

## HIGH-TEMPERATURE VISCOSITY OF COMMERCIAL GLASSES

PAVEL HRMA

*Pacific Northwest National Laboratory, Richland, WA 99352, United States of America*

E-mail: pavel.hrma@pnl.gov

Submitted November 11, 2005; accepted December 12, 2005

**Keywords:** Viscosity, Glass, Viscosity model

*Arrhenius models were developed for glass viscosity within the processing temperature range for six types of commercial glasses: low-expansion-borosilicate glasses, E glasses, fiberglass wool, TV panel glasses, container glasses, and float glasses. Both local models (for each of the six glass types) and a global model (for the composition region of commercial glasses, i.e., the six glass types taken together) are presented. The models are based on viscosity data previously obtained with rotating spindle viscometers within the temperature range between 900°C and 1550°C; the viscosity varied from 1 Pas to 750 Pas. First-order models were applied to relate Arrhenius coefficients to the mass fractions of 15 components: SiO<sub>2</sub>, TiO<sub>2</sub>, ZrO<sub>2</sub>, Al<sub>2</sub>O<sub>3</sub>, Fe<sub>2</sub>O<sub>3</sub>, B<sub>2</sub>O<sub>3</sub>, MgO, CaO, SrO, BaO, PbO, ZnO, Li<sub>2</sub>O, Na<sub>2</sub>O, and K<sub>2</sub>O. The R<sup>2</sup> is 0.98 for the global model and ranges from 0.97 to 0.99 for the six local models. The models are recommended for glasses containing 42 to 84 mass% SiO<sub>2</sub> to estimate viscosities or temperatures at a constant viscosity for melts within both the temperature range from 1100°C to 1550°C and viscosity range from 5 to 400 Pas.*

## INTRODUCTION

The melting behavior of glasses depends on their viscosity-temperature relationships. Glassmelting furnace design and operation are largely determined by the temperature span within which melt viscosity allows successful melting, fining, and conditioning of the glass. Therefore, the knowledge of glass viscosity as a function of temperature and glass composition is crucial for efficient glassmaking.

The most commonly used viscosity-temperature relationship for a wide span of viscosities (over 12 orders of magnitude) is the Vogel-Fulcher-Tammann (VTF) equation,

$$\ln \eta = F_1 + \frac{F_2}{T - T_0} \quad (1)$$

where  $\eta$  is the viscosity,  $T$  is the absolute temperature, and  $F_1$ ,  $F_2$ , and  $T_0$  are temperature-independent coefficients [1]. However, during the melting process, the viscosity of molten glass spans only 3 orders of magnitude (1 to 10<sup>3</sup> Pas). For this relatively narrow range, the viscosity-temperature relationship is sufficiently well represented by the Arrhenius equation [2,3],

$$\ln \eta = A + \frac{B}{T} \quad (2)$$

The Arrhenius coefficients,  $A$  and  $B$ , are functions of glass composition. Since all mixture properties, extensive and non-extensive, are expressible in terms of

their partial specific (per mass) or molar values [4], Arrhenius coefficients for viscosity can be related to glass composition as

$$A = \sum_{i=1}^N A_i x_i \quad (3)$$

and

$$B = \sum_{i=1}^N B_i x_i \quad (4)$$

where  $A_i$  and  $B_i$  are the  $i$ -th component partial specific Arrhenius coefficients, and  $N$  is the total number of components.

The  $A_i$  and  $B_i$  values are relatively constant within the range of composition of commercial glasses. Therefore, equations (3) and (4) can be treated as linear models and  $A_i$  and  $B_i$  as component coefficients for glass viscosity. We can also introduce the  $i$ -th component partial specific viscosity, i.e., a temperature-dependent coefficient, defined as

$$\eta_i = \exp\left(A_i + \frac{B_i}{T}\right) \quad (5)$$

Based on the partial specific values (component coefficients), the viscosity of molten glass (within the glass melting temperature range) can be estimated using the equation

$$\eta = \exp\left(\sum_{i=1}^N \left[A_i + \frac{B_i}{T}\right] x_i\right) \quad (6)$$

or

$$\ln \eta = \sum_{i=1}^N x_i \ln \eta_i \quad (7)$$

which can also be written as

$$\eta = \prod_{i=1}^N \eta_i^{x_i} \quad (8)$$

A convenient feature of the Arrhenius equation is its linearity, which allows us to express explicitly the temperature at which viscosity has a desired value. Rearranging equation (6), we obtain

$$T = \frac{\sum_{i=1}^N B_i x_i}{\ln \eta - \sum_{i=1}^N A_i x_i} \quad (9)$$

To develop mathematical models that represent the viscosity-temperature-composition relationships for commercial glasses, several steps need to be taken [5]. Roughly, the composition and temperature regions must be defined and covered with a matrix of a sufficient number of points. Glasses of the corresponding compositions are then made and tested at several temperatures to generate a database to which equation (6) can be fitted.

Table 1 lists composition regions of six types of commercial glasses evaluated in this study: E-glass (E), float glass (F), low-expansion-borosilicate glass (LE), TV panel glass (TV), fiberglass wool (FW), and container glass (C). The composition matrices of glasses that cover these six regions are presented in [6]. Figure 1 displays the maximum mass fractions of glass components for the overall composition region of commercial glasses tested (the minimum fractions of all components but SiO<sub>2</sub> were 0). As table 1 shows, the SiO<sub>2</sub> mass fraction range is 0.42 to 0.84, and the maximum mass frac-

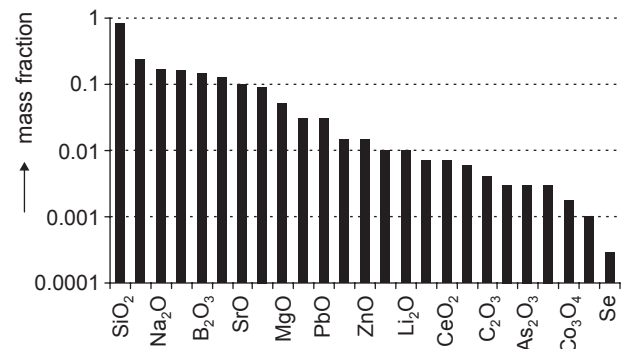


Figure 1. Maximum mass fractions of components in the composition region of commercial glasses .

Table 1. Composition regions of glasses in mass %.

	E	F	LE	TV	FW	C	All
SiO <sub>2</sub>	41.6-71.5	67.5-77.3	63-84	50-83	48.6-78	62.5-81	41.6-84
B <sub>2</sub> O <sub>3</sub>	0-9		10-15		3-9		0-15
Al <sub>2</sub> O <sub>3</sub>	12-16	0.1-2	2-7	1.3-3.5	0-6	1-3	0-16
MgO	0.5-4.5	3-4		0-1.5	1-5	0-3	0-5
CaO	16-24	7-9	0-2	0-3.5	5-11	7-12	0-24
Na <sub>2</sub> O	0-2	12-15	4-8	6-9	13-17	11-15	0-17
K <sub>2</sub> O	0-0.5	0-2	0-3	6-9	0-2	0-2	0-9
Fe <sub>2</sub> O <sub>3</sub>	0-0.8	0.1-1.5			0-0.6	0-0.4	0-1.5
TiO <sub>2</sub>	0-1	0-1		0.1-0.5		0-0.5	0-1
F	0-0.6			0-0.7	0-0.6		0-0.7
SO <sub>3</sub>					0-0.2	0-0.3	0-0.3
Li <sub>2</sub> O				0-0.5		0-1	0-1
Cr <sub>2</sub> O <sub>3</sub>		0-0.4				0-0.3	0-0.4
BaO			0-2	2-13		0-0.1	0-13
CeO <sub>2</sub>				0-0.7			0-0.7
ZrO <sub>2</sub>				0-3			0-3
PbO				0-3			0-3
ZnO				0-1.5			0-1.5
As <sub>2</sub> O <sub>3</sub>				0-0.3			0-0.3
Sb <sub>2</sub> O <sub>3</sub>				0.2-0.6			0-0.6
SrO				1-10			0-10
MnO <sub>2</sub>		0-0.3					0-0.3
Se		0-0.03					0-0.03
Co <sub>3</sub> O <sub>4</sub>		0-0.2					0-0.2
FeO	0-0.1				0-0.1		0-0.1

E - E glass, F - float glass, LE - low-expansion-borosilicate glass, TV - TV panel glass, FW-fiberglass wool, C - container glass

tions of major components are CaO 0.24, Na<sub>2</sub>O 0.17, Al<sub>2</sub>O<sub>3</sub> 0.16, B<sub>2</sub>O<sub>3</sub> 0.15, BaO 0.13, SrO 0.10, K<sub>2</sub>O 0.09, and MgO 0.05.

Out of the total number of 150 different compositions (25 compositions-baseline plus 24 variations-for each of the six groups), 147 were fabricated at Alfred University and tested in Pacific Northwest National Laboratory (PNNL) where viscosity was measured with rotating spindle viscometers. Hрма et al., Chapter 7 in

[6], describe the details of measurement and list the measured viscosity data. Figure 2 maps the viscosity-temperature data points. Note that LE and E glasses occupy the high-viscosity-high-temperature corner, F glasses have relatively small viscosity variations, and FW glasses cover the largest viscosity-temperature area. Overall, the temperature of measurements spanned an interval from 899°C to 1554°C, and the viscosity varied from 1 Pas to 747 Pas.

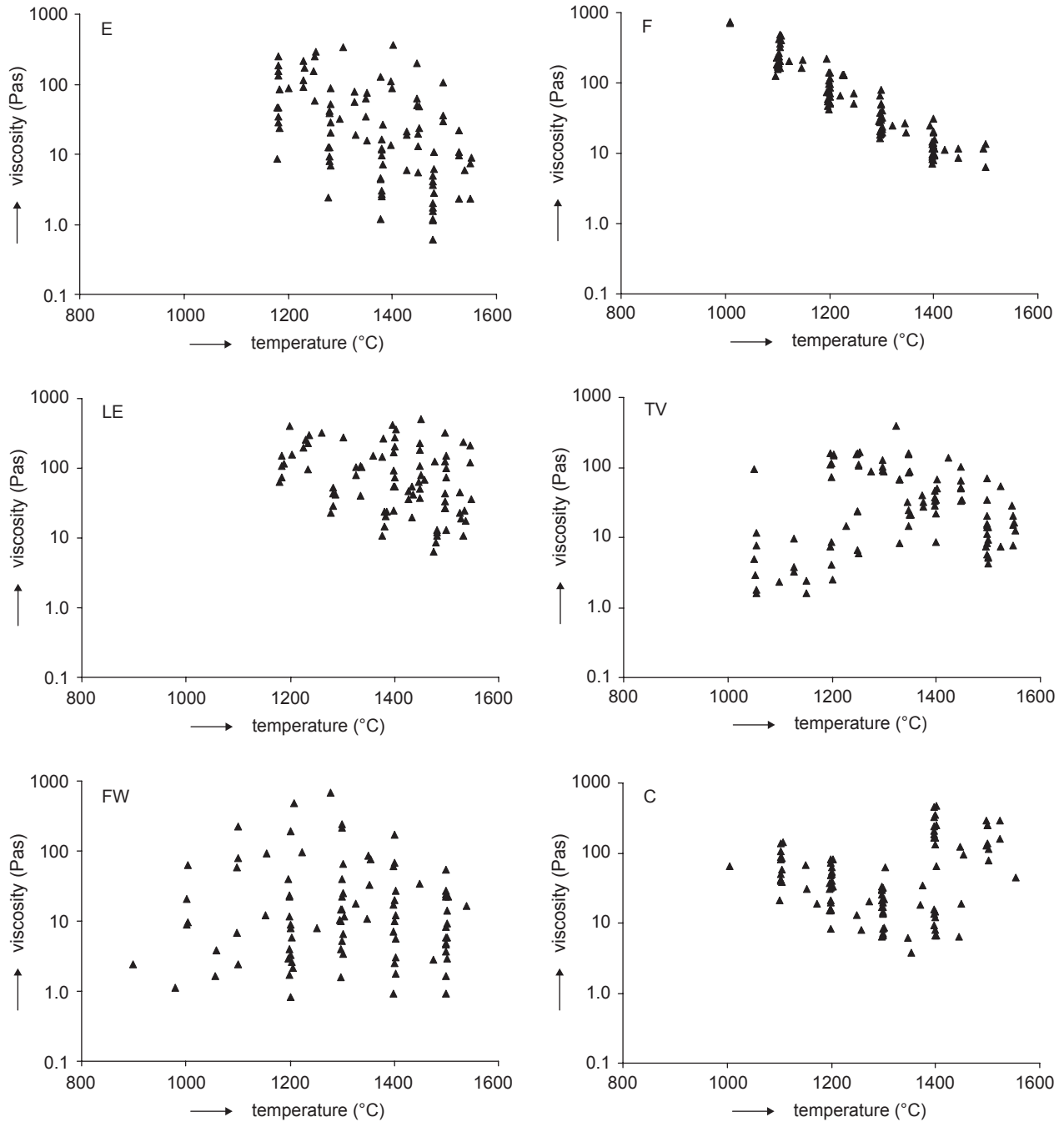


Figure 2. Maps of viscosity-temperature data points for six types of commercial glasses: E glass (E), float glass (F), low-expansion-borosilicate glass (LE), TV panel glass (TV), fiberglass wool (FW), and container glass (C).

Fluegel et al. [7] augmented these low-viscosity data by high-viscosity data measured with the beam bending and parallel plate methods [6] and by published viscosities of an additional 150 glasses. They used the resulting large database to obtain component coefficients for isokoms, i.e., temperatures at constant viscosity ( $T_\eta$ ) using the formula

$$T_\eta = T_0 + 10^2 \sum_i T_i c_i + 10^4 \sum_{i,j} T_{ij} c_i c_j + 10^6 \sum_{i,j,k} T_{ijk} c_i c_j c_k \quad (10)$$

where  $T_0$ ,  $T_i$ ,  $T_{ij}$ , and  $T_{ijk}$  are composition-independent coefficients, and  $c_i$  is the  $i$ -th component mole fraction. The composition-independent coefficients are functions of viscosity and are listed in table 2 for three viscosity values corresponding to  $\log(\eta \text{ (Pas)}) = 1.5, 6.6, \text{ and } 12.0$ .

Fluegel et al., Chapter 9 in [6], provide also four first-order models for  $\log(\eta \text{ (Pas)}) = 1.5, 6.6, \text{ and } 12.0$  isokoms for the following five composition regions: F+C (float glasses plus container glasses), E, TV, LE, and FW. They report the significant coefficients and the intercept, corresponding to the equation

$$T_\eta = T_0 + \sum_{i=1}^S b_i x_i \quad (11)$$

where  $b_i$  is the significant component coefficient, and  $S$  is the number of significant components. This equation can be conveniently rearranged into the form

$$T_\eta = \sum_{i=1}^N a_i x_i \quad (12)$$

where  $a_i = b_i + T_0$  ( $i=1, \dots, S$ ),  $N = S + 1$ , and  $a_n = T_0$ ; here the  $n$ -th component, called "others" in table 3, comprises all other than significant components plus  $\text{SiO}_2$ . Hence,

$$x_n = 1 - \sum_{i=1}^S x_i \quad (13)$$

Table 3 lists the  $a_i$  coefficients for the  $\log(\eta \text{ (Pas)}) = 1.5$  isokom.

In this contribution, the values of  $A_i$  and  $B_i$  coefficients were obtained by fitting equation (6) to viscosity versus temperature and composition data for individual glass types (local models) as well as for all commercial glasses tested (a global model). Generally, global models cover large composition regions whereas local models are developed for compositional neighborhoods of base glasses formulated for various applications and production technologies.

Table 3. Component coefficients for  $\eta = 31.6 \text{ Pas}$  isokom in  $^\circ\text{C}$  (Fluegel et al., Chapter 9 in [6]).

	F+C	E	TV	FW
$\text{Al}_2\text{O}_3$	2183			
$\text{B}_2\text{O}_3$		-15		-306
BaO			700	
CaO	237	-82	371	260
F			-3140	
$\text{Fe}_2\text{O}_3$	322			
$\text{K}_2\text{O}$	398		300	-427
$\text{Li}_2\text{O}$	-4707	1837	-3463	
MgO	698	494		1287
$\text{Na}_2\text{O}$	-533	93	-912	-670
PbO			727	
SrO			535	
$\text{TiO}_2$	-295		-3483	
Others	1811	1837	1865	1848

The F+C column lists coefficients for float glass (F) plus container glass (C). Component coefficients for  $\eta = 31.6 \text{ Pas}$  isokom are not reported for low-expansion (LE) glasses. "Others" are all remaining components including  $\text{SiO}_2$  [see equation (13)].

Table 2. Component coefficients for isokoms.

$\eta \text{ (Pas)}$	$3.16 \times 10^1$	$3.98 \times 10^6$	$1.00 \times 10^{12}$	$\eta \text{ (Pas)}$	$3.16 \times 10^1$	$3.98 \times 10^6$	$1.00 \times 10^{12}$
	$T_0 \text{ (K)}$				$T_{ij}$		
	1816.4	876.7	618.4				
	$T_i$						
$\text{Al}_2\text{O}_3$	4.35	15.48	11.24	$\text{Al}_2\text{O}_3 \times \text{B}_2\text{O}_3$		-0.625	-0.626
$\text{B}_2\text{O}_3$	-13.49	-3.16	-3.10	$\text{Al}_2\text{O}_3 \times \text{MgO}$	-0.526	-0.911	
BaO	-22.26	-4.16		$\text{Al}_2\text{O}_3 \times \text{Na}_2\text{O}$	0.761	-0.686	
CaO	-18.00	-2.77	1.05	$\text{B}_2\text{O}_3 \times \text{K}_2\text{O}$			0.585
F	-14.73	-6.14	-9.33	$\text{B}_2\text{O}_3 \times \text{Na}_2\text{O}$	-0.536	0.156	0.573
FeOx	-15.33	-6.79		$\text{B}_2\text{O}_3 \times \text{CaO}$	-0.225	-0.117	
$\text{K}_2\text{O}$	-19.21	-11.90	-11.94	CaOxF	1.017		
$\text{Li}_2\text{O}$	-29.14	-16.81	-21.06	CaOx $\text{K}_2\text{O}$		0.334	0.468
MgO	-5.99	4.02	-1.54	CaOx $\text{Na}_2\text{O}$	0.215	0.207	0.157
$\text{Na}_2\text{O}$	-25.10	-11.27	-7.30	Fx $\text{K}_2\text{O}$		-0.565	
PbO	-23.22	-8.62	-4.61	$\text{K}_2\text{O} \times \text{MgO}$	0.788		
SrO	-20.09	-3.01	2.25	$\text{MgO} \times \text{Na}_2\text{O}$		-0.174	
ZnO	-9.42	-1.67				$T_{ijk}$	
$\text{ZrO}_2$		9.51	9.03	$\text{Al}_2\text{O}_3 \times \text{B}_2\text{O}_3 \times \text{Na}_2\text{O}$			-0.0449
				$\text{Al}_2\text{O}_3 \times \text{CaO} \times \text{Na}_2\text{O}$			-0.0285
				$\text{Al}_2\text{O}_3 \times \text{MgO} \times \text{Na}_2\text{O}$		0.0732	
				$\text{B}_2\text{O}_3 \times \text{CaO} \times \text{Na}_2\text{O}$			-0.0111
				CaOxMgOx $\text{Na}_2\text{O}$	-0.0211	-0.0282	

RESULTS

Viscosity data for three (LE 16, FW 18, and E 20) out of 150 glasses originally designed were not available because these glasses were never fabricated. With two exceptions, Li<sub>2</sub>O and K<sub>2</sub>O, only mass fractions of components with ≥1 mass% were selected for fitting. Although fluorine is a minor component that strongly impacts viscosity, its mass fraction was not included as a variable because including it did not improve the outcome. To obtain  $A_i$  and  $B_i$  values, equation (6) was fitted to data. The compositions were not renormalized (to make the sum of mass fractions equal to 1) when minor components were excluded from calculations. Of the 147 glasses for which viscosity data were available, three were eliminated as outliers (E 3, F 9, and TV 8). Several individual data points were also removed as outliers. The outliers were selected based on local models as glasses with unusually high values of  $\Delta^2 = [\ln(\eta_m/\eta_c)]^2$ , where the subscript  $m$  stands for measured and  $c$  for calculated values (using local models with outliers removed). In the extreme case of E-glasses, the difference between  $\Delta^2$  values for outliers was substantially higher than  $\Delta^2$  values for regular data ( $\Delta^2 \geq 4.5$  for outliers and  $\Delta^2 \leq 0.28$  for all other data). For other glass groups, these differences were lower: 3.6 and 0.57 for LE, 0.77 and 0.31 for FW, 0.50 and 0.39 for FW, 0.45 and 0.13 for F; no outliers were identified in C glasses.

Table 4 lists  $A_i$  and  $B_i$  values of the global model obtained by fitting equation (6) to all data except outliers. Table 5 summarizes the values of  $A_i$ ,  $B_i$ , and  $\ln(\eta_{i,1500^\circ\text{C}})$  for individual types of glasses (local models).

Table 4. Component coefficients for viscosity in Pas, global model.

	$A_i$	$B_i, 10^3 \text{ K}$	$\ln(\eta_i(\text{Pas}))$ at 1500°C
SiO <sub>2</sub>	-6.25	24.14	7.37
TiO <sub>2</sub>	-26.72	28.15	-10.84
ZrO <sub>2</sub>	-8.41	22.88	4.49
Al <sub>2</sub> O <sub>3</sub>	12.68	-4.66	10.06
Fe <sub>2</sub> O <sub>3</sub>	19.39	-35.05	-0.37
B <sub>2</sub> O <sub>3</sub>	0.45	-14.74	-7.86
MgO	-41.91	60.26	-7.93
CaO	-53.10	66.80	-15.43
SrO	-18.19	20.84	-6.44
BaO	-15.99	19.51	-4.99
PbO	-13.39	11.89	-6.68
ZnO	-39.25	67.15	-1.38
Li <sub>2</sub> O	-80.42	50.11	-52.16
Na <sub>2</sub> O	-13.02	-2.12	-14.22
K <sub>2</sub> O	-27.10	30.05	-10.15
R <sup>2</sup>	0.984		
R <sup>2</sup> adj	0.983		

Table 5. Component coefficients for viscosity (in Pas), local models.

	$A_i$					
	E	F	LE	TV	FW	C
SiO <sub>2</sub>	-5.65	-6.52	-9.64	-11.36	-17.97	-8.43
TiO <sub>2</sub>	38.62	-59.51				
ZrO <sub>2</sub>				-17.19		
Al <sub>2</sub> O <sub>3</sub>	-28.47	9.72	67.39	29.72	4.13	-6.78
Fe <sub>2</sub> O <sub>3</sub>		-37.04				
B <sub>2</sub> O <sub>3</sub>	10.17		1.15		-11.48	
MgO	-49.06	-48.40		-24.32	-31.82	-16.66
CaO	-34.53	-48.11	-57.84	-12.15	-66.91	-16.62
SrO				-21.97		
BaO			-53.64	-15.36		
PbO				-41.12		
ZnO				-28.75		
Li <sub>2</sub> O						-98.08
Na <sub>2</sub> O	0.91	-7.51	-44.15	25.28	45.54	-21.40
K <sub>2</sub> O	-78.02	-16.67	-31.83	-33.79	-8.52	-7.84

	$10^{-3} B_i \text{ (K)}$					
	E	F	LE	TV	FW	C
SiO <sub>2</sub>	27.62	23.25	31.01	31.28	41.64	26.16
TiO <sub>2</sub>	-69.55	90.75				
ZrO <sub>2</sub>				39.28		
Al <sub>2</sub> O <sub>3</sub>	47.71	2.45	-69.48	-26.18	8.73	34.93
Fe <sub>2</sub> O <sub>3</sub>		60.30				
B <sub>2</sub> O <sub>3</sub>	-28.43		-11.78		-2.20	
MgO	65.01	69.96		49.27	54.73	20.68
CaO	34.30	63.10	80.83	5.67	94.41	14.97
SrO				26.59		
BaO			84.06	19.30		
PbO				54.34		
ZnO				49.55		
Li <sub>2</sub> O						77.22
Na <sub>2</sub> O	-22.82	-8.16	11.39	-72.05	-91.92	12.97
K <sub>2</sub> O	112.93	18.44	23.14	50.04	-0.93	11.52

	$\ln(\eta_{i,1500^\circ\text{C}} \text{ (Pas)})$					
	E	F	LE	TV	FW	C
SiO <sub>2</sub>	9.93	6.60	7.85	6.28	5.51	6.32
TiO <sub>2</sub>	-0.61	-8.33				
ZrO <sub>2</sub>				4.97		
Al <sub>2</sub> O <sub>3</sub>	-1.56	11.11	28.20	14.95	9.06	12.92
Fe <sub>2</sub> O <sub>3</sub>		-3.03				
B <sub>2</sub> O <sub>3</sub>	-5.86		-5.50		-12.72	
MgO	-12.39	-8.94		3.47	-0.95	-5.00
CaO	-15.18	-12.52	-12.25	-8.95	-13.66	-8.17
SrO				-6.97		
BaO			-6.23	-4.47		
PbO				-10.47		
ZnO				-0.80		
Li <sub>2</sub> O						-54.53
Na <sub>2</sub> O	-11.97	-12.11	-37.73	-15.36	-6.31	-14.08
K <sub>2</sub> O	-14.33	-6.27	-18.78	-5.56	-9.04	-1.34

## DISCUSSION

Figure 3 compares calculated versus measured values for viscosity, and table 6 lists the values of  $R^2$  and  $R^2_{\text{adj}}$  that express the fraction of variability accounted for by the model ( $R^2_{\text{adj}}$  is adjusted for the number of parameters used in fitting the model). As expected, both figure 3 and table 6 show that the individual fits predict viscosity values better than the overall fit. The difference between viscosity predicted by the local models and the global model is the smallest for float glass (F) and the largest for low-expansion glass (LE). As figure 2 shows, float glass has the smallest variability of data, and low-expansion glass is the most difficult to melt. Models for all individual glass types have high  $R^2$  values ranging from 0.97 for TV glasses to 0.99 for float glasses. The global model represents viscosity data as a whole with a good  $R^2$  value of 0.98. However, when the global model is applied to individual glass types,  $R^2$  values vary from 0.92 to 0.98, except for low-expansion glasses for which the fit is rather poor ( $R^2 = 0.75$ ).

Table 6.  $R^2$  values for viscosity models.

	E	F	LE	TV	FW	C	All
$R^2_{\text{ind}}$	0.982	0.989	0.967	0.965	0.967	0.983	
$R^2_{\text{all}}$	0.939	0.981	0.748	0.923	0.940	0.962	0.984
$R^2_{\text{adj,ind}}$	0.979	0.987	0.961	0.955	0.961	0.981	
$R^2_{\text{adj,all}}$	0.926	0.978	0.700	0.901	0.930	0.957	0.983

As figure 3 and table 6 indicate, local models are generally more accurate than the global model within the composition regions of their databases (listed in table 1). The global model is recommended for compositions within the overall composition region that are not covered by any of the local models. However, for high-viscosity-high-temperature glasses (the LE type), the global model may perform rather poorly.

The effect of composition change on viscosity can be expressed as the change in viscosity,  $\Delta\eta_j$ , caused by replacing a mass fraction of silica ( $-\Delta x$ ) with the same mass fraction ( $\Delta x$ ) of  $j$ -th oxide. By equation (7),

$$\Delta\eta_j = \eta_0 \{ \exp [\Delta x (Z_j - Z_{\text{SiO}_2})] - 1 \} \quad (14)$$

where  $\eta_0$  is the melt viscosity before the fraction of silica was replaced with the same mass of  $j$ -th oxide, and  $Z_j = \ln[\eta_j(T)]$  is the partial specific logarithmic viscosity at temperature  $T$  (shown in tables 3 and 4 for  $T = 1500^\circ\text{C}$ ). By equation (14), the  $j$ -th component tends to increase the melt viscosity when  $\Delta\eta_j > 0$  at  $1500^\circ\text{C}$ . Calculations were performed for  $Z_j = \ln(\eta_{i,1500^\circ\text{C}} \text{ (Pas)})$ ,  $\Delta x = 0.02$  (2 mass% replacement) and  $\eta_0 = 10 \text{ Pas}$ . Figures 4 and 5 display the results for several major glass components. In figure 4, the  $\Delta\eta_j$  values are based on  $Z_j$

values from the global model. Figure 5 compares  $\Delta\eta_j$  values based on local models with those from the global model. As expected,  $\text{B}_2\text{O}_3$ ,  $\text{Na}_2\text{O}$ ,  $\text{K}_2\text{O}$ ,  $\text{MgO}$ , and  $\text{CaO}$  decrease glass viscosity when replacing  $\text{SiO}_2$  whereas  $\text{Al}_2\text{O}_3$  tends to increase viscosity except for the low-alkali E-glass. Note that in the high-silica-high-boria LE glass,  $\text{Al}_2\text{O}_3$  and  $\text{Na}_2\text{O}$  have a significantly higher impact on viscosity than in any other glass tested.

In glass technology, it is often important to know how rapidly viscosity changes with changing temperature and how the rate of change is affected by glass composition. By equation (2),

$$\frac{\partial \ln \eta}{\partial T} = -\frac{B}{T^2} \quad (15)$$

Since viscosity decreases as temperature increases,  $B$  is always positive, and the higher the  $B$  at a given temperature, the steeper the slope. Consequently, as molten glass gets cooler, its viscosity increases less with decreasing temperature when the  $B$  value is small; such a glass is called a "long" glass because it takes a longer time to reach a high viscosity at a given rate of cooling. This is illustrated in figure 6, which plots the temperature increase (starting from  $1500^\circ\text{C}$ ) associated with a 10-times increase in melt viscosity as a function of  $B$ .

The average  $B$  value for glasses tested in this study is  $B_a = 2.38 \cdot 10^4 \text{ K}$ . With a glass "length" component effect defined as  $L_i = B_i - B_a$ , components with  $L_i > 0$  tend to "lengthen" the glass and components with  $L_i < 0$  tend to "shorten" it. Figure 7 compares the effects of several components on the melt "length" at glass processing temperatures. This picture will change at glass-forming temperatures because the Arrhenius relationship no longer represents the melt viscosity-temperature relationship for commercial glasses below  $1000^\circ\text{C}$ .

The  $\log(\eta \text{ (Pas)}) = 1.5$  ( $\eta = 31.6 \text{ (Pas)}$ ) isokoms were obtained from equation (9) with the coefficient values listed in table 4. To compare the results of calculations with experimental data, the temperature,  $T_{31.6}$ , at which  $\eta = 31.6 \text{ Pas}$ , was obtained by fitting equation (2) to data for each glass. Figure 8 shows the result together with a similar plot in which the Fuegel et al. [7] model is compared with  $T_{31.6}$  values obtained from experimental data. The vertical lines in figure 8 indicate the maximum temperature of the viscosity measurement, beyond which all values are extrapolated. As figure 9 shows, both models predict similar  $T_{31.6}$  values for  $T < 1400^\circ\text{C}$ . For higher temperatures, the Fuegel et al. [7] model seems to underpredict the isokoms, provided that extrapolated data can be trusted. However, high temperatures are outside the application limits of the Fuegel et al. model; most extrapolated temperature values from data obtained at lower temperatures were excluded from the model database [7].

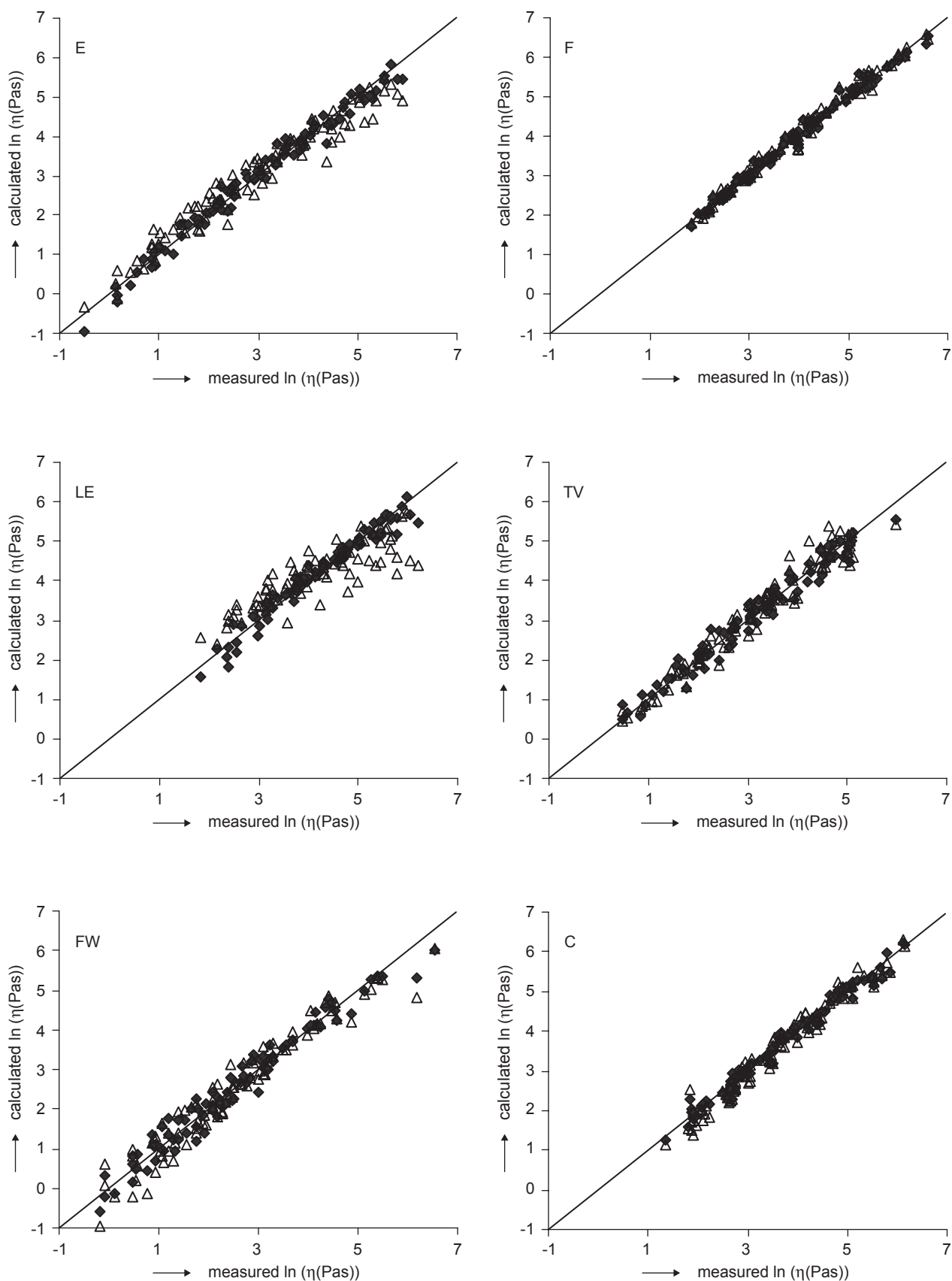


Figure 3. Calculated versus measured values for viscosity; solid points represent local models, and hollow points stand for the global model applied to individual glass types.

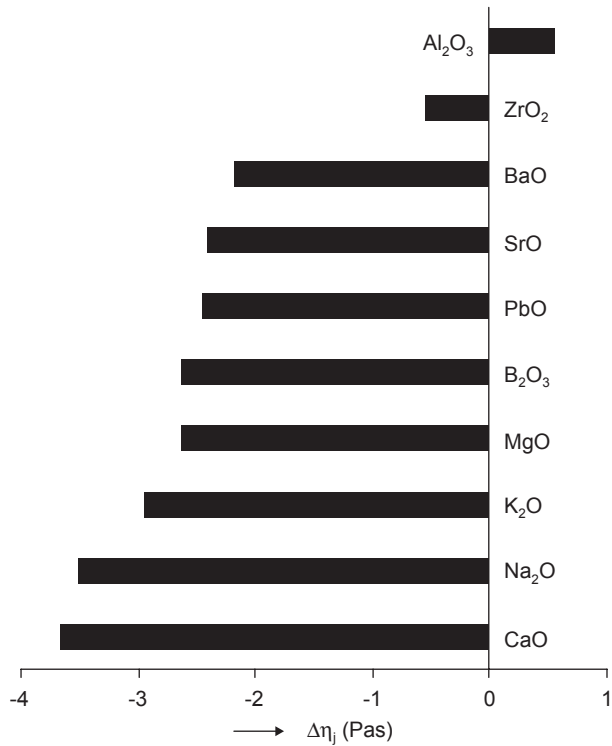


Figure 4. Effect of replacing 2 mass% SiO<sub>2</sub> with another oxide on melt viscosity at 1500°C.

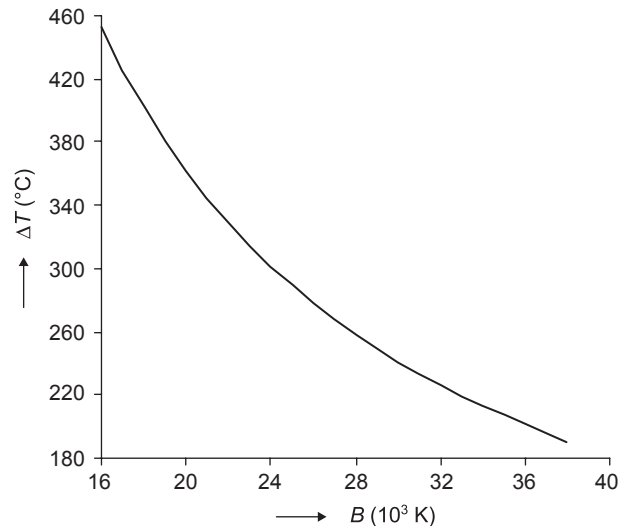


Figure 6. Effect of B on the temperature decrease ( $\Delta T$ ) from 1500°C that results in a 10 times increase in melt viscosity.

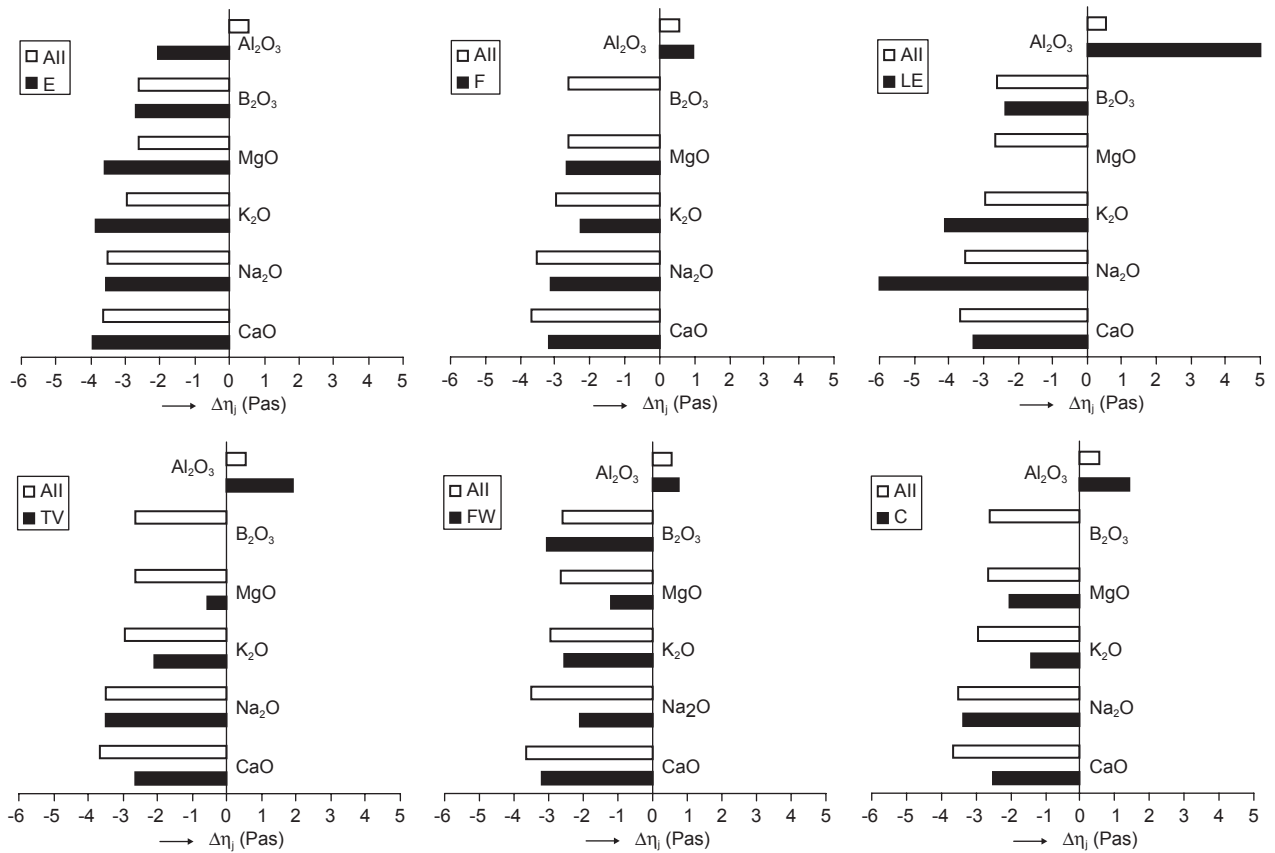


Figure 5. Effect of replacing 2 mass% SiO<sub>2</sub> with another oxide on melt viscosity at 1500°C: comparison of individual glass types with the full set of data.

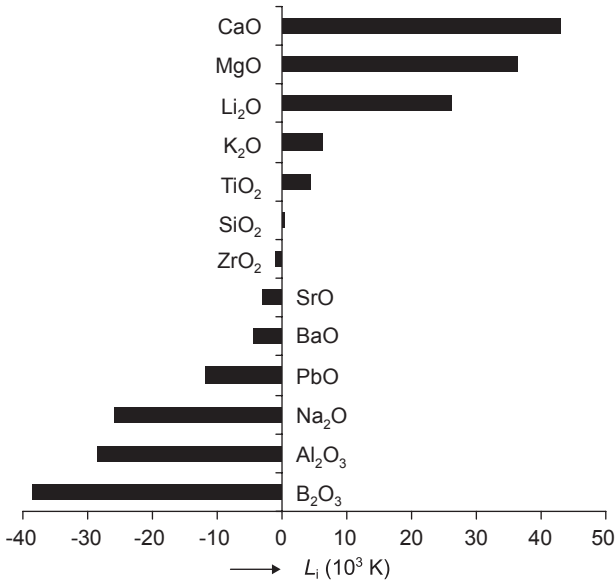


Figure 7. Effect of glass components on melt "length".

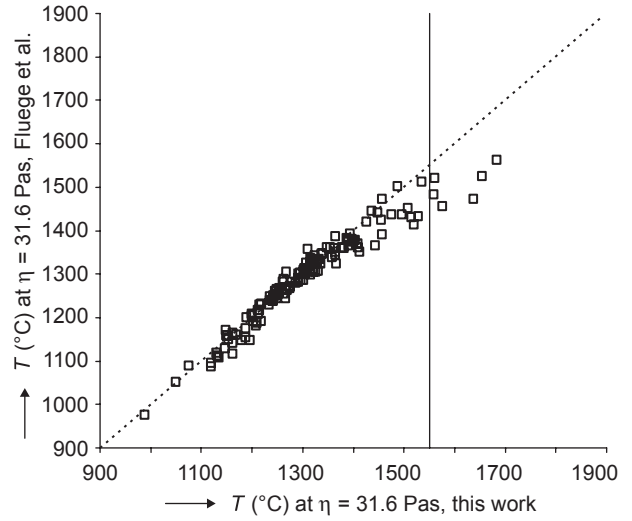


Figure 9.  $T_{31.6 \text{ Pas}}$  isokom obtained using the nonlinear model by Fluege et al. [7] versus the global Arrhenius model (table 4).

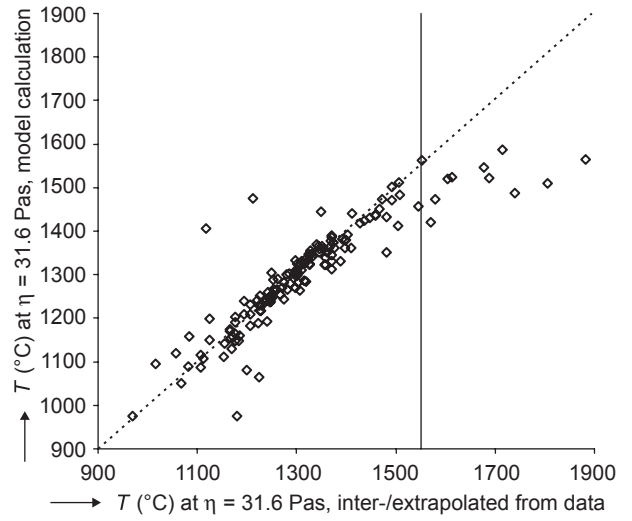
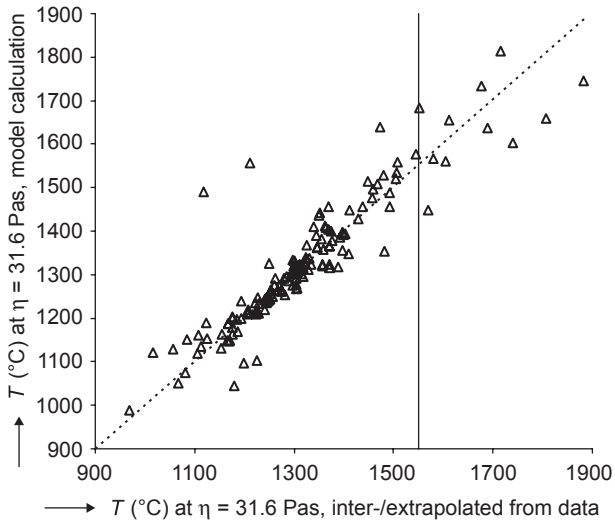


Figure 8.  $T_{31.6 \text{ Pas}}$  isokom, model calculation versus values obtained for experimental data; left: Arrhenius model with 30 coefficients listed in table 4; right: Fluegel et al. [7] model, equation (10), with 22 coefficients listed in table 2.

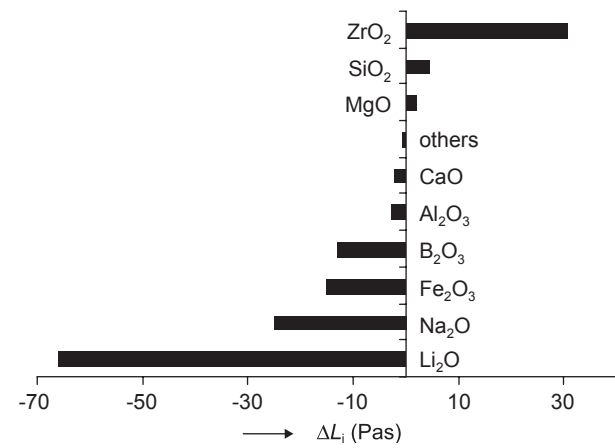
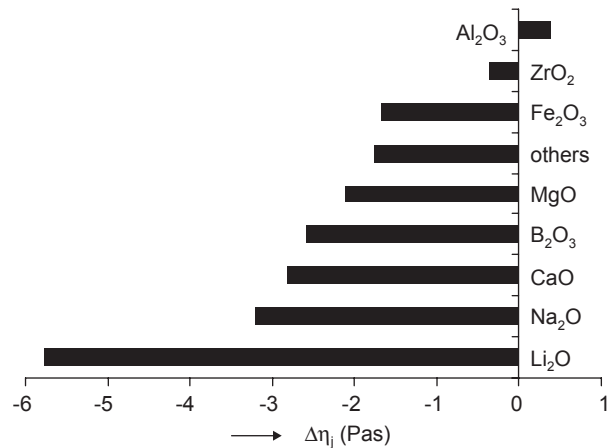


Figure 10. Effect of components on high-level waste glass viscosity (left) and "length" (right).

Finally, it may be of interest to compare commercial and waste glasses with respect to the effects of glass components on their viscosity. Table 7 lists the composition region and the Arrhenius coefficients for the viscosity of these glasses [3]. Viscosity data for the waste glasses were measured within 950°C and 1250°C, and viscosity values ranged from 0.4 to 90 Pas at 1150°C. Figure 10 shows the values of  $\Delta\eta_j$  ( $\Delta x = 0.02$ ,  $\eta_0 = 10$  Pas, and  $T = 1150^\circ\text{C}$ ) and  $L_i$ . A comparison of figures 4 and 10 reveals that the impact of replacing  $\text{SiO}_2$  with an equal mass of another component is very similar in commercial and waste glasses. However, the impacts of glass components on melt "length" are different, indicating that the differences in composition regions and temperature ranges significantly influence the secondary properties (such as the temperature derivative of viscosity) of melts.

Table 7. Composition region and viscosity coefficients for high-level waste glasses [3].

	Mass fraction ranges		Viscosity coefficients	
	$x_{\min}$	$x_{\max}$	$A_i$	$10^3 B_i$ (K)
$\text{SiO}_2$	0.42	0.57	-11.1	28.5
$\text{B}_2\text{O}_3$	0.05	0.20	-13.7	10.9
$\text{Na}_2\text{O}$	0.05	0.20	-9.6	-1.2
$\text{Li}_2\text{O}$	0.01	0.07	-4.5	-42.3
$\text{CaO}$	0.00	0.10	-22.8	21.5
$\text{MgO}$	0.00	0.08	-21.1	25.8
$\text{Fe}_2\text{O}_3$	0.005	0.15	-6.4	8.8
$\text{Al}_2\text{O}_3$	0.00	0.17	-4.1	21.2
$\text{ZrO}_2$	0.00	0.13	-31.3	54.6
Others	0.01	0.10	-17.0	23.0

### CONCLUSION

For the processing temperature range for common commercial glasses (1100°C to 1550°C), the Arrhenius relationship represents the viscosity-temperature relationship reasonably well; the  $R^2$  ranges from 0.97 to 0.99 for six local models developed for individual glass types (E glass, float glass, low-expansion-borosilicate glass, TV panel glass, fiberglass wool, and container glass) and 0.98 for the global model covering the whole composition region of commercial glasses containing 42 to 84 mass%  $\text{SiO}_2$ . The models adequately represent the viscosity-temperature relationship of glass at  $\eta < 10^3$  Pas, or, more accurately, 5 to 400 Pas. The global Arrhe-

nus model was found in good agreement with a nonlinear model developed by Fluegel et al. [7]. The component effects were found similar to those previously established for high-level waste glasses.

### References

- Scholze H.: *Glass*, Springer, New York 1990.
- Bansal N. P., Doremus R. H.: *Handbook of Glass Properties*, Academic Press, Orlando 1986.
- Hrma P., Piepel G. F., Redgate P. E., Smith D. E., Schweiger M. J., Vienna J. D., Kim D-S.: *Ceramic Transactions 61*, 505 (1995).
- Hrma P.: *Ceramic Transactions 87*, 245 (1998).
- Piepel G. F., Hrma P., Vienna J. D.: *Glass Chemistry Development Strategy For Hanford High Level Waste (HLW)*, in *Science and Technology for Disposal of Radioactive Tank Wastes*, pp. 393-402, Plenum Press, New York 1998.
- Seward III T. P., Vascott T. (Editors): *High temperature glass melt property database for process modeling*, American Ceramic Society, Westerville, Ohio 2005.
- Fluegel A., Varshneya A. K., Earl D. A., Seward T. P., Oksoy D.: *Improved Composition-Property Relations in Silicate Glasses, Part I: Viscosity*, *Ceramic Transaction* [in print].

### VYSOKOTEPLTNÍ VISKOZITA PRŮMYSLOVÝCH SKEL

PAVEL HRMA

*Pacific Northwest National Laboratory  
Richland, WA 99352, United States of America*

Závislost viskozity skelných tavenin v oblasti tavicích teplot byla aproximována lineárními modely na bázi Arrheniovy rovnice pro šest typů průmyslových skel: borosilikátová skla s nízkým koeficientem tepelné roztažnosti, E skla, skelná vata, skla pro televizní obrazovky, obalová skla, a skla float. Modely reprezentují závislost viskozity na teplotě a složení jak pro jednotlivé typy skel (lokální modely) tak pro celkovou oblast složení průmyslových skel (globální model). Modelové koeficienty byly optimalizovány s použitím viskozitních dat změřených rotačním viskozimetrem v rozmezí 900-1550°C, ve kterém viskozita nabývala hodnot 1-750 Pas, pro 15 složek:  $\text{SiO}_2$ ,  $\text{TiO}_2$ ,  $\text{ZrO}_2$ ,  $\text{Al}_2\text{O}_3$ ,  $\text{Fe}_2\text{O}_3$ ,  $\text{B}_2\text{O}_3$ ,  $\text{MgO}$ ,  $\text{CaO}$ ,  $\text{SrO}$ ,  $\text{BaO}$ ,  $\text{PbO}$ ,  $\text{ZnO}$ ,  $\text{Li}_2\text{O}$ ,  $\text{Na}_2\text{O}$  a  $\text{K}_2\text{O}$ .  $R^2$  nabyla hodnoty 0.98 pro globální model a 0.97 až 0.99 pro šest lokálních modelů. Modely lze doporučit pro průmyslová skla s obsahem 42-84 %  $\text{SiO}_2$  k odhadu viskozit nebo teplot pro danou hodnotu viskozity skelných tavenin v rozmezí teplot 1100-1550°C a viskozit 5-400 Pas.

# STRUCTURE OF SILICATE OXYNITRIDE MELT DOPED WITH SCANDIUM, YTTRIUM AND LANTHANUM: A MD DFT SIMULATION

JAN MACHÁČEK, ONDREJ GEDEON, MAREK LIŠKA\*, SOŇA CHARVÁTOVÁ

*Department of Glass and Ceramics, Institute of Chemical Technology, Technická 5, 166 28 Prague, Czech Republic*

*\*Vitrum Laugaricio, Joint Glass Center of Institute of Inorganic Chemistry of SAS,*

*Alexander Dubček University of Trenčín and RONA, j.s.c., Študentská 2, Trenčín, 911 50, Slovak Republic*

E-mail: Jan.Machacek@vscht.cz

Submitted November 29, 2005; accepted January 16, 2006

**Keywords:** Oxynitride glass, MD DFT simulation, Scandium, Yttrium, Lanthanum

*The MD DFT simulations of three oxynitride systems (Mg–M–Si–O–N, M = Sc, Y, La, 20 eq.% of N) were carried out. The results in the form of RDF and a coordination number were compared with the available experimental data and a good agreement was found. The main features of the experimental total RDFs were identified by means of the partial RDF originating from the simulations. Calculated coordination numbers of anions and cations were compared with the experimental data measured on both glasses and crystalline phases. It was confirmed that MD DFT can be used for bulk simulations of multi-component glassy oxynitride systems with quite reasonable results. Some discrepancies in Si–O and Si–N distances were attributed mainly to higher temperature and limited size of the systems.*

## INTRODUCTION

Oxynitride glasses occur as grain-boundary phases in nanostructured silicon nitride ceramics and dramatically influence its mechanical strengths [1, 2]. Therefore, the investigation of their structure and properties is lead not only by the theoretical interest but primarily by the strong technical impact. In early studies related to the refining of glass melts, small concentrations of nitrogen in silicate glasses were reported to increase their softening temperature, viscosity and resistance to devitrification [2, 3]. However, till now the relationship between physical properties and the structure of oxynitride glass is not fully understood [4, 5].

Atoms in oxynitride glasses are usually considered to be cations and anions. The amount of the particular ion can be alternatively quantified by the equivalent percentage, which expresses the relative contribution of the cationic/anionic charge. For example, the concentration of nitrogen expressed in equivalent percents yields

$$\text{eq.\% of N} = \frac{3[\text{N}]}{2[\text{O}] + 3[\text{N}]} \quad (1)$$

where [N] and [O] are atomic concentrations, 2 and 3 are valences. Similarly, eq.% of O or eq.% of cations can be expressed as well. It was found that the glass forming region for oxynitride glasses is quite narrow and rarely exceeds 25 eq.% of N [2].

If nitrogen is substituted for oxygen the silicate structure becomes stiffer due to higher valency (-III) of nitrogen. In principle, three bonding possibilities should be considered:



The case a) reflects the situation in glassy and crystalline systems with no alkali or alkali-earth modifier. When a modifier is added, the cases b) and c) will happen in the structure. Simultaneously, with formation of b) and c) type structures the non-bridging oxygens (e.g.  $\equiv\text{Si}-\text{O}^-$ ) are formed in this case.  $^{15}\text{N}$  MAS-NMR and neutron diffraction show that in sodium-silicate (20 mol.%  $\text{Na}_2\text{O}$ ) glasses with 4 at.% of N [3] the cases a) and b) predominate.  $^{29}\text{Si}$  MAS-NMR measurements revealed that a silicon atom binds more than one nitrogen atom very unwillingly, at least for the measured system (20 eq.% of N, 80 eq.% of O, 20 eq.% of Mg, 20 eq.% of La, 60 eq.% of Si) [4]. It was suggested [6] that, while Mg is a network modifier in oxide systems and is usually 6-coordinated, in oxynitride glasses it acts as a network former (or intermediate), being 4-coordinated. As a rule of thumb, cationic modifiers (such as column III elements and lanthanides) with higher cationic field strength (CFS) increase strength of the silicate structure [4, 7].

In many cases, MD simulations help with interpretation of the experimental data [8, 9]. Recently, experimental investigations on oxynitride glasses were com-

pleted with atomistic computer simulations [10-12]. However, molecular dynamics simulations with empirical force fields are seldom able to describe interatomic polar covalent bonds with an acceptable accuracy. It seems that the most difficult task is the deriving of interatomic potential functions describing correctly the first coordination spheres of the network-forming atoms, e.g. N, B, P, Al, Si. Thus, in comparison with classical simulations of oxynitride glasses [10-12], more precise and more promising simulations can be performed with atomic forces calculated with help of density functional theory (MD DFT) [13]. Despite such simulations comprise only about a hundred particles and only a short time interval can be studied, typically tens of picoseconds, it was shown that even such limited calculations suffice for establishing of the short range ordering (SRO) of atoms in amorphous systems [14, 15]. Atomistic simulations enable to calculate various physico-chemical properties of the studied system and they can be directly compared with the experimental results e.g. radial distribution functions (RDF), structure factor, distribution of Q-species, diffusion and viscosity coefficients, elastic moduli, IR spectrum, etc.

The aim of this study is to perform MD DFT simulations of silicate oxynitride systems containing magnesium and the column III elements - scandium, yttrium, and lanthanum. Our work follows the extensive experimental research carried out by Lofaj and co-workers [4, 5, 16].

## COMPUTATIONAL DETAILS

The composition of the simulated systems Mg–M–Si–O–N (M = Sc, Y, La) were as follows: 21.33 eq.% of Mg, 20.00 eq.% of M, 58.67 eq.% of Si, 80.00 eq.% of O, 20.00 eq.% of N. It corresponds to 42.1 mol.% of MgO, 13.2 mol.% of M<sub>2</sub>O<sub>3</sub>, 38.2 mol.% of SiO<sub>2</sub>, and 6.6 mol.% of Si<sub>3</sub>N<sub>4</sub>. The systems were simulated in cubic computational cells with periodic boundaries. The box volumes were determined by the experimental densities of the corresponding glasses (table 1). The total number of ions in each computational box was 118 (10 N, 60 O, 16 Mg, 10 M, and 22 Si).

The simulation procedure consisted from preparation of reasonably chemically ordered systems which were used as input for MD DFT simulation. The classi-

cal MD was used for this initiation procedure and only the yttrium containing system was subjected to above procedure. The other two systems were prepared for MD DFT simulation start by replacement of yttrium atoms by scandium or lanthanum followed by geometry relaxation performed by MD DFT. Thus the simulation procedure may be decomposed in the following detailed steps:

- 1) The positions of atoms in a simulation cell were randomised at 5000 K during 10000 steps using classical MD with time step of 0.001 ps.
- 2) The randomised structure entered the classical MD simulation [17]. The system was cooled down to 300 K to obtain the structure of "some chemical order".
- 3) The obtained ion positions were taken as an input for a MD DFT simulation using Hellmann-Feynman forces. The time-step of a numerical solution of the equations of motions was set to 0.001 ps. The system was relaxed for 7.5 ps at 4000 K and was treated as an NVT ensemble. The temperature was scaled at each 0.05 ps.
- 4) Up to now, only the system with Y was simulated. For other two studied systems, at this point, the Y ions were replaced by Sc/La. All ion coordinates were linearly rescaled according to the room temperature densities of Sc/Y/La oxynitride glasses (table 1).
- 5) Additional MD DFT runs (5 ps) were performed for Sc and La systems with a temperature scaling followed by NVE relaxations for 3 ps. As an example, the time evolutions of temperature, total energy, and potential energy for Sc system are shown in figure 1.
- 6) The temperature of all systems were numerically rescaled to 2000 K. Temperature was scaled for 2.5 ps

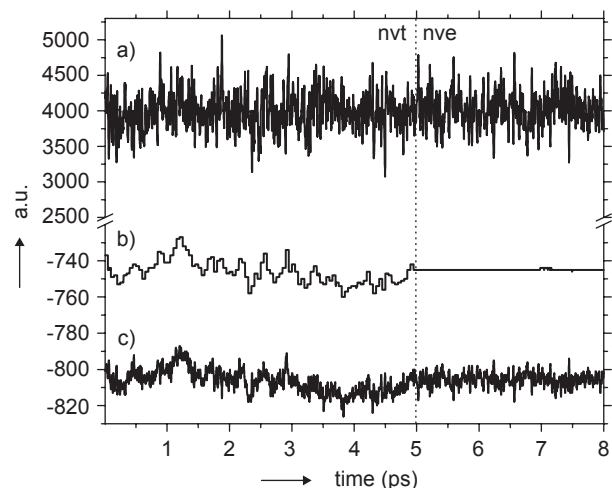


Figure 1. Temperature (K) - (a), total energy (eV) - (b), and potential energy (eV) - (c) evolutions in Sc-system at 4000 K. The dotted line separates the constant temperature (NVT) and the following constant total energy (NVE) modes.

Table 1. Room temperature densities [4] of studied Mg–M–Si–O–N (M = Sc, Y, La) oxynitride systems.

M	Density (g/cm <sup>3</sup> )	Simulation box size (Å)
Sc	3.096	11.109
Y	3.545	11.196
La	3.972	11.348

in MD DFT run (NVT) to ensure no temperature drift would be observed after switching the temperature scaling off.

7) Finally, 2.5 ps runs were completed under constant total energy conditions (NVE). During the runs the radial distribution functions were collected every 0.05 ps. The radial step of 0.057 Å was used for RDF accumulation.

The MD DFT calculations of the bulk oxynitride systems were performed using the Vienna ab-initio simulation package VASP [18]. The valence-electron wavefunctions were expanded in plane waves. The Kohn-Sham equations of density-functional theory (DFT) were solved using generalized gradient approximation (GGA) adapted by Perdew, Burke and Ernzerhof (PBE). All-electron wave functions were used to describe the electron-ion interaction as derived from ultrasoft pseudopotentials [19] via projector augmented wave technique (PAW). The potential energy calculations in scandium, yttrium and lanthanum systems were performed with plane-wave cut-offs of 250 eV, 213 eV, and 250 eV, respectively. The cut-offs correspond to the maxima of the minimal values recommended for DFT molecular dynamics among atoms present in the oxynitride systems. Brillouin-zone sampling was restricted to the  $\Gamma$ -point only.

## RESULTS

No remarkable energy drifts of NVE ensembles were observed both at 4000 K and 2000 K. The total energy was perfectly conserved and therefore the time-step of 0.001 ps seems to be quite reasonable even at the highest used temperature (figure 1). Moreover, the potential energies were also kept constant what may serve as an indication that the major structural rearrangements faded out. The interpretation of hereafter presented results presumes that the short range ordering in the oxynitride systems is formed very quickly at an extremely high temperature and does not depend on a simulation time scale too much. This assumption is in har-

mony with the results of classical MD simulations [9]. Using of the above assumption enables significant time shortening of the performed MD DFT simulations. The reason for performing as short as possible simulations dwells in enormous computational demands of DFT. The size of a simulated system represents even more limiting factor, because the DFT algorithm scales as  $N^3$ , where  $N$  is the number of particles.

The snapshot of the simulated Sc-system is presented in figure 2. Such images may be useful for the first inspection of the structure, e.g. provide an initial hint on homogeneity and/or warn of the unusual coordinations. It is seen that the atoms in the Sc-system are reasonably distributed without a visible separation of the nitrogen phase. Although not presented here, other systems (Y- and La-) offer similar pictures.

As the snapshots are not suitable for the quantitative analyses, a comparison of the simulated and the experimental RDFs is given in figure 3. Experimental data for scandium and lanthanum oxynitride systems (20 eq.% of N, 80 eq.% of O, 60 eq.% of Si, 20 eq.% of

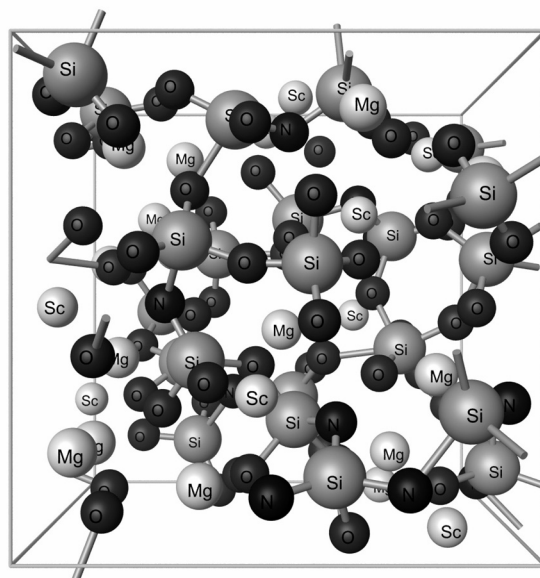


Figure 2. Structure of the simulated Sc-system.

Table 2. Positions of the maxima of the first peaks of pair RDFs. Average bond length (Å) in some common crystalline nitrides are denoted with asterisk [23].

System	N-					O-						
	N	O	Mg	M	Si	O	Mg	M	Si	Mg-Mg	M-M	Si-Si
Sc	3.06	2.83	2.17	2.11	1.78	2.67	2.00	2.11	1.67	3.28	3.55	3.00
Y	2.85	2.85	2.07	2.41	1.79	2.69	2.02	2.30	1.68	3.13	3.97	3.02
La	2.89	2.84	2.16	2.50	1.76	2.78	1.99	2.44	1.70	3.29	3.97	3.01
Sc*			2.13	2.22	1.73							
Y*				2.43								
La*				2.57								

Mg, 20 eq.% of M) were obtained by neutron diffraction at room temperature [16]. The yttrium system was not measured. Positions of the maxima of peaks corresponding to the particular X-Y pairs, summarized in table 2, are depicted in the figure 3 to identify the main contributions. The peaks of RDFs are not clearly separated what embarrasses the determination of the local structure of glassy systems. However, the main features can be identified on both the simulated and experimental RDFs. The simulated RDFs reveal similar behaviour as the experimental ones; however, the peaks coming from simulations are broader due to the higher temperature. The peaks of the first maxima are systematically shifted to a longer radius (about 4.3 %) and their right-hand shoulder is contributed by Mg–O/N (and M–O/N in case of Sc-system).

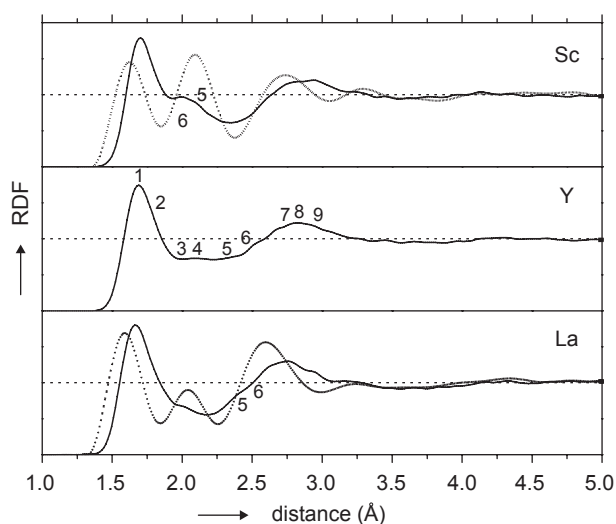


Figure 3. Total radial distribution functions of the scandium, yttrium, and lanthanum systems. DFT MD results are sketched by the solid lines; experimental results [16] by the dashed lines. The main features of the curves were identified with help of the simulated pair RDFs as follow: 1 Si–O, 2 Si–N, 3 Mg–O, 4 Mg–N, 5 M–O, 6 M–N, 7 O–O, 8 N–O and N–N, 9 Si–Si. For the sake of simplicity, only M–O and M–N peaks are marked in Sc- and La-systems.

In case of the Sc- and La-systems, one unstable N–N bond (of length 1.6 Å) was observed in several atomic configurations. However, such arrangement is highly unstable in a system with a low content of nitrogen. In the amorphous  $\text{SiO}_2\text{:Si}_3\text{N}_4$  system, there was observed much higher willingness of N towards formation of N–N bonds [13].

Coordination numbers were obtained by the integration of the pair RDFs up to their first local minima. The obtained results, including upper integration bounds, are presented in table 3. As expected, the partial coordination M–O increases with the increasing ionic diameters of column III elements. Scandium, yttrium, and lanthanum cations are coordinated by 6.6, 7.5, and 8.9 anionic neighbours, respectively. However, the number of coordinating nitrogen anions is not monotonous. The highest amount of nitrogen is coordinated to scandium, that is the smallest among the studied modifiers. Then abrupt drop of the number of N around Y is observed followed by the expected increase in case La due to the increase of the ion size. The magnesium coordination sphere remains unchanged in all systems studied. This contains less than one nitrogen anion within 5.6 total neighbouring anions. The coordination sphere of a silicon atom remains approximately the same for all systems. Silicon binds 4.1 anions from which 0.8 are N. The coordination number of nitrogen is very close to 4. Most of nitrogen atoms are connected to two silicon atoms. For M and Mg, nitrogen slightly prefers bonding to magnesium. The coordination number of oxygen is roughly 3.5. Vast majority of oxygen atoms are non-bridging oxygens.

## DISCUSSION

The simulated and the experimental total RDFs reveal similar features. Peaks of the experimental RDFs can be identified with help of MD simulation. On the other hand, some striking discrepancies arise when a quantitative comparison is required. While the peak widening of simulated RDFs can be attributed to the

Table 3. Coordination numbers and the first local minimum distances (Å) (in parentheses) of X–Y pairs.

System	Si–N	Si–O	M–N	M–O	Mg–N	Mg–O
Sc	0.7 (2.33)	3.5 (2.33)	1.3 (3.16)	5.4 (3.11)	0.8 (3.05)	4.7 (2.83)
Y	0.9 (2.29)	3.2 (2.35)	0.7 (3.30)	6.9 (3.19)	0.8 (3.07)	4.9 (2.85)
La	0.8 (2.32)	3.3 (2.32)	0.9 (3.34)	7.8 (3.46)	0.9 (3.00)	4.8 (2.89)
System	N–Si	N–M	N–Mg	O–Si	O–M	O–Mg
Sc	1.5 (2.33)	1.3 (3.17)	1.3 (3.06)	1.3 (2.33)	0.9 (3.11)	1.3 (2.83)
Y	2.0 (2.30)	0.6 (3.30)	1.3 (3.08)	0.9 (2.35)	1.1 (3.19)	1.3 (2.85)
La	1.8 (2.33)	0.9 (3.35)	1.4 (3.01)	1.2 (2.32)	1.3 (3.46)	1.3 (2.89)

influence of higher temperature, the 0.07-Å-drift of the first peak belonging to Si–O and Si–N pairs can be discussed such way only partly. Probably, a coincidence of more effects happens during a calculation. Among them, size of the system, incompleteness of a wave function basis set and premises of DFT should play a certain role. The over-coordinated silicon atoms are considered to be another important factor influencing Si–O distance. At this point, additional testing is to be carried out. We have tested the DFT methodology implemented in the VASP programme on silicate clusters:  $H_4SiO_4$ ,  $H_6Si_2O_7$ ,  $H_3SiO_3N$ ,  $H_7Si_2O_6N$ , and  $H_9Si_3O_9N$  (table 4). We have found our results to be in agreement with post Hartree-Fock quantum calculations [20, 21]. It seems that the Si–O and Si–N distances are usually rather longer in clusters than in a bulk material. We can speculate the main contribution, which prolongs the first RDF peak, to be the size of a simulation box. On the other hand, no difference in the first peak positions of the large (6000 atoms) and small (117 atoms)  $Na_2O \cdot 2SiO_2$  glassy systems modeled with empirical Buckingham potentials was observed [22].

Average interatomic distances correspond to the first maxima of the pair RDFs (table 2). Except for M–X lengths no significant differences among the simulated systems were found (up to 5 %). Thus, the major changes are caused by the increasing ionic diameter of Sc, Y, and La ions. The calculated M–N distances are in good agreement with the tabulated values of crystalline nitrides [23].

An additional piece of information to the experimental results offers the analysis of coordination numbers (table 3). There are some common features throughout the systems. In all systems, the coordination number of silicon slightly exceeds four. Not only  $SiO_4$  tetrahedra but also  $SiO_5$  trigonal bi-pyramids were

observed in the simulated oxynitride melt. Such unusual units are believed to act as intermediates of high temperature transport processes in a melt [24, 9]. Number of over-coordinated silicon atoms decreases with the increasing ionic radius of M. Similar behaviour was observed in potassium-, rubidium- and caesium-silicate glasses modelled by classical MD simulations [25, 9] and by  $^{29}Si$  MAS-NMR [24]. Larger cations are weakly bound to the silicate network, decrease rigidity and viscosity [5] of the structure. Therefore, high-temperature diffusive processes proceed more readily and formation of  $SiO_5$  defects is suppressed [25].

A silicon atom is mostly bound to three oxygen atoms and one nitrogen atom. It seems consistent with the published results [5] where  $SiO_3N$  units dominate in the structure of oxynitride glass.

The crystalline  $Si_3N_4$  phases contain only 3-coordinated nitrogen. However, in the oxynitride systems presented in this study, the coordination number of nitrogen is very precisely four, as it is in ionic crystalline nitrides [23]. It is not surprising if we consider chemical composition of systems contained a huge amount of MgO and  $M_2O_3$ . Nitrogen atoms bind approximately 1.8 silicon atoms. The formation of  $\equiv Si-N-Si \equiv$  and  $\equiv Si-N^2-$  units is preferred (see figure 2). It is in agreement with the present-day concept of the nitrogen role in the silicate structure [2, 7]. Nearly all oxygen atoms are non bridging oxygens (NBO), bridging oxygens (BO) form only lesser part of the structure. The equivalent binary metasilicate system ( $MgO \cdot SiO_2$ , i.e. 40 eq.% of Mg, 60 eq.% of Si, 100 eq.% of O) contains 2/3 of NBO and 1/3 BO.

Differences in coordination numbers throughout the systems do not seem to be conclusive enough. Larger M cations prefer oxygen in their coordination spheres, i.e. N/O ratio decreases. On the other hand, N/O ratio in the Mg coordination sphere is invariant with respect to a column III cation diameter. In most cases, the coordination number of Mg in crystalline magnesium oxides and silicates is 6. On the other hand, it equals 4 in magnesium nitrides. Therefore, the calculated average value 5.6 proves to be a superposition of these two values. The coordination number of Mg approaching 6 is in contradiction with ref. [6] which claims Mg atoms play rather a network forming than a network modifying role. Our simulations witness Mg to be a network modifier in oxynitride systems. Coordination number of Sc in crystalline materials [23] ranges from 5 to 8; the most frequent coordination number is 6. Y ranges from 6 to 7; mostly 7. La ranges roughly from 6 to 9, mostly 8. The calculated values slightly exceed tabulated data. It is quite common and can be explained by disordering in the oxynitride structure.

Table 4. Si–O and Si–N bond lengths (Å) in some oxynitride clusters. a) Our results obtained by DFT; b) RHF simulation [21]; c) experimental data cited in [20]; d) HF simulations cited in [20].

	Si–NBO	Si–BO	Si–N
$Si(OH)_4$	1.649 <sup>a)</sup> 1.643 <sup>b)</sup>		
$(HO)_3SiOSi(OH)_3$	1.647 <sup>a)</sup> 1.650 <sup>b)</sup> 1.657 <sup>b)</sup>	1.622 <sup>a)</sup> 1.624 <sup>b)</sup> 1.591 <sup>b)</sup>	
$H_3SiOSiH_3$		1.633 <sup>a)</sup> 1.634 <sup>a)</sup>	
$(HO)_3SiNH_2$	1.654 <sup>a)</sup>		1.711 <sup>a)</sup>
$(HO)_3SiNHSi(OH)_3$	1.653 <sup>a)</sup> 1.660 <sup>b)</sup>		1.721 <sup>a)</sup> 1.691 <sup>b)</sup>
$N[Si(OH)_3]_3$	1.652 <sup>a)</sup> 1.660 <sup>b)</sup>		1.746 <sup>a)</sup> 1.719 <sup>b)</sup>

## CONCLUSION

The DFT MD simulations of three oxynitride systems (Mg–M–Si–O–N, M = Sc, Y, La, 20 eq.% of N) were carried out. The results in the form of RDF and a coordination number were compared with the available experimental data and the good agreement was found. The main features of the experimental total RDFs were identified by means of the partial RDF originating from the simulations. Coordination numbers of anions and cations were calculated and compared with the available data measured on both glasses and crystalline phases. This work confirmed that DFT MD can be used for bulk simulations of multi-component glassy oxynitride systems with quite reasonable results. Some discrepancies in Si–O and Si–N distances were attributed mainly to higher temperature and limited size of the simulated systems.

## Acknowledgement

This work was supported by the Slovak Grant Agency for Science through the grant No. 1/0218/03 and by the Grant Agency of the Czech Republic through the grant No. 104/06/0202. It was also part of research programme MSM 6046137302 Preparation and research of functional materials and material technologies using micro- and nanoscopic methods. The super-computing centre of Czech technical university contributed with the necessary computing facilities. The authors (J.M. & O.G.) also acknowledge Integrated Centre for Advanced Materials and Molecular Science (IIC-Matmol) in Bratislava (SK) for the fruitful collaboration.

## References

- Satet R. L., Hoffmann M. J.: *J.Eur.Ceram.Soc.* 24, 3437 (2004).
- Hampshire S.: *J.Non-Cryst.Solids* 316, 64 (2003).
- Sakka S.: *J.Non-Cryst.Solids* 181, 215 (1995).
- Lofaj F., Satet R., Hoffmann M. J., de Arellano López A. R.: *J.Eur.Ceram.Soc.* 24, 377 (2004).
- Lofaj F., Dériano S., LeFloch M., Rouxel T., Hoffmann M. J.: *J.Non-Cryst.Solids* 344, 8 (2004).
- Jack K. H.: cited in Hampshire S.: *J.Non-Cryst.Solids* 316, 64 (2003).
- Hampshire S., Pomeroy M. J.: *J.Non-Cryst.Solids* 344, 1 (2004).
- Soules T. F.: *J.Non-Cryst.Solids* 123, 48 (1990).
- Macháček J.: Ph.D. thesis, in Czech (2005).
- Umesaki N., Hirosaki N., Hirao K.: *J.Non-Cryst.Solids* 150, 120 (1992).
- Macháček J., Liška M., Gedeon O.: *Glastech.Ber.Glass Sci.Technol.* 77C, 406 (2004).
- Yoshiya M., Tatsumi K., Tanaka I., Adachi H.: *J.Am. Ceram.Soc.* 85, 109 (2002).
- Kroll P.: *J.Non-Cryst.Solids* 345-346, 720 (2004).
- Kresse G.: *J.Non-Cryst.Solids* 192-193, 222 (1995).
- Kresse G.: *J.Non-Cryst.Solids* 205-207, 833 (1996).
- Lofaj F.: neutron scattering measurements, unpublished results.
- Smith W.: The DL\_POLY molecular simulation package, [http://www.cse.clrc.ac.uk/msi/software/DL\\_POLY/](http://www.cse.clrc.ac.uk/msi/software/DL_POLY/), Daresbury 2003.
- Kresse G., Furthmüller J.: *Phys.Rev. B* 54, 11169 (1996).
- G. Kresse, and J. Joubert, *Phys.Rev. B* 59, 1758 (1999).
- Lazarev A. N.: *Molecular approach to solids*, Elsevier, Amsterdam 1998.
- Murakami M., Sakka S.: *J.Non-Cryst.Solids* 101, 271 (1988).
- Macháček J.: unpublished results.
- Gmelin Institute/FIZ Karlsruhe (1997), International crystal structure database/Retrieve, version 2.01.
- Stebbins J. F., McMillan P.: *J.Non-Cryst.Solids* 160, 116 (1993).
- Macháček J., Gedeon O., Liška M.: *Transactions of the VŠB - Technical University of Ostrava* 48, 167 (2005).

STRUKTURA KŘEMIČITÝCH OXYNITRIDOVÝCH  
TAVENIN DOPOVANÝCH SKANDIEM, YTRIEM  
A LANTANEM: MD DFT SIMULACE

JAN MACHÁČEK, ONDREJ GEDEON,  
MAREK LIŠKA\*, SOŇA CHARVÁTOVÁ

Ústav skla a keramiky, Vysoká škola chemicko-technologická,  
Technická 5, CZ-16628 Praha, Česká Republika  
\*Vitrum Laugaricio, centrum kompetencie skla,  
spoločné pracovisko Ústavu anorganickej chémie SAV,  
Trenčianskej univerzity Alexandra Dubčeka v Trenčíne  
a RONA a.s., Študentská 2, Trenčín, SK-911 50,  
Slovenská Republika

Byla provedena MD DFT simulace třech oxynitridových systémů (Mg–M–Si–O–N, M = Sc, Y, La, 20 eq.% N). Výsledky ve formě RDF a koordinačních čísel byly srovnány s dostupnými experimentálními daty a byla zjištěna dobrá shoda. Hlavní píky experimentálních RDF byly identifikovány pomocí parciálních RDF získaných ze simulací. Vypočítaná koordinační čísla anionů a kationů byla srovnána s experimentálními daty naměřenými u skel i krystalických fází. Bylo potvrzeno, že metoda MD DFT může být použita pro modelování více-složkových skelných oxynitridových systémů, a to s rozumnými výsledky. Zjištěné nesrovnalosti v délkách vazeb Si–O a Si–N byly připisány hlavně vyšší teplotě a omezené velikosti simulovaných systémů.

# CORROSION OF E-GLASS FIBERS - SECURITY FACTOR OF NUCLEAR POWER PLANTS

LUCIA MIŠÍKOVÁ, DAGMAR GALUSKOVÁ

*Vitrum Laugaricio - Joint Glass Center of IIC SAS, TnU AD and RONA a.s.  
Študentská 2, 911 50 Trenčín, Slovak Republic*

E-mail: galuskova@tnuni.sk

Submitted January 17 2006; accepted February 17, 2006

**Keywords:** E-glass fibers, Corrosion, Flow-through leaching tests

*The flow-through leaching experiments have been conducted at two buffered pH values (8.5 and 10.0) of borate leaching solutions and at two temperatures (70°C and 90°C) on the EUTAL glass fibers, used as an insulation in nuclear power plants. Time dependencies of the total amount of leached elements Si, Al and Ca in corrosive solution have been determined. From the leaching rates in stationary conditions the values of activation energies,  $E_a$ , have been calculated. Lower  $E_a$  values were found for leaching at higher pH value. Higher  $E_a$  values were found for atoms so called network-forming oxides (Si, Al). Surface of corroded fibers was analyzed by scanning electron microscopy with energy dispersive X-ray analysis (SEM/EDX). Formation of relatively smooth continuous surface layer of corrosion products was detected at higher pH value.*

## INTRODUCTION

In case of an accident the emergency system of a nuclear power plant is used in order to preserve pressure of a coolant in the primary cooling circuit and to dispose heat from the active zone of nuclear reactor. The system consists of the tanks filled with the boric acid solution and the pumps transporting solution to the primary cooling area. Moreover the low-pressure pumps are activated when the tanks are not able to bring the cooling water into the system. After pumping out, water is pumped in again from the heat exchanger placed at the bottom of the hermetic boxes. Loss of coolant accident - LOCA (damage of the primary cooling area) causes rapid increase of pressure in the hermetic boxes. Therefore the spraying system is activated. Required decrease of pressure is achieved by spraying the area of the hermetic boxes and by condensation of steam and air mixture [1].

The glass fibers play a significant role regarding the security system of the nuclear plants. Glass fibers are mainly used as thermal and electrical insulation and in case of accident fibers get in immediate contact with cooling solution. It is well known that water solution in contact with a glass causes changes resulting in the structure transformation of glass surface, dissolution of a glass itself and formation of new glass surface layer [2]. Intensity of this phenomenon depends on well known factors. To the most important belong composition of the corrosive solution, its  $pH$  and temperature, and exposure time. In the case of LOCA, the glass fibers used as insulation are exposed to very aggressive environment for a relatively long time. Corrosion products

can plug filtering devices of the cooling system and consequently prevent pumping of a coolant from the hermetic boxes. This causes insufficient even functionless circulation of the cooling solution during accident. To assure safety of the cooling system is important to describe behavior of the glass fibers in the environment meeting aggressive conditions, and to predict composition and behavior of created corrosion products due to the long-term contact of insulation with the corrosive medium.

## EXPERIMENTAL

The flow-through leaching tests have been conducted on the EUTAL glass fibers with the composition shown in table 1.

Table 1. Composition (wt.%) of the EUTAL glass fibers (main components).

SiO <sub>2</sub>	B <sub>2</sub> O <sub>3</sub>	Al <sub>2</sub> O <sub>3</sub>	CaO	MgO
54	5.3	14.3	22.9	1.5

To remove the lubrication, the glass fibers had been exposed to the temperature of 300°C in the furnace for one hour. Diameters of burned glass fibers were determined by the optical microscopy using the image analysis (LUCIA). The mean value of the fiber diameter was counted from the lognormal distribution of a thousand

fiber diameters. The specific surface of fibers was then calculated:

$$\frac{S}{m} = \frac{2}{\rho r} \quad (1)$$

The flow-through leaching tests had been carried out in a period of 10 days with the flow rate of 15 cm<sup>3</sup>/h at temperatures of 70°C and 90°C. As a leaching medium two borate solutions of different composition with buffering effect were used. The composition of buffering solutions is given in the table 2. First leaching solution marked as B meets composition of the cooling solution used in the nuclear power plant. The *pH* value of 8.5 at the temperature of 22°C was achieved by addition of KOH. The *pH* of second leaching solution marked as CP meeting value of 10.0 was assured by addition of KOH together with 6-(cyklohexylamino)-1-propanesulfone acid (CAPS). This highly alkaline solution was chosen in order to simulate more aggressive conditions for dissolution of the EUTAL glass fibers known for their high chemical durability in alkaline environment.

Table 2. Composition of the leaching media (g/l).

Abbreviation	B	CP
H <sub>3</sub> BO <sub>3</sub>	9.36	9.36
KOH	2.99	7.00
NH <sub>3</sub>	0.89	7.58
N <sub>2</sub> H <sub>6</sub> SO <sub>4</sub>	0.93	0.93
CAPS	-	2.00
<i>pH</i> at 22°C	8.5	10.0

Table 3. Experimental conditions of flow-through tests.

Weight of fibers in reactor	1.00 g
Volume of reactor	5.00 cm <sup>3</sup>
Density of fibers	2.644 g/cm <sup>3</sup>
Mean value of fiber diameter	11.2×10 <sup>-6</sup> m
Specific surface	0.133 m <sup>2</sup> /g
Flow rate of leaching solution	15 cm <sup>3</sup> /h

For each temperature and leaching medium four parallel experiments were performed. The concentrations of leached Si, Al, and Ca were determined by the atomic absorption spectrometry (it was impossible to determine the amount of leached boron in the solution due to significantly lower concentration comparing with boron presented in the initial solution). The corrosion layer created on the surface of elementary fiber and its composition were analyzed by the scanning electron microscopy with energy dispersive X-ray analysis.

## RESULTS AND DISCUSSION

The weight loss of glass fibers leached in the corrosive medium B at the temperature of 70°C for 10 days meets the value (5.2 ± 0.2) % and (6.8 ± 0.2) % in case of using the medium CP, whereas the weight loss of glass fibers exposed to medium B at the temperature of 90°C meets the value (15.0 ± 0.1)% and for medium CP the value (16.7 ± 0.1)%.

The total amount of leached elements and its normalized amounts determine the following equations [3,4]:

$$Q_i^t = c_i \frac{F}{S} \Delta t + Q_i^{t-\Delta t} \quad (2)$$

$$NL_i^t = \frac{c_i F \Delta t}{x_i S} + NL_i^{t-\Delta t} \quad (3)$$

where  $Q_i$  is the total amount of leached elements by unit glass surface area in time  $t$ ,  $S$  is the glass surface area in contact with the leaching solution,  $c_i$  is concentration of particular leached element in time  $t$ ,  $F$  is the flow rate, and  $x_i$  represents the weight fraction of  $i$ -th element in the glass. Comparison of  $NL_i$  values tells us about mechanism involved in dissolution of a given glass. In case of congruent dissolution the  $NL_i$  values are in mutual compliance unlike for incongruent dissolution. The time dependence of total amount,  $Q_i$ , and normalized amount,  $NL_i$ , of Si, Al, and Ca are plotted in figures 1 and 2.

Normalized amount of Ca at both temperatures and for both leaching solutions was higher as normalized amount of Si and Al. This fact is related to the position of Ca in the silicate network. Calcium modifies the silicate network and leaching of its ions is higher in confrontation with Al, which participate on formation of the silicate network.

Values of the initial and stationary leaching rates may be evaluated from experimental time dependencies of  $Q_i$  by graphical or numerical methods. The graphical method is not reliable for determination of the initial leaching rates, therefore the following empirical equation is commonly used [2, 5]:

$$Q_i = P_a (1 - e^{-R_i t}) + P_c t \quad (4)$$

Due to low thickness and quick formation of the calcium depleted surface diffusion layer in alkaline conditions, the obtained  $Q_i(t)$  dependences are almost perfectly linear (figures 1, 2) in the time scale studied. The simple linear regression model with non-zero intercept has to be used instead of the equation (5) in this case. The stationary leaching rate is then simply given by the slope of the regression line.

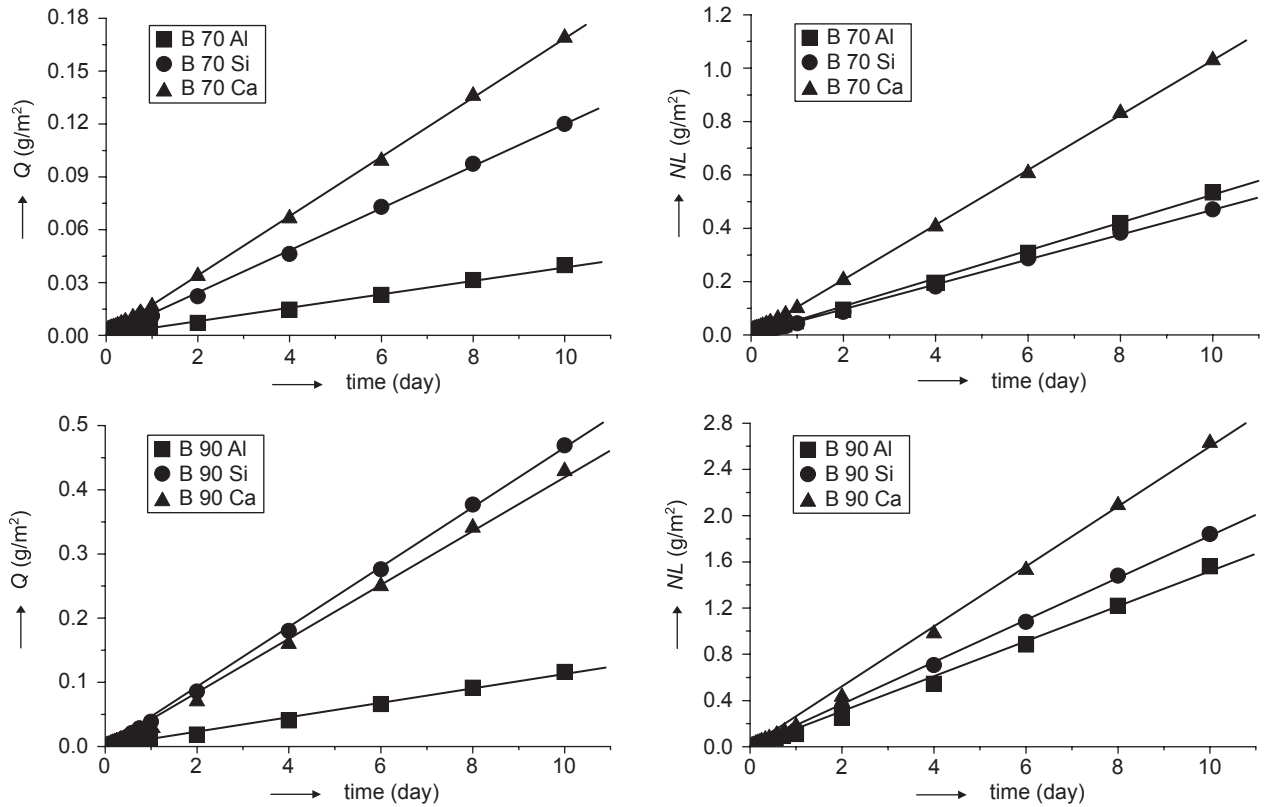


Figure 1. Time dependence of the amounts and normalized amounts of leached elements at temperatures 70°C a 90°C for leaching solution B. Lines represent the linear regression model.

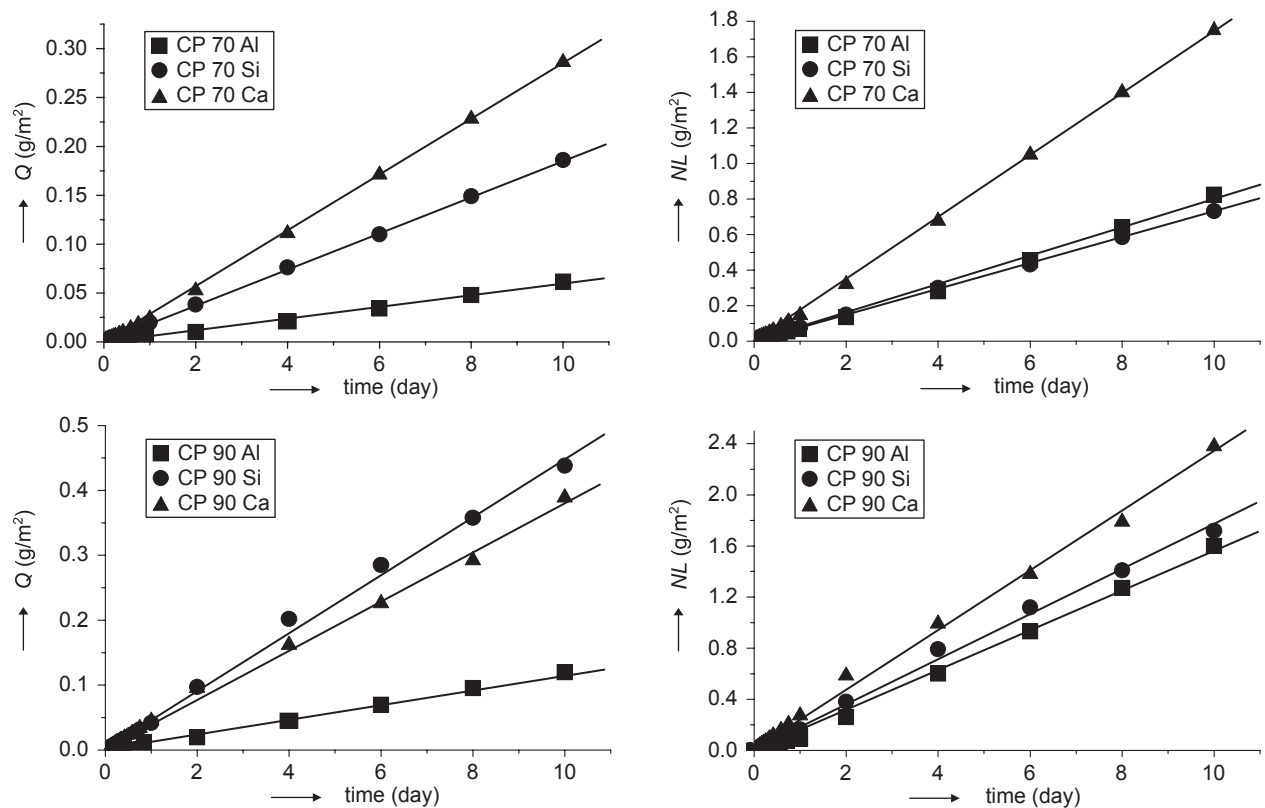


Figure 2. Time dependence of the amounts and normalized amounts of leached elements at temperatures 70°C a 90°C for leaching solution CP. Lines represent the linear regression model.

In alkaline environment when almost non-alkaline E-glass fiber had been leached, very thin diffusion layer is developed very fast. Alkaline solution in a contact with glass fiber surface causes fast breaking of Si–O–Si bonds followed by dissolution of silicate network as the rate controlling step of the corrosive process. The alkali metals, participating on the corrosive process as a diffusion component, are mostly not presented in the structure of the EUTAL glass. The obtained time dependences are practically linear after one hour of leaching. Therefore only the leaching rates in stationary conditions were evaluated. The values of the leaching rates in stationary conditions are summarized in table 4.

Table 4. Values of dissolution rates in stationary conditions and their standard deviations.

medium/ temperature	$v_{\infty}$ (Si) (mg/m <sup>2</sup> day)	$v_{\infty}$ (Al) (mg/m <sup>2</sup> day)	$v_{\infty}$ (Ca) (mg/m <sup>2</sup> day)
B 70	47.5 ± 0.7	52.8 ± 1.6	102.1 ± 2.7
B 90	185.2 ± 4.4	154.9 ± 1.0	262.9 ± 6.1
CP 70	73.5 ± 2.1	80.9 ± 1.9	175.4 ± 6.3
CP 90	176.9 ± 3.7	162.0 ± 3.6	231.4 ± 10.5

From the stationary leaching rates obtained for two distinct temperatures, the formal mean activation energy,  $E_a$ , was calculated from the Arrhenius equation:

$$v_{\infty} = A \cdot \exp(-E_a/RT) \quad (5)$$

Mean values of activation energies,  $E_a$ , and their standard deviations are shown in table 5. Standard deviations of  $E_a$  were calculated from four parallel experiments for each temperature. It can be concluded, that lower  $E_a$  values were found for leaching at higher pH value. On the other hand, higher  $E_a$  values were found for atoms of network-forming oxides (Si, Al).

Table 5. Values of mean activation energies and their standard deviations.

medium	$E_a$ (Si) (kJ/mol)	$E_a$ (Al) (kJ/mol)	$E_a$ (Ca) (kJ/mol)
B	72.3 ± 1.8	55.8 ± 0.8	49.0 ± 1.8
CP	45.5 ± 2.4	36.0 ± 1.4	14.4 ± 1.8

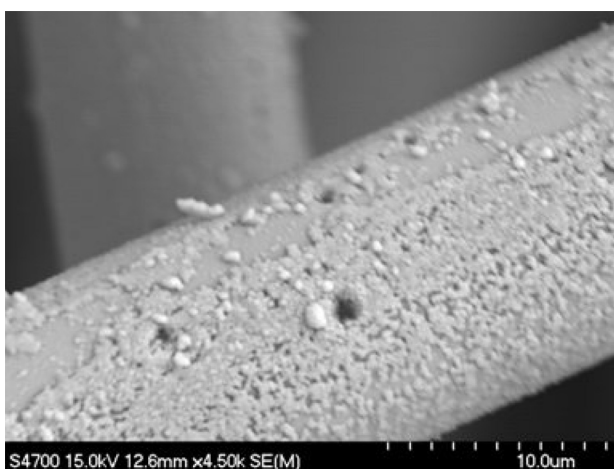
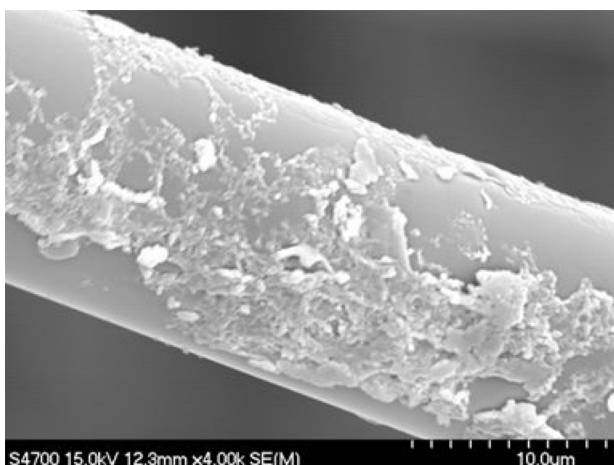


Figure 3. SEM micrographs of corroded fibers.

The presented figures (figure 3) obtained from SEM analysis indicate formation of the corrosive products on the surface of glass fibers. SEM/EDX analysis confirmed formation of alumino-silicate precipitated layer on the surface of corroded fiber. Observed layer on a glass fiber leached in the solution B is not as compact as in case of CP leaching solution.

## CONCLUSION

Performed flow-through leaching tests on the EUTAL glass fibers used as insulation in the nuclear plants confirmed the fact that the E-glass fibers show high chemical durability in alkaline solutions. Dissolution of the glass fibers used in our experiments is incongruent. The dissolution rate of Al and Si is almost the same. In the corrosive environment was observed back-precipitation of Si, Al and Ca elements participating on formation of a new layer on the fiber surface.

## Acknowledgement

*This work was supported by Agency for Promotion Research and Development under the contract No. APVV-20-P06405 and by the Slovak Grant Agency for Science under the grant No. VEGA 1/3578/06.*

References

1. <http://www.seas.sk/spolocnost/jadrova-bezpecnost/bezpecnost-prevadzky-je/>
2. Helebrant A., Matoušek J.: *Ceramics-Silikáty* 2, 173 (1988).
3. Helebrant A., Maryška M., Matoušek J.: *Sklář a keramik* 46, 164 (1996).
4. Jiříčka A., Helebrant A. Hamáčková J.: *Glass Sci. Technol.* 76, 298 (2003).
5. Helebrant A., Maryška M., Matoušek J., Tošnerová B.: *Bol.Soc.Esp.Ceram.Víd., 31C*, 87 (1992).

---

KORÓZIA SKLENÝCH VLÁKIEN - BEZPEČNOSTNÝ  
FAKTOR JADROVÝCH ELEKTRÁRNÍ

LUCIA MIŠÍKOVÁ, DAGMAR GALUSKOVÁ

*Vitrum Laugaricio - Spoločné pracovisko ÚACH SAV, TnU AD  
a RONA a.s., Študentská 2, 911 50 Trenčín, Slovak Republic*

Na sklených vláknach Eutal, používaných ako izolácie v jadrových elektrárňach, boli vykonané prietokové lúžiace experimenty. Testy prebiehali v dvoch pufrovaných roztokoch kyseliny boritej s  $pH$  8,5 a 10 a pri dvoch teplotách (70°C a 90°C). Boli zistené časové závislosti vylúhovania celkového množstva jednotlivých zložiek Si, Al a Ca do roztoku. Z rýchlostí lúhovania v ustálenom stave sa vypočítali hodnoty aktivačných energií,  $E_a$ . Nižšie hodnoty  $E_a$  sa stanovili pre lúhovanie sklených vlákien v roztokoch s vyšším  $pH$ . Vyššie hodnoty  $E_a$  boli nájdené pre atómy siet'otvorných oxidov (Si, Al). Povrch korodovaných vlákien sa sledoval pomocou skenovacej elektrónovej mikroskopie v kombinácii s mikroanalýzou (SEM/EDS). Pri vyšších hodnotách  $pH$  bol detekovaný vznik relatívne hladkej, kontinuálnej vrstvičky na povrchu korodovaných vlákien.

# PROPERTIES OF SELECTED ZIRCONIA CONTAINING SILICATE GLASSES

RADOVAN KARELL, JOZEF KRAXNER\*, MÁRIA CHROMČÍKOVÁ\*

*Faculty of Industrial Technologies, Alexander Dubček University of Trenčín,  
Ivana Krasku 491/30, Púchov, SK-020 01, Slovak Republic*

*\*Vitrum Laugaricio - Joint Glass Centre of the Institute of Inorganic Chemistry, Slovak Academy of Sciences,  
Alexander Dubček University of Trenčín and RONA, a.s., Študentská 2, Trenčín, SK- 911 50, Slovak Republic*

E-mail: karell@fpt.tnuni.sk

Submitted January 17, 2006; accepted February 17, 2006

**Keywords:** Viscosity, Density, Refractive index, Glass transition temperature, Zirconia-silicate glasses

*Viscosity, density, thermal expansion, glass transition temperature, refractive index, molar refraction, and chemical durability of  $15M_2O \cdot 10CaO \cdot xZrO_2 \cdot (75-x)SiO_2$  ( $M = Na$  for NCZ glasses, and  $M = K$  for KCZ glasses;  $x = 1, 3, 5,$  and  $7$ ) glasses were measured. The effect of  $SiO_2/ZrO_2$  equimolar substitution on measured physical and chemical properties was discussed. Increasing content of  $ZrO_2$  significantly improves the chemical durability against water in both studied glass series. The  $ZrO_2/SiO_2$  substitution strengthens the silicate network and therefore increases the values of glass transition temperature, and viscosity and decreases the value of the thermal expansion coefficient. Molar refractivity depends linearly on the  $ZrO_2$  content. The slope of the regression line is the same for both studied glass series, whereas the higher intercept for potassium glasses reflects the greater polarizability of the potassium cation with respect to the  $Na^+$  cation. In comparison with the NCZ glasses both the viscosity and the viscous flow activation energy of KCZ glasses are higher and their dependence on the  $ZrO_2$  content is steeper.*

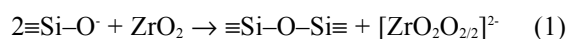
## INTRODUCTION

Silicate glasses containing zirconia play a significant role both in the igneous petrology [1] and glass technology [2]. Due to the non-toxicity and extremely high chemical durability in alkaline conditions these glasses are used for the production of alkali-resistant fibers for Portland cement composites [3]. Both the thermal expansion coefficient and the glass transition temperature are positively correlated with the  $ZrO_2$  content in silicate glass [4-6]. In addition to the chemical durability the high density, and high value of refractive index and dispersion predetermined these glasses for production of ecologically friendly barium- and lead-free crystal glass [7,8]. In addition to  $ZrO_2$ , other oxides of heavy elements as  $ZnO$  and  $TiO_2$  are used to substitute harmful lead- and barium-oxide. On the other side, zirconia increases the viscosity of the glass melt and the melting of the glass batch containing zirconium-containing raw materials (typically zircon) needs increased temperature and longer time. Thus, the corrosion of the refractory materials is more pronounced [2,9].

EXAFS studies of Zr coordination in selected silicate glasses have shown that variations in the local environment of Zr are relatively small [10]. In silicate glasses with lower  $ZrO_2$  concentrations (1-4 wt.%) Farges and Calas [11] found Zr to be mainly 6 coordi-

nated. The abundance of 6 coordinated Zr should increase with melt depolymerization as a result of the increasing network modifier content. With respect to the main coordination number, zirconia can be classified as network-modifying oxide according to the Zachariasens' rules. However its structural position strengthens the silicate network via forming the covalent Zr-O-Si bridges. Thus its influence on concentration dependence of various physical and chemical properties resembles the network-forming oxides. Therefore the literature information about the network-forming/modifying character of  $ZrO_2$  is relatively contradictory. For example, Ringwood [12] stated that  $ZrO_2$  is a network-former producing tetrahedral  $ZrO_4$  groups. Furthermore, Linthout [13] inferred that  $ZrO_2$  is a network modifier rather a network former based on crystal-chemical reasoning.

The possible structural model of 6-coordinated zirconium in silicate glasses suggested by Farges [10] on the basis of the EXAFS study consists in  $ZrO_6$  octahedron with four bridging and two non-bridging oxygen atoms (schematically  $[ZrO_2O_{2,2}]^2-$ ). Thus,  $ZrO_2$  not only takes part in the formation of the silicate network, but in addition it heals the broken Si-O-Si bridges according to the reaction:



This situation formally resembles the  $\text{Al}_2\text{O}_3$  network-forming structural activity where the non-bridging oxygen atoms of partially depolymerized silicate network are consumed by converting the  $\text{Al}_2\text{O}_3$  to tetrahedral anions  $[\text{AlO}_4]^-$  [2].

During the development of zirconia containing silicate glasses with targeted properties the multi-component, i.e. more than three-component, zirconia containing silicate systems are commonly studied [14-17]. However, the study of simpler model systems is needed to envisage the structure-property relationships with respect to the structural position of  $\text{ZrO}_2$  in the silicate glass and melt. Moreover, the thermodynamic models based on the regular solution theory can be simply constructed for simple oxide systems to verify the structural assumptions proposed on the basis of experimentally determined composition-property relationships [18]. The literature data concerning the composition - property relationships for more than three component zirconia containing silicate systems are relatively scarce [19,20]. Therefore the effect of the equimolar  $\text{ZrO}_2/\text{SiO}_2$  substitution in sodium-calcium and potassium-calcium trisilicate glasses  $15\text{M}_2\text{O} \cdot 10\text{CaO} \cdot x\text{ZrO}_2 \cdot (75-x)\text{SiO}_2$  ( $\text{M}=\text{Na}, \text{K}, x = 1, 3, 5, \text{ and } 7$ ) is in the scope of the present work.

## EXPERIMENTAL

The glass batches were prepared by mixing of powdered  $\text{Na}_2\text{CO}_3$  (AFT, p.a.),  $\text{K}_2\text{CO}_3$  (Fluka, p.a.),  $\text{CaCO}_3$  (AFT, p.a.),  $\text{ZrSiO}_4$  (Aldrich, p.a.) and  $\text{SiO}_2$  (AFT, min. 96,5 %). Sodium sulphate (AFT, p.a.) and potassium sulphate (Lachema, p.a.) were used as fining agents.

Glasses were melted in Pt-10%Rh crucible in supercanthal furnace at temperature of  $1600^\circ\text{C}$  for two-three hours in ambient atmosphere. The homogeneity was ensured by repeated hand mixing of the melt. The glass melt was then poured onto a stainless steel plate. The samples were tempered in a muffle furnace for one hour at  $650^\circ\text{C}$ , after which the furnace was switched off and samples allowed remain there until completely cool.

Theoretical composition and abbreviation of glass samples is summarized in table 1.

Thermal expansion coefficient of glass,  $\alpha_g$ , together with the glass transition temperature,  $T_g$ , were obtained by thermodilatometry (Netzsch, TMA 402) during cooling from sufficiently high temperature by the cooling rate of  $5^\circ\text{C}/\text{min}$ . The linear thermal expansion coefficient  $\alpha_g$  was obtained from the slope of the cooling curve in temperature interval  $400\text{-}450^\circ\text{C}$ . The experimental data for the NCZ0 glass were obtained in our previous work in the temperature interval  $350\text{-}450^\circ\text{C}$ .

The densities of glasses at laboratory temperature were measured by Archimedes method by dual weighting in air and in distilled water.

Refractive index was measured on polished prismatic glass samples by Abbe's refractometer at  $20^\circ\text{C}$ .

Chemical durability against distilled water, CD, was determined on grained sample according to the ISO norm [21] at  $98^\circ\text{C}$ . The values are given in  $\text{cm}^3$  of 0.01  $\text{mol}/\text{dm}^3$  hydrochloric acid needed for neutralisation of alkalis leached from 1 g of glass grains.

The low-temperature viscosities between  $10^8$  and  $10^{12}$   $\text{dPa}\cdot\text{s}$  were measured by thermo-mechanical ana-

Table 1. The composition and abbreviation of studied glasses (mol. %).

Glass	$\text{Na}_2\text{O}$	$\text{CaO}$	$\text{ZrO}_2$	$\text{SiO}_2$	Glass	$\text{K}_2\text{O}$	$\text{CaO}$	$\text{ZrO}_2$	$\text{SiO}_2$
NCZ0	15	10	0	75					
NCZ1	15	10	1	74	KCZ1	15	10	1	74
NCZ3	15	10	3	72	KCZ3	15	10	3	72
NCZ5	15	10	5	70	KCZ5	15	10	5	70
NCZ7	15	10	7	68	KCZ7	15	10	7	68

Table 2. Measured physical and chemical properties of studied glasses. Average standard error of measurement of density  $\pm 0.0001$   $\text{g}/\text{cm}^3$ , thermal expansion coefficient  $\pm 1 \cdot 10^{-7}/\text{K}^{-1}$  and refractive index  $\pm 0.0001$ .

Glass	$M_g$ (g/mol)	$\rho^{20}$ ( $\text{g}/\text{cm}^3$ )	$10^7 \alpha_g$ ( $\text{K}^{-1}$ )	$T_g$ (K)	$n_D^{20}$	$R_m$ ( $\text{cm}^3/\text{mol}$ )	CD ( $\text{cm}^3$ )
*NCZ0	59.97	2.4753	95	819	1.5140	7.29	-
NCZ1	60.69	2.5061	96	830	1.5193	7.35	$0.690 \pm 0.028$
NCZ3	62.13	2.5716	94	850	1.5319	7.49	$0.292 \pm 0.001$
NCZ5	63.57	2.6425	85	867	1.5463	7.62	$0.225 \pm 0.015$
NCZ7	65.02	2.7025	-	-	1.5598	7.78	$0.167 \pm 0.015$
KCZ1	65.52	2.4885	103	883	1.5191	7.99	$1.325 \pm 0.009$
KCZ3	66.96	2.5725	104	895	1.5352	8.11	$1.192 \pm 0.008$
KCZ5	68.41	2.6313	-	-	1.5471	8.25	$0.675 \pm 0.008$
KCZ7	69.85	2.6597	-	-	1.5524	8.40	$0.275 \pm 0.001$

\*values from previous unpublished work of Chromčíková.

lyzer (Netzsch TMA 402). The viscosity value,  $\eta$ , was calculated from the measured deformation rate  $d\varepsilon/dt$  and the known value of axial load  $G$  on orthorhombic (approx.  $5 \times 5 \times 20$  mm) sample with cross-section  $S$ :

$$\eta = \frac{G}{3S(d\varepsilon/dt)} \quad (2)$$

## RESULTS AND DISCUSSION

The measured values of density, thermal expansion coefficient, glass transition temperature, refractivity index, and chemical durability against water (CD, expressed in  $\text{cm}^3$  of  $10^{-2}$  molar HCl [21]) are summarized in table 2 together with the mean molar (formula) weight of glass,  $M_g$ , and molar refractivity calculated by:

$$R_m = \frac{(n_D^{20})^2 - 1}{(n_D^{20})^2 + 2} \frac{M_g}{\rho^{20}} \quad (3)$$

In the case of potassium glasses KCZ5 and KCZ7 as well as in the case of the sodium NCZ7 glass the glass transition region was partially above the experimentally accessible temperature range of thermodynamic measurement. Thus, the values of  $T_g$ , and  $\alpha_g$  were not measured for these glasses. As was expected, the chemical durability steeply increases (i.e. CD decreases) with increasing  $\text{ZrO}_2$  content in both kinds of studied glasses. On the other hand, the chemical durability is significantly lower for the potassium glasses, namely for low  $\text{ZrO}_2$  content, in comparison with the corresponding sodium ones. Also the density, glass transition temperature, refractive index and molar refractivity values are positively correlated with  $\text{ZrO}_2$  content in both studied compositional series. The steep increase of  $T_g$  with increasing  $\text{ZrO}_2$  content in silicate glasses was also reported by Takahashi [5], and Fisher [6]. With the

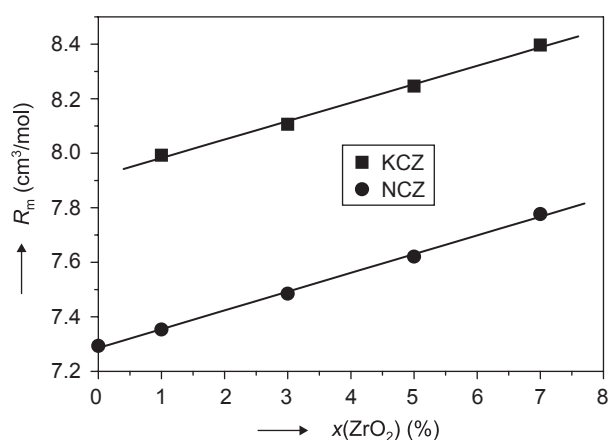


Figure 1. The dependence of molar refractivity on mole fraction of  $\text{ZrO}_2$ .

exception of NCZ0 glass, the thermal expansion coefficient of sodium glasses decreases with the increasing  $\text{ZrO}_2$  content. Probably the same is true for the potassium glasses, but the insufficient number of experimental data prevents the statistical confirmation of this idea. Similar tendency was confirmed by the work of Kheifets [4]. The thermal expansion coefficients of potassium glasses are about 10% higher in comparison with the sodium ones.

Figure 1 illustrates the dependence of molar refractivity of NCZ and KCZ glasses on  $\text{ZrO}_2$  content. It can be seen, that the almost perfect linear (correlation coefficient 0.9991 for NCZ glasses, and 0.9981 for KCZ glasses) correlation is obtained in both cases. The regression line

$$R_{m,NCZ} = [(7.286 \pm 0.007) + (0.0688 \pm 0.0017) \times (\text{ZrO}_2)] \text{ cm}^3/\text{mol} \quad (4)$$

describes the NCZ experimental data with standard deviation of approximation of  $0.010 \text{ cm}^3/\text{mol}$ . In the case of KCZ glasses the regression equation

$$R_{m,KCZ} = [(7.915 \pm 0.068) + (0.0676 \pm 0.0030) \times (\text{ZrO}_2)] \text{ cm}^3/\text{mol} \quad (5)$$

fits the data with standard deviation of  $0.013 \text{ cm}^3/\text{mol}$ . The  $\text{ZrO}_2$  content in the equations (4,5) is given in mole %. The slope of the regression line corresponds to the increment of molar refractivity caused by substitution of 1 mole % of  $\text{SiO}_2$  by  $\text{ZrO}_2$ . It is worth noting that in the limits of standard deviation the slope is the same for both glass series.

The temperature dependence of viscosity was described by the Arrhenius-like equation:

$$\log(\eta/\text{dPas}) = A + B/T \quad (6)$$

where  $A$ , and  $B$  are constants routinely determined by regression analysis, and  $T$  is thermodynamic tempera-

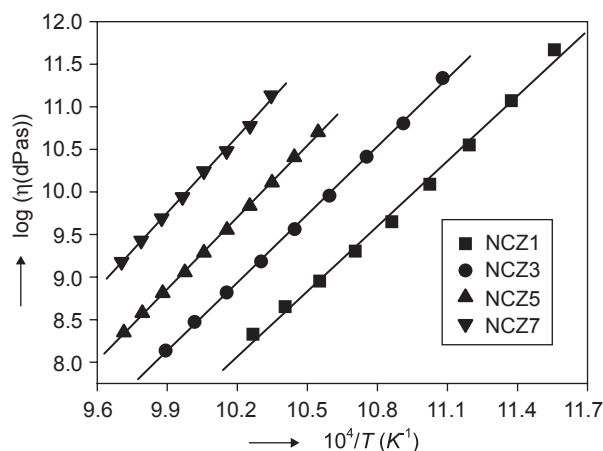


Figure 2. Arrhenius plot of viscosity - temperature dependence for NCZ glasses.

ture. The temperature independent viscous flow activation energy,  $E_a$ , was calculated by:

$$E_a = (\partial \ln \eta / \partial (1/T))_P = \ln(10)RB = 2.303RB \quad (7)$$

where  $R$  is the molar gas constant.

Experimental values of viscosity are plotted in  $\log(\eta/\text{dPa}\cdot\text{s})$  versus  $10^4K/T$  coordinate system in figure 2 for NCZ glasses, and in figure 3 for KCZ glasses. It can be concluded that all depicted dependences are linear with the isothermal viscosity value steeply increasing with increasing  $\text{ZrO}_2$  content, and with the slope moderately increasing with increasing  $\text{ZrO}_2$  content. Table 3 summarizes the values of  $A$ , and  $B$  coefficients (equation (6)), and the values of activation energy calculated according the equation (7). It can be seen that both  $A$ , and  $B$  values are increasing with increasing  $\text{ZrO}_2$  content in both glass series.

Figure 4 demonstrates the linear dependence of viscous flow activation energy on  $\text{ZrO}_2$  mole fraction. For NCZ glasses this can be described with the regression equation:

$$E_a(\text{NCZ}) = [(469 \pm 4) + (14.1 \pm 0.9) \times (\text{ZrO}_2)] \text{ kJ/mol} \quad (8)$$

with correlation coefficient of 0.9957 and standard deviation of approximation of 0.43 kJ/mol. For KCZ glasses the regression equation

$$E_a(\text{KCZ}) = [(529 \pm 12) + (38.3 \pm 4.1) \times (\text{ZrO}_2)] \text{ kJ/mol} \quad (9)$$

was obtained with the correlation coefficient of 0.9943 and standard deviation of approximation of 1.23 kJ/mol. It can be concluded that for KCZ glasses the activation energy is higher and its dependence on  $\text{ZrO}_2$  mole fraction is steeper.

### CONCLUSION

Increasing content of  $\text{ZrO}_2$  significantly improves the chemical durability against water in both studied glass series. The  $\text{ZrO}_2/\text{SiO}_2$  substitution strengthens the silicate network and therefore increases the values of glass transition temperature, and viscosity. The thermal expansion coefficient decreases with the increasing  $\text{ZrO}_2$  content. Molar refractivity depends linearly on the  $\text{ZrO}_2$  content expressed in mole %. The slope of the regression line is the same for both studied glass series, whereas the higher intercept for potassium glasses reflects the greater polarizability of the potassium cation with respect to the  $\text{Na}^+$  cation. In comparison with the NCZ glasses both the viscosity and the viscous flow activation energy of KCZ glasses are higher and their dependence on the  $\text{ZrO}_2$  content is steeper.

Table 3. Coefficients of the viscosity equation (equation (6)) and viscous flow activation energies (equation (7)) together with standard deviations and standard deviation of  $\log \eta$  approximation  $s_{\text{apr}}$ .

Glass	$A$	$B$	$E_a$ (kJ/mol)	$s_{\text{apr}}[\log(\eta \text{ dPa}\cdot\text{s})]$
NCZ1	$-17.97 \pm 0.76$	$25526 \pm 700$	$489 \pm 13$	0.087
NCZ3	$-18.26 \pm 0.29$	$26658 \pm 279$	$510 \pm 5$	0.032
NCZ5	$-18.99 \pm 0.23$	$28131 \pm 232$	$539 \pm 4$	0.020
NCZ7	$-19.78 \pm 0.51$	$29839 \pm 512$	$571 \pm 10$	0.031
KCZ1	$-20.26 \pm 0.41$	$29769 \pm 401$	$570 \pm 8$	0.034
KCZ3	$-22.68 \pm 0.57$	$33018 \pm 577$	$632 \pm 11$	0.028
KCZ5	$-26.50 \pm 0.57$	$37940 \pm 588$	$726 \pm 11$	0.023

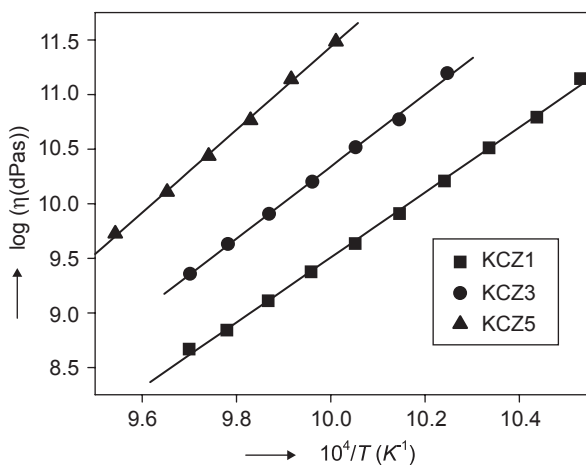


Figure 3. Arrhenius plot of viscosity - temperature dependence for KCZ glasses.

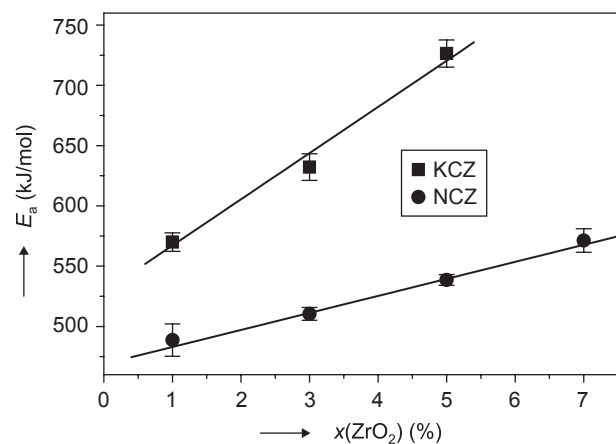


Figure 4. Dependence of viscous flow activation energy on mole fraction of  $\text{ZrO}_2$ .

Acknowledgement

*This work was supported by Agency for Promotion Research and Development under the contract APVV-20-P06405, and by the Slovak Grant Agency for Science under the grant VEGA 1/3578/06.*

References

1. Hofmann A. W.: Earth Planet Sci. Lett. 90, 297 (1988).
2. Vogel W.: Glass Chemistry, 2<sup>nd</sup> edition. Springer, Berlin 1994.
3. Proctor B. A., Yale B.: Phil.Trans.R.Soc. London A 294, 427 (1980).
4. Kheifets V. S., Shevyakov A. M., Tarlakov Yu. P.: In: *Mekhanicheskie i teplovye svoistva i stroenie stekla*, pp. 280-285, Moscow 1972 (in Russian).
5. Takahashi K., Mochida N., Yoshida Y.: J.Cer.Jpn. 85, 330 (1977).
6. Fisher J. G., James P. F., Parker J. M.: J.Non-Cryst. Solids 351, 623 (2005).
7. EU patent No. 91121730.5, 1991.
8. Czech patent No. WO 95/13993.
9. Volf M. B.: *Chemie skla*, SNTL, Praha 1971 (in Czech).
10. Farges F., Ponader C. W., Brown Jr., G. E.: Geochim. Cosmochim.Acta 55, 1563 (1991).
11. Farges F., Calas G.: Amer.Mineral. 76, 60 (1991).
12. Ringwood A. E.: Geochim.Cosmochim.Acta 7, 189 (1955); 7, 242 (1955).
13. Linthout K.: Contrib.Mineral.Petrol. 86, 155 (1984).
14. Liška M., Šimurka P.: Phys.Chem.Glasses 36, 6, (1995).
15. Liška M., Hulínová H., Šimurka P., Antalík J.: Ceramics-Silikáty 39, 20 (1995).
16. P. Šimurka, M. Liška, J. Antalík: Ceramics-Silikáty 39, 9 (1995).
17. Chromčíková M., Liška M., Karell R., Martiš V.: Chem.Listy 98, 584 (2004).
18. Liška M., Klement R., Macháček J., Gedeon O.: Phys. Chem.Glasses 46, 108 (2005).

19. INTERGLAD, Ver. 6., <http://www5.ngf.dion.ne.jp> (2005).
20. SciGlass-6.5, <http://www.scienceserve.com/Software/SciGlass/> (2005).
21. ČSN ISO 70 0531.

VLASTNOSTI VYBRANÝCH ZIRKONIČITANO-KREMIČITANOVÝCH SKIEL

RADOVAN KARELL, JOZEF KRAXNER\*,  
MÁRIA CHROMČÍKOVÁ\*

*Fakulta priemyselných technológií  
Trenčianskej univerzity A. Dubčeka,  
Ivana Krasku 491/30, Púchov, 020 01, Slovenská republika  
\*Vitrum Laugaricio - Centrum kompetencie skla  
Ústavu anorganickej chémie SAV,  
Trenčianskej univerzity A. Dubčeka a RONA, a.s.,  
Študentská 2, Trenčín, 911 50, Slovenská Republika*

Pre sklá so zložením  $15M_2O \cdot 10CaO \cdot xZrO_2 \cdot (75-x)SiO_2$  ( $M = Na$  pre NCZ sklá a  $M = K$  pre KCZ sklá;  $x = 1, 3, 5, a 7$ ) sa zmerali teplotné závislosti viskozity a hustoty, teplotná rozťažnosť, teplota skleneného prechodu, index lomu, a chemická odolnosť voči vode. V práci sa v súvislosti so zmenami štruktúry kremičitanovej siete diskutuje efekt ekvimolárnej substitúcie  $SiO_2/ZrO_2$  na merané fyzikálne vlastnosti. Potvrdilo sa, že zvyšujúci obsah  $ZrO_2$  výrazne zvyšuje chemickú odolnosť voči vode v oboch skúmaných sériách zložení skiel. Substitúcia  $SiO_2/ZrO_2$  spevňuje kremičitanovú sieť a zvyšuje preto teplotu skleneného prechodu a viskozitu, pričom súčasne znižuje koeficient teplotnej rozťažnosti. Ďalej sa zisťovalo, že molárna refrakcia je lineárnou funkciou obsahu  $ZrO_2$  vyjadreného v molových %. Emranica tejto závislosti je rovnaká v oboch skúmaných sériách zložení skiel, pričom vyšší úsek pozorovaný pre draselné sklá dobre korešponduje s vyššou polarizovateľnosťou draselného kationu v porovnaní so sodným kationom. V porovnaní s NCZ sklami majú KCZ sklá vyššie hodnoty viskozity a aktivačnej energie viskózneho toku, pričom lineárna závislosť aktivačnej energie viskózneho toku od obsahu  $ZrO_2$  je pre KCZ sklá strmšia.

# INFLUENCE OF REFERENCE ELECTRODE POWDER CHARACTERISTICS ON PERFORMANCE OF ZIRCONIA OXYGEN SENSORS

HÜSEYİN Ş. SOYKAN, YILMAZ KARAKAŞ\*

*Department of Metallurgy and Materials Engineering, Kocaeli University, 41040, Izmit, Turkey*

*\*Department of Metallurgy and Materials Engineering, Sakarya University, 54187, Adapazari, Turkey*

E-mail: hsoykan@erdemir.com.tr

Submitted May 31, 2005; accepted December 10, 2005

**Keywords:** Oxygen sensors, Reference electrode powders, Coprecipitation, Molten steel

*Reference electrode powder is an important part, which affect performance of zirconia oxygen sensors. The new reference electrode powders with variations in terms of  $\text{Cr}_2\text{O}_3\text{-Fe}_2\text{O}_3$  composition and chromium-oxide ratio have been produced by chemical coprecipitation method. The microstructural characterization of the reference electrode powders were conducted using scanning electron microscopy (SEM). Performance of the reference electrode powders was tested in oxygen activity measurements at molten steel under industrial steelmaking practice. The powders produced by the oxide coprecipitation work very well in terms of the EMF reproducibility and of the response time for the low oxygen content measurements. The chemically produced  $\text{Cr}_2\text{O}_3\text{-Fe}_2\text{O}_3$  powder mixtures very well attach to the Cr particles. This fact gives good electromotive force (EMF) reproducibility with accurate Al response. Elevated  $\text{Fe}_2\text{O}_3$  content of the oxide powder reduces the EMF overshoot and improves the measurement accuracy. More positive EMF measurements, lower Al predictions than the chemical analysis and reduced probe accuracy at higher Al contents are obtained with decreasing the oxide content of the reference powder.*

## INTRODUCTION

The control of oxygen content in molten steel is one of the critical importance in steelmaking from stand point of proper deoxidation, steel cleanliness, good recovery of alloying additives and final product quality. In order to control the oxygen content in the steel, the knowledge of the oxygen concentrations or activities at various stages in the process is required. This can be directly achieved by using an oxygen sensor [1-3]. The oxygen sensor is an indispensable tool for process control in steelmaking, such as the estimation of carbon content at blow end of basic oxygen furnaces, or improvement in aluminum control in the secondary refinement [4,5]. The oxygen sensors are today regularly used in the areas of converter steelmaking, ladle treatment and casting of the steel [6].

The oxygen sensor is a simple oxygen concentration cell, which is mainly composed of a solid electrolyte and a reference electrode. Magnesia-partially stabilized zirconia (Mg-PSZ) having ionic conductivity at higher temperatures is widely used as the solid electrolyte in the form of a closed end tube [7-9]. The oxygen reference electrode in the cell is powder mixture of metal and its oxide. The sole purpose of the reference material is to ensure that the activity on one side of the

solid electrolyte remains constant. For this purpose, a metal-metal oxide system is used which, at a known temperature, gives a fixed oxygen activity. A powder mixture of Cr-Cr<sub>2</sub>O<sub>3</sub> is the best known reference material for the oxygen sensors due to its oxygen activity very close to the that of the molten steel [10,11].

In industrial applications, the accuracy and the reproducibility of the oxygen measurements and success rates are satisfactory, in general [12]. However, the oxygen sensor is still capable of further improvements from the viewpoints of the solid electrolyte and the reference electrode. The response time of the sensor in oxygen content less than 10 ppm, as observed after deoxidation processes, needs to be improved. Since the EMF of the sensor takes a longer time to stabilize in such a low range, immersion process of the sensor into molten steel takes longer time until the oxygen cell reaches its equilibrium state. Mochizuki and co-workers [13] reported that the zirconia tube with a thinner tip end thickness and less amount of Cr-Cr<sub>2</sub>O<sub>3</sub> powder reduces the response time of the cell. Worrell and co-workers [14] developed an extended-life oxygen sensor for the iron and the steel melts using isostatic fabrication technique. On the other hand, Dimitrov and co-workers [15] studied new oxygen reference materials, which exhibit lower oxygen partial pressures than that of Cr-Cr<sub>2</sub>O<sub>3</sub> to reduce gradient of the oxygen potential for semi-killed or fully killed steels.

*Authors are now with "Eregli Iron and Steel Works Co., Kdz. Eregli, Zonguldak, Turkey".*

The aim of the present investigation is to understand the influence of new reference electrode powders on the performance of the commercial sensors in terms of EMF reproducibility, the response time and the accuracy in soluble Al predictions. The study is concerned with chemically produced powders and their characteristics including variations in the oxide composition and the metal/metal oxide ratio.

## EXPERIMENTAL

The reference electrode powders given in table 1 were produced by chemically oxide coprecipitation method [16]. The powders varied in terms of  $\text{Cr}_2\text{O}_3\text{-Fe}_2\text{O}_3$  composition, and chromium-oxide ratio. In order to prepare the oxide part of the powders, raw materials used were reagent grade  $\text{Cr}(\text{NO}_3)_3 \cdot 9\text{H}_2\text{O}$  and  $\text{Fe}(\text{NO}_3)_3 \cdot 9\text{H}_2\text{O}$ . The nitrate salts were dissolved in distilled water individually, then mixed corresponding to the compositions and stirred simultaneously. The mixture was hydrolyzed by pouring aqueous ammonia, while pH value was maintained at 7. The precipitates were washed several times and then the required amount of hydroxide/water sediment was mixed as slurry with coarse Cr particles around  $100\ \mu\text{m}$  in size. The mixture obtained was dried at  $100^\circ\text{C}$  for 24 h and finally calcined at  $700^\circ\text{C}$  for 2 h.

The chemically produced powders around 30 mg were injected into the commercial Mg-PSZ tubes and back-filled with fine alumina powder. The oxygen cells were then mounted into modules and sand-filled by a domestic supplier. Figure 1 shows structure of the test probes. The main elements of the cell (figure 1a) are a Mg-PSZ solid electrolyte (A), a chemically produced reference electrode powder (B) and a Mo lead wire (C), as shown on SEM micrograph (figure 1b). The oxygen sensors were finally dipped into the molten steel, together with the commercial probes containing standard powders (CP) and samples for chemical analysis (Lab). The industrial trials were repeatedly conducted in low oxygen content on a degasser of secondary metallurgy under industrial steelmaking practice. Each oxygen sensor was applied for one quick EMF reading only. The performance of the reference powders was summarized in terms of mean difference (X), standard deviation (S) and response time, according to number of the test probes (N).

Table 1. The reference powders produced by oxide coprecipitation method.

Reference powder	Composition (wt.%)	Chromium/oxide ratio (%)
RP15a	85 $\text{Cr}_2\text{O}_3$ /15 $\text{Fe}_2\text{O}_3$	90/10
RP15b	85 $\text{Cr}_2\text{O}_3$ /15 $\text{Fe}_2\text{O}_3$	95/5
RP25a	75 $\text{Cr}_2\text{O}_3$ /25 $\text{Fe}_2\text{O}_3$	90/10
RP25b	75 $\text{Cr}_2\text{O}_3$ /25 $\text{Fe}_2\text{O}_3$	95/5

The oxygen sensor structure and the powder morphology after the calcination and the immersion to the molten steel were examined using JEOL JSM 5400 SEM.

## RESULTS AND DISCUSSION

Examination of the coprecipitated powders by SEM revealed that the powder particles were very fine and homogeneous in size. Figure 2 shows typical SEM image of the reference powder. The fine oxide powders adhere very well on the coarse Cr particles (figure 2a). In a higher magnification (figure 2b), it is clear that the particle size are generally less than  $2\ \mu\text{m}$  in size. Thus, the coprecipitation method produces very fine spherical particles of  $\text{Cr}_2\text{O}_3\text{-Fe}_2\text{O}_3$  having large surface area for ionic bonding between chromium and oxide mixture. Due to smaller particles and hence, higher surface area for reaction, production of the oxides by the coprecipi-

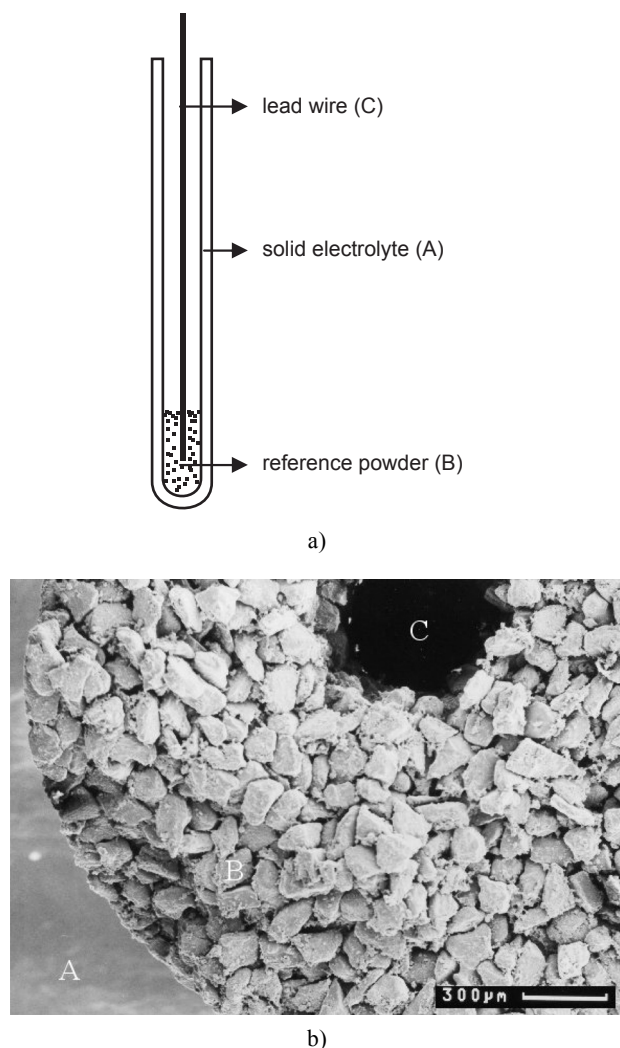


Figure 1. Structure of the test sensors: (a) schematic; (b) cross-section.

tation method might give higher EMF reproducibility and faster response times during the oxygen activity measurements in the molten steel.

The immersion tests were conducted using the oxygen sensors with the chemically produced powders having two different compositions for the investigation of the influence on the sensor performance. The sensor parameters such as temperature ( $T$ ), EMF and oxygen

concentration of the steel bath ( $a_o$ ) were measured during the immersion tests and several results obtained are given in table 2. In general, the oxygen concentration of the steel bath was lower than 10 ppm, which could introduce errors in the measurements due to the polarization effects [17].

In addition, the probe performance was tested in term of Al content predictions. In the production of Al-killed steel indicating low oxygen content, close control of the aluminum content in the molten steel is required to obtain the desired grain size of the final product [18]. The results are shown in figure 3. The coprecipitated powder RP15a brings reproducible values, while the mean difference and the standard deviation in predicted Al contents were 0.0018 and 0.0041, respectively (figure 3a). Reproducible results were obtained also with probes containing the RP25a powder (figure 3b) and CP powders (figure 3c), which were tested as a reference.

The chemically produced powders have good performance against aluminum content obtained by the chemical analysis. However, examination of the EMF traces indicates that RP25a composition tends to give a slightly flatter trace. According to the trial results, it has been found that increasing  $Fe_2O_3$  content in the reference oxide system reduces EMF overshoot and improves the trace quality. The RP25a powder exhibited a small overshoot of about 2 mV, while the overshoot was around 6 mV for RP15a powder.

The response time traces for RP15a, RP25a and CP powders are shown in figure 4. The chemically produced powders gave the response times very close to each other and to the commercial ones. The reproducibility in the response times is very consistent for all chemically produced powders. The thermal equilibrium time was below 5 seconds. These results ensure that the new reference powders are feasible with the stable EMF readings for the industrial applications.

From the literature, it is believed that 10% oxide content in the reference electrode powder gives a close relationship to the chemical analysis results [15]. In this study, the oxygen probes were tested with the chemical production powders having different Cr/oxide ratio such as 90/10 (RP15b) and 95/5 (RP25b) proportions, in weight. Figure 5 shows the results of the Al predictions. The results indicated that the EMF measurements became more positive and the Al predictions were lower than those from the chemical analysis with lower oxide content in the reference powder mixture. However, the EMF reproducibility increased, presumably due to more repeatable oxide content within each individual probe. On the other hand, the Al-mV scale became more compressed giving reduced probe accuracy at higher Al contents, when decreasing the oxide content of the reference powder.

Table 2. The oxygen sensor parameters measured in the performance tests.

Trial	Powder	$T$ (°C)	EMF (mV)	$a_o$ (ppm)
1	RP15a	1566	-120	5.02
	RP25a	1562	-122	4.75
	CP	1570	-126	4.82
2	RP15a	1591	-109	6.95
	RP25a	1591	-111	6.77
	CP	1592	-109	7.00
3	RP15a	1580	-159	3.25
	RP25a	1580	-157	3.34
	CP	1582	-156	3.40

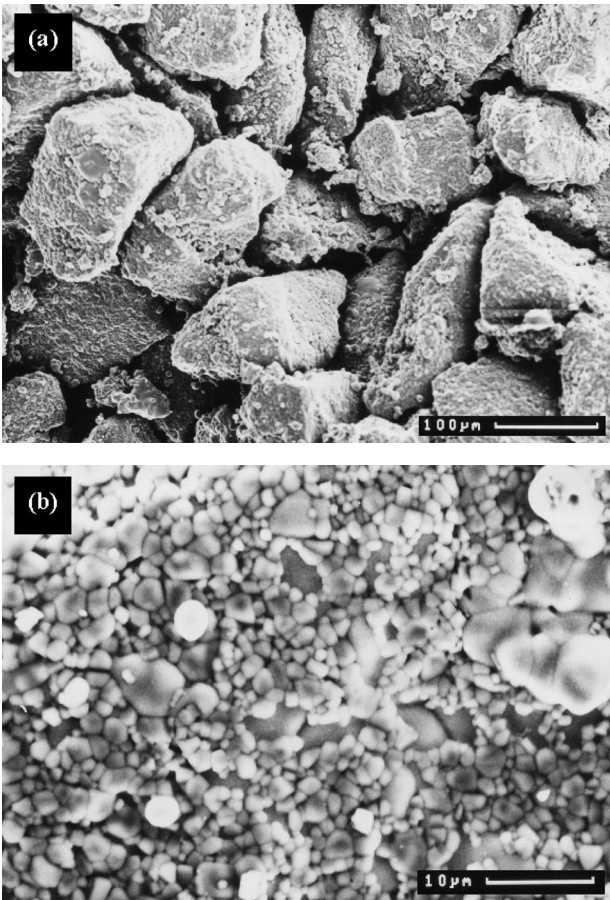


Figure 2. SEM micrographs of RP15a powder: (a) low magnification; (b) high magnification.

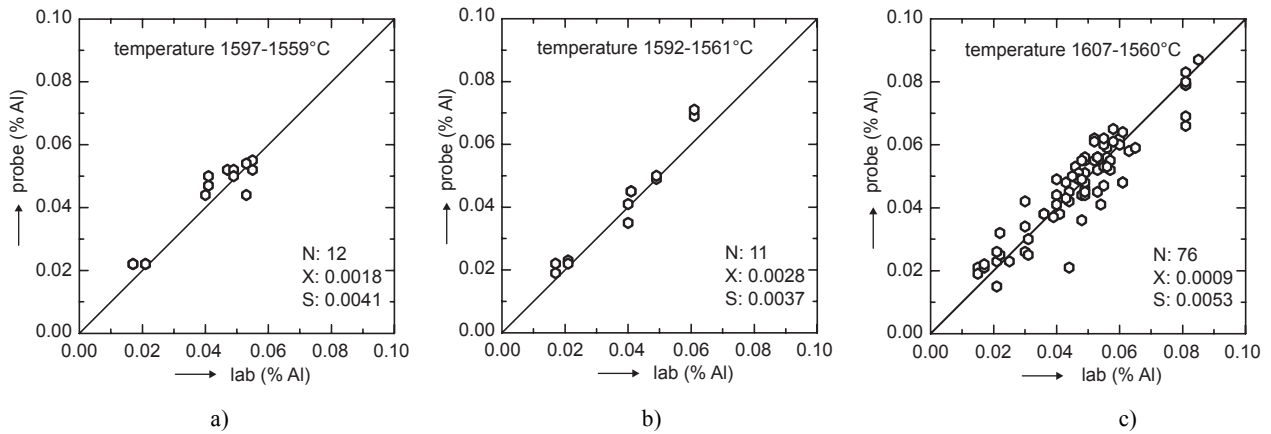


Figure 3. The performance of the reference powders used in the measurements of the low oxygen content: (a) RP15a; (b) RP25a; (c) CP.

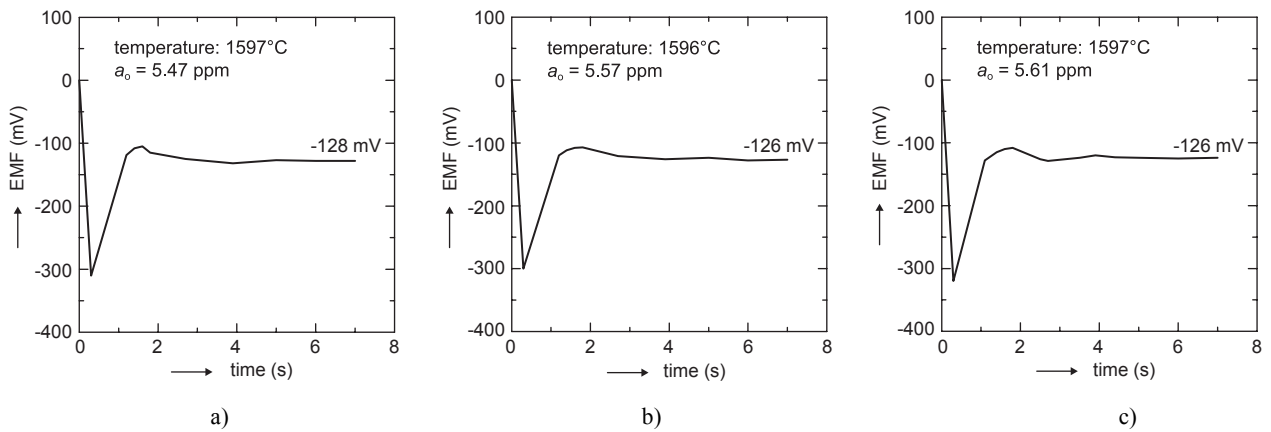


Figure 4. The response time traces of the reference powders: (a) RP15a; (b) RP25a; (c) CP.

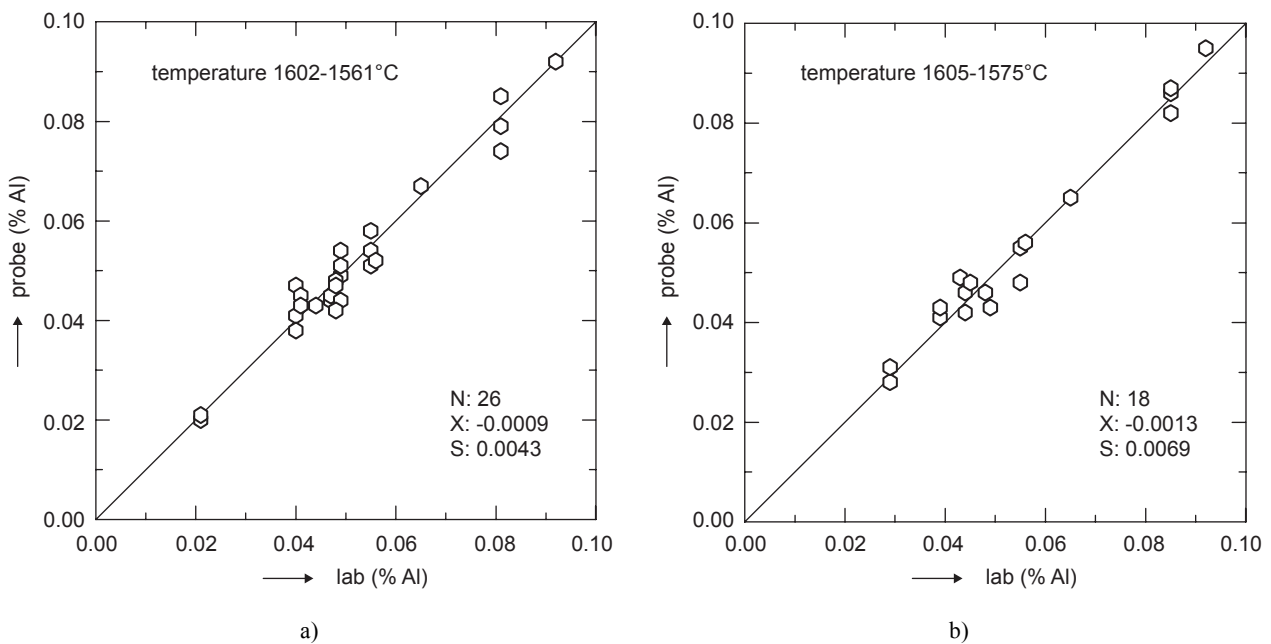


Figure 5. Influence of the chromium-oxide ratio of the reference powders on the sensor performance: (a) RP15b; (b) RP25b.

The coprecipitated powders were examined using SEM after the immersion tests. Figure 6 shows typical SEM micrograph of the probe cross-section for RP25a powder. It is obvious that the oxide powder was partially sintered. Most of the particles in the reference powder remains separated, which is very important advantage for the chemically produced powders in the industrial applications. As observed in the industrial trials, tight contact between the solid electrolyte and the reference powder during measurements of the oxygen concentration ensures a stable reference potential, rapid electrochemical equilibrium and short response times [14].

### CONCLUSION

Influence of the chemically coprecipitated reference powders on the performance of the oxygen sensors in the oxygen activity measurements has been investigated. The reference electrode powders produced by the oxide coprecipitation perform very well in terms of the EMF reproducibility and the response time for the low oxygen content measurements in the molten steel under industrial scale. The chemically produced  $\text{Cr}_2\text{O}_3\text{-Fe}_2\text{O}_3$  powders very well adhere to the Cr particles. This fact gives good EMF reproducibility with a good Al relationship. An increase in  $\text{Fe}_2\text{O}_3$  content of the oxide powder reduces the EMF overshoot and improves the trace quality. More positive EMF measurements, lower Al predictions than the chemical analysis and reduced probe accuracy at higher Al contents are obtained with decreasing the oxide content of the reference powder. In spite of the bath temperature in the molten steel, over  $1600^\circ\text{C}$ , the chemical production powders are partially sintered, which should lead to a much more attention on the method of the reference powder production used in this study.

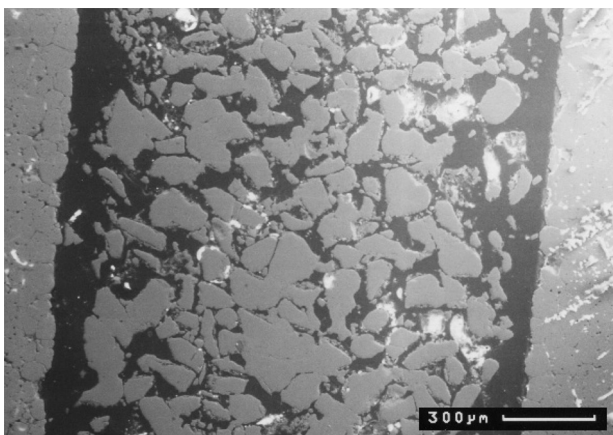


Figure 6. Typical SEM micrograph of the reference powders after immersion to the molten steel.

### References

1. Iwase M. in: *Advances in Ceramics*, Vol.24, p.871, Ed. Claussen N, Heuer A. H., The American Ceramic Society, Ohio 1988.
2. Janke D. in: *Advances in Ceramics*, Vol. 12, p.109, Ed. Claussen N, Heuer A. H., The American Ceramic Society, Ohio 1983.
3. Goto K. S., Pluschkell W., in: *Physics of Electrolytes*, Vol. 2, p.540, Ed. Hladik J., Academic Press, London 1972.
4. Janke D, in: *Int. Conf. on Clean Steel*, p.202, The Metals Society, London 1983.
5. Goto K. S., Susa M., in: *Chemical Sensor Technology*, Vol. 1, p.109, Ed. Seiyama T., Kodansha Ltd. & Elsevier, Tokyo 1988.
6. Nagata K, Goto K. S.: *Mat.Sci.&Eng. A 146*, 63 (1991).
7. Liu, M., Joshi A.V., in: *Engineered Materials Handbook*, Vol. 4, p.1132, Ed. Schneider S.J., ASM International, Ohio 1991.
8. Badwal S. P. S.: *Solid State Ion.* 52, 23 (1992).
9. Göpel W., Hesse J., Zemel, J. N.: *Sensors: A Comprehensive Survey*, VCH, Weinheim 1989.
10. Fray D.: *Chem. & Ind.* 7, 445 (1992).
11. Weyl A., Tu S. W., Janke D.: *Steel Research* 65, 167 (1994).
12. Janke D.: *Solid State Ion.* 40/41, 764 (1990).
13. Mochizuki M., Matsuoka M., Fujiwara R.: *Solid State Ion.* 40/41, 746 (1990).
14. Worrell W. L., Liu Q.: *Solid State Ion.* 40/41, 761 (1990).
15. Dimitrov S., Ranganathan S., Weyl A., Janke D.: *Steel Research* 64, 63 (1993).
16. Soykan H. Ş., Karakaş Y.: Serem Inc., Report No. SER-2001.32, Istanbul 2001.
17. Iwase M., McLean A., in: 6<sup>th</sup> Int. Iron and Steel Congress, p.521, ISIJ, Nagoya 1990.
18. Turkdogan E. T., Fruehan R. J.: *Can. Metal. Quar.* 11, 371 (1972).

### VLIV CHARAKTERISTIK PRAŠKU REFERENČNÍ ELEKTRODY NA FUNKČNOST ZIRKONIČITÝCH KYSLÍKOVÝCH SOND

HÜSEYİN Ş. SOYKAN, YILMAZ KARAKAŞ\*

Department of Metallurgy and Materials Engineering,  
Kocaeli University, 41040, Izmit, Turkey

\*Department of Metallurgy and Materials Engineering,  
Sakarya University, 54187, Adapazari, Turkey

Prášek referenční elektrody je důležitou částí, která ovlivňuje funkčnost zirkoničitých kyslíkových sond. Nové referenční prášky s různým obsahem směsi  $\text{Cr}_2\text{O}_3\text{-Fe}_2\text{O}_3$  a poměrem kov-oxid byly připraveny chemickou cestou spolusrážením. Mikrostrukturní analýza prášků byla provedena skenovací elektronovou mikroskopií. Funkčnost prášků byla testována měřením aktivity kyslíku v roztavených ocelích v ocelářské praxi. Prášky připravené srážením oxidů mají velmi dobrou EMF reprodukovatelnost a čas odezvy při měření nízkých koncentrací kyslíku. Směsné prášky  $\text{Cr}_2\text{O}_3\text{-Fe}_2\text{O}_3$  velmi dobře přilnou k Cr částicím, což dává dobrou reprodukovatelnost odezvy a správnost stanoveného obsahu Al. Zvýšený obsah  $\text{Fe}_2\text{O}_3$  redukuje EMF překmitnutí a zvyšuje přesnost měření. Nižší obsah oxidu v referenčním prášku přináší nižší stanovené obsahy hliníku v oceli ve srovnání s chemickou analýzou a snižuje správnost měření při vyšších obsahích Al.

# DEVELOPMENT OF LOW COST GLASS-CERAMIC BASED ON BLAST FURNACE SLAG AND GRANITE ROCK

SAAD MOGHAZY SALMAN, HUSSEIN DARWISH

*Glass Research Dept., National Research Centre, El-Beheos St., Dokki, Cairo, Egypt*

E-mail: hussein25@yahoo.com

Submitted September 1, 2005; accepted December 30, 2005

**Keywords:** Slag, Granite, Glass, Glass-ceramics, Thermal expansion, Chemical durability

*The development of low cost glass-ceramic based on various contents of Egyptian blast furnace slag and granite rock has been investigated. The effect of granite / slag replacements on the crystallization characteristics of the glasses and the resulting microstructure, are traced by differential thermal analysis (DTA), x-ray diffraction analysis (XRD) and scanning electron microscopy (SEM). Varieties of melilite phase of gehlenite type, wollastonite solid solution and anorthitic plagioclase phases were mostly formed depending on the granite/slag ratios in the glasses. The types of the crystallized phases formed are discussed in relation to the compositional variation of the glasses and thermal treatment applied. SEM micrographs showed that granite/slag replacement promoted a uniform volume crystallization of fine-grained interlocked microstructure, which is achieved by increasing the granite content in the glasses. The addition of LiF as nucleation catalyst enhanced the crystallization characteristics of the glasses. The increase of granite at the expense of slag in the glasses led to improve both the thermal expansion characteristics and the chemical durability of the materials investigated.*

## INTRODUCTION

In general, glass-ceramics may be defined as polycrystalline solids produced by controlled crystallization of glasses [1]. Slag-based glass-ceramic materials are different in resulting properties than those prepared from elemental technical grade oxide powders. The primary difference is that slag-based glass-ceramic materials are multicomponent systems to start with, whereas glass-ceramics developed from elemental powders are made multicomponent by choice for the purpose of tailoring resulting properties.

Slag is an industrial solid waste generated in the process of iron ore reduction in blast furnace which represent one of the many types of wastes resulting from the industrial metallurgical processes. The major amount of slag produced in Egypt at a rate of 300 000 tons/year is being used as a raw material for the cement industry and in road pavement. The rest is directly discharged in landfills, which consequently can cause environmental problems. So reducing the environmental impact of slag, scrap and dust resulting from iron and steel product will give its product further important benefit and other significant potential for cost savings profit if reintroduced into the industrial process through well planned programs [2]. Knowledge of the atomic scale structure of slags is essentially required in order to discuss various properties of slags [3-4].

Granite is widely distributed in Egypt and occurs in large deposits at Aswan, in the Eastern desert, the Sinai and to a smaller extent in the Western desert. In the

Aswan region the granite deposits consists of both the monumental red and monumental black varieties. The term granite applies to any holocrystalline quartz-bearing plutonic rock, in which quartz makes up 10 to 50 % of the felsic components, the alkali feldspar/total feldspar ratio is between 65 to 90 %, and the modal concentration of mafic minerals is less than 10 % (hornblende, biotite). Grain size of the minerals components generally range from 1 millimeter to many centimeters [5].

Due to the high cost of some of the chemical ingredients e.g.  $\text{Li}_2\text{O}$ ,  $\text{B}_2\text{O}_3$ ,  $\text{Al}_2\text{O}_3$  etc., and the high melting temperatures or special melting conditions, glass-ceramics are relatively expensive materials. The motivation for developing glass-ceramics from metallurgical slags together with granite rock as a raw material instead of using technical grade powders stems from the fact that cheaper production costs would allow higher profits in practical applications such as wall claddings and floor tiles [6].

Glass-ceramic materials have a number of outstanding characteristics in comparison with the traditional ceramics and glasses, which determine their application in advanced technology as well as in electronics and medicine [7].

The aim of the present work is to develop some types of glasses and glass-ceramics based on blast furnace slag - granite rock mixtures and to study their crystallization behaviour, microstructure, and phase relation as well as the thermal expansion and chemical durability of the materials.

## EXPERIMENTAL

Local granulated blast furnace slag of the Egyptian Iron and Steel Company and Aswan granite, at Upper Egypt were the main starting materials used in this study. The chemical compositions of slag and granite were chemically analyzed [8]. After drying and pulverizing steps, the slag had the following chemical composition (in wt.%): 34.15 % SiO<sub>2</sub>, 46.13 % CaO, 11.33 % Al<sub>2</sub>O<sub>3</sub>, 2.28 % MgO, 1.10 % MnO<sub>2</sub>, 1.65 % Fe<sub>2</sub>O<sub>3</sub>, 0.84 % FeO, 0.88 % Na<sub>2</sub>O, 0.11 % K<sub>2</sub>O, 0.09 % P<sub>2</sub>O<sub>5</sub>, 1.47 % S.

Aswan granite rock had the following chemical composition (in wt.%): 69.91 % SiO<sub>2</sub>, 1.91 % CaO, 14.66 % Al<sub>2</sub>O<sub>3</sub>, 1.40 % MgO, 1.6 % FeO, 0.6 % Fe<sub>2</sub>O<sub>3</sub>, 3.06 % Na<sub>2</sub>O, 6.08 % K<sub>2</sub>O, 0.78 % TiO<sub>2</sub>. The amount of Fe<sup>2+</sup>/Fe<sup>3+</sup> was determined by calorimetric analysis [9]. LiF was added in amount of 3 g over 100 g glass oxide constitutions of the batch compositions as a nucleating agent. Details of the batch compositions of the prepared glasses are given in table 1.

The weighed batches were thoroughly mixed and were melted in Pt-2%Rh crucible in an electric heating furnace, with SiC heating elements, at 1400-1450°C for 3 hours duration with occasional stirring to ensure homogeneity. The homogeneous bubble-free melts were cast into rectangular rods (0.5 × 0.5 cm cross section and 1.5 cm length), and as buttons, which were then well annealed at 600°C in a muffle furnace to minimize the strain of the glasses.

The thermal behaviour of the finely powdered (45-75 μm) glass samples was examined using a SETARAM Labsys TMTG-DSC16. The powdered glass was heated in Pt-holder against another Pt-holder containing Al<sub>2</sub>O<sub>3</sub> as a reference material. A uniform heating rate of 10°C/min was adopted. Data were recorded using a computer-driven data acquisition system. The results obtained were used as a guide for determining

the required heat-treatment temperatures applied to induce crystallization of the glasses.

The progress of crystallization in the glasses was followed by using double stage heat-treatment regimes. The glasses were first heated according to the DTA results at the endothermic peak temperature for 5 h, which was followed by another thermal treatment at the exothermic peak temperature for 10 h.

Crystal phases were identified by the x-ray diffraction (XRD) analysis using a Philips type diffractometer (P.W. 1730) with Ni-filtered Cu-Kα radiation. The crystallization characteristics and internal microstructures of the resultant materials were examined by using scanning electron microscopy (SEM), where representative electron micrographs were obtained using Jeol, JXA-840 A Electron Probe Microanalyzer.

The thermal expansion characteristics of the investigated glasses and glass-ceramics were carried out on (0.5 × 0.5 cm cross section and 1.5 cm length) rods using a Linseis L76/1250 automatic recording multiplier dilatometer with a heating rate of 5°C/min. The coefficients of thermal expansion (α-values) of the investigated glasses were measured from room temperature up to 300°C while the glass-ceramics were measured up to 600°C. The linear thermal expansion coefficient (α) was automatically calculated using the general equation:

$$\alpha = (\Delta L/L) \times (1/\Delta T) \quad (1)$$

where (ΔL) is the increase in length, (ΔT) is the temperature interval over which the sample is heated and (L) is the original length of the specimen.

The chemical durability of the glass-ceramics in acidic medium was determined. The samples were crushed in an agate mortar and then sieved using BS sieves to obtain the fraction with granulation range 0.32 mm 0.63 mm. The grains were washed several times with ether, dried at 110°C for 2 hrs and then transferred to weighing bottles and cooled in a desiccator.

Table 1. Composition of the glasses (wt.%).

oxides	G <sub>1</sub>		G <sub>2</sub>		G <sub>3</sub>		G <sub>4</sub>	
	slag 80	granite 20	slag 60	granite 40	slag 50	granite 50	slag 40	granite 60
SiO <sub>2</sub>	41.3		48.45		52.04		55.61	
CaO	37.28		28.44		24.02		19.60	
Al <sub>2</sub> O <sub>3</sub>	11.99		12.66		12.99		13.33	
Fe <sub>2</sub> O <sub>3</sub>	1.44		1.23		1.13		1.02	
FeO	1.00		1.15		1.22		1.30	
MgO	2.1		1.93		1.84		1.75	
MnO <sub>2</sub>	0.86		0.65		0.54		0.43	
Na <sub>2</sub> O	1.32		1.75		1.98		2.19	
K <sub>2</sub> O	1.31		2.50		3.10		3.69	
P <sub>2</sub> O <sub>5</sub>	0.07		0.05		0.04		0.03	
S	1.17		0.88		0.71		0.58	
TiO <sub>2</sub>	0.16		0.31		0.39		0.47	
granite/slag ratio	0.25		0.67		1.0		1.5	

One gram of the sample grains was accurately weighed in a  $G_4$ -sintered glass crucible and then placed in a 400 ml polyethylene beaker. The sample was subjected to the static action of 200 ml of 0.1N HCl for 1, 3 and 7 hrs at 95°C using a contact thermometer water bath. The polyethylene beaker with its content was covered by a polyethylene cover to reduce evaporation. The volume of the leaching solution was made large enough relative to the weight of the sample grains in order to avoid formation of saturated solutions, which might prevent further leaching of grains. The reproducibility of the results for representative duplicate samples was better than 5%. The percentage weight loss was taken as a measure of the relative magnitude of the leaching rate.

## RESULTS

The DTA data of the glasses (figure 1) showed endothermic peaks in the 730-750°C temperature range. These endothermic peaks are to be attributed to the nucleation processes, at which the atoms begin to arrange themselves in preliminary structural elements subsequent to crystallization. Two exothermic peaks are detected in each glass, indicating crystallization reaction in the glasses. However, the heat-treatment was carried out using the higher exothermic peak temperature to attain the most stable phases in the crystalline glasses ( $G_1$ - $G_4$ ).

The progress of crystallization in the glasses, the type and proportions of the crystalline phases formed were markedly dependent on the variation of the granite/slag ratios in the glass and the effect of thermal treatment as well as the role of the nucleating agent added.

The DTA data (figure 1) revealed that the endothermic dips as well as the onset of crystallization were shifted to higher temperature values with increasing the granite contents in the glass at the expense of the slag.

SEM micrographs of fracture surfaces of selected crystalline samples  $C_1$  and  $C_4$  demonstrate the effect of increasing granite content at the expense of slag on the microstructure formed. Granite promoted volume crystallization of the glass to form holocrystalline mass without deformation by thermal treatment. For example SEM micrograph of  $C_1$  (with 20% granite) clearly showed that numerous aggregates of crystals were formed (figure 2). However, at 60% granite,  $C_4$ , fine interlocked growths were formed giving rise to network-like microstructure (figure 3).

The phases developed in glass-ceramics ( $C_1$ - $C_4$ ) over the investigated 980-1030°C temperature range as indicated by the X-ray diffraction analysis (figure 4) were melilite phase of gehlenite type, anorthitic plagioclase phase and wollastonite solid solution.

At low granite / slag ratio (0.25) i.e.,  $G_1$  heated at 730°C/5 h - 980°C/10 h led to the formation of melilite of gehlenite- $Ca_2Al_2SiO_7$  type (lines 5.07, 3.72, 3.47, 2.86, 2.40..., PDF No. 20-199) [10] as well as wollastonite ss phase (pattern I). The XRD analysis clearly indicated the diffraction lines of the solid solution formed i.e. (7.62, 3.80, 3.49, 3.28, 3.01, 2.95...) were identical, with a slight shift, to those of wollastonite- $CaSiO_3$  (PDF No. 29-372) [10].

The addition of LiF in glass  $G_1$  resulted in enhanced crystallization of melilite of gehlenite type and wollastonite ss phases as indicated from the increase of the intensity of the d-spacing lines characteristics of these phases as indicated in the x-ray diffraction pattern of the glass-ceramic  $C_1$  (figure 4, pattern II).

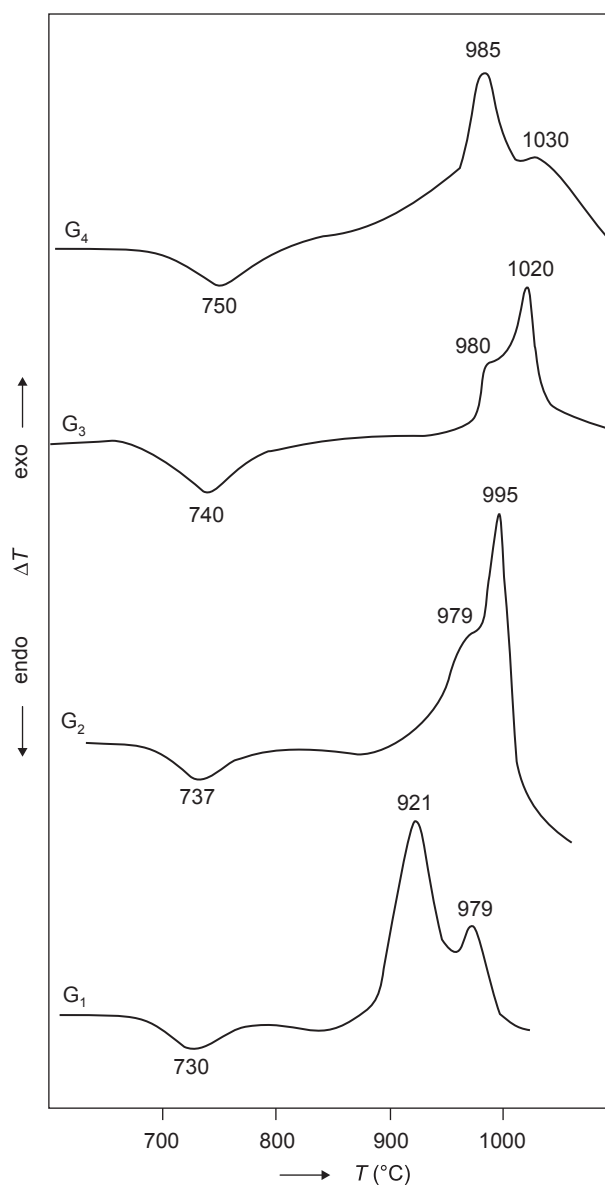


Figure 1. DTA data of the studied glasses.

On increasing the granite/slag ratios (up to 0.67, 1.0 and 1.5) i.e.,  $G_2$ ,  $G_3$  and  $G_4$  respectively, the XRD analysis (figure 4, patterns III-V) revealed that the thermal treatment of these glasses at 735°C/5 h - 995°C/10 h, 740°C/5 h - 1020°C/10 h, and 750°C/5 h - 1030°C/10 h, respectively, led to the formation of plagioclase phase of anorthite– $\text{CaAl}_2\text{Si}_2\text{O}_8$  type (lines 3.71, 3.28, 3.21, 3.12, 2.51, 1.82..., PDF No. 12-301)[10] (major) and wollastonite ss phase. The addition of LiF to glass  $G_4$ , as nucleating agent, led to the formation of the same phases with the increase of the intensity of their characteristics d-spacing lines as indicated from XRD analysis (figure 4, pattern VI).

The thermal expansion data of the glasses and their respective crystalline solids as a function of the granite/slag ratios are shown in figures 5 and 6.

Figure 5 and table 2 revealed that the thermal expansion coefficients of the glasses as well as their  $T_g$  and  $T_s$  values are greatly dependent upon the base glass composition. With successive increase of granite contents at the expense of slag in the glasses, the expansion coefficients decreased (figure 5). While, both the dilato-

metric  $T_g$  and softening  $T_s$  temperatures of the glasses were increased. Lithium fluoride has a great influence on increasing the expansion coefficients of the studied glasses and decreasing their dilatometric  $T_g$  and softening  $T_s$  temperatures (table 2).

The expansion coefficient values of the glass-ceramics are decreased by additions of granite at the expense of slag ( $C_1$ - $C_4$ , figure 6). The addition of LiF as nucleating agent led to increase of the expansion coefficient of glass-ceramics, table 2.

Adding the granite at the expense of slag led to improve chemical durability of the glass-ceramics ( $C_1$ - $C_4$ ) i.e., increasing the granite content in the glasses led to a remarkable decrease in the leachability of the corresponding glass-ceramics. Applying the long-term action of acid, figure (7) indicated that the glass-ceramic with granite/slag ratios > unity, i.e. 1.5,  $C_4$  was the most durable sample, while that with the lowest granite/ slag ratio i.e. 0.25,  $C_1$  was the least durable one. Table 2 revealed that the chemical durability glass-ceramics  $C_1$  and  $C_4$  was decreased by addition of the LiF.

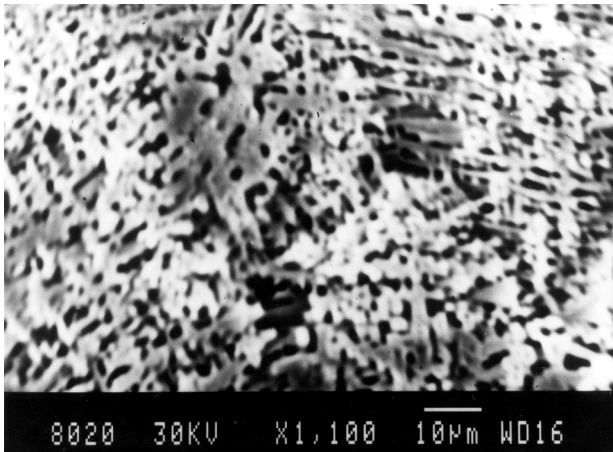


Figure 2. SEM micrograph of fracture surface of  $C_1$  crystallized at 730°C/5h - 980°C/10h showing volume crystallization of coarse interlocked structure.

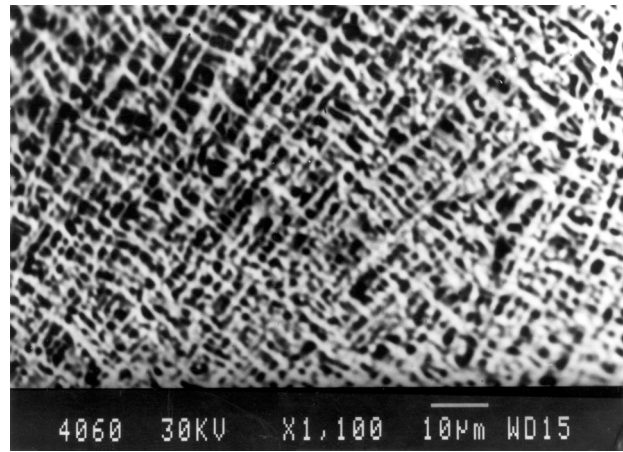


Figure 3. SEM micrograph of fracture surface of  $C_4$  crystallized at 750°C/5h - 1030°C/10h showing volume crystallization of fine interlocked structure.

Table 2. Thermal expansion coefficients and chemical durability data of the LiF-containing glasses and glass-ceramics.

sample no.	expansion coefficients $\alpha \times 10^7$ ( $^{\circ}\text{C}^{-1}$ )					$T_g$ ( $^{\circ}\text{C}$ )	$T_s$ ( $^{\circ}\text{C}$ )	weight loss (%) in 0.1N HCl at 95°C		
	25-300	25-400	25-500	25-600	25-700			1 h	3 h	7 h
$G_1$	87	90	93	94	-	659	710	-	-	-
$G_1$ +LiF	97	98	103	-	-	548	580	-	-	-
$C_1$	85	89	92	93	94	-	-	1.72	2.34	4.97
$C_1$ +LiF	93	94	94	95	96	-	-	5.46	6.74	9.56
$G_4$	75	76	77	78	-	690	727	-	-	-
$G_4$ +LiF	76	80	86	-	-	559	613	-	-	-
$C_4$	42	45	46	47	48	-	-	0.15	0.24	1.39
$C_4$ +LiF	67	69	74	80	85	-	-	3.69	4.6	5.89

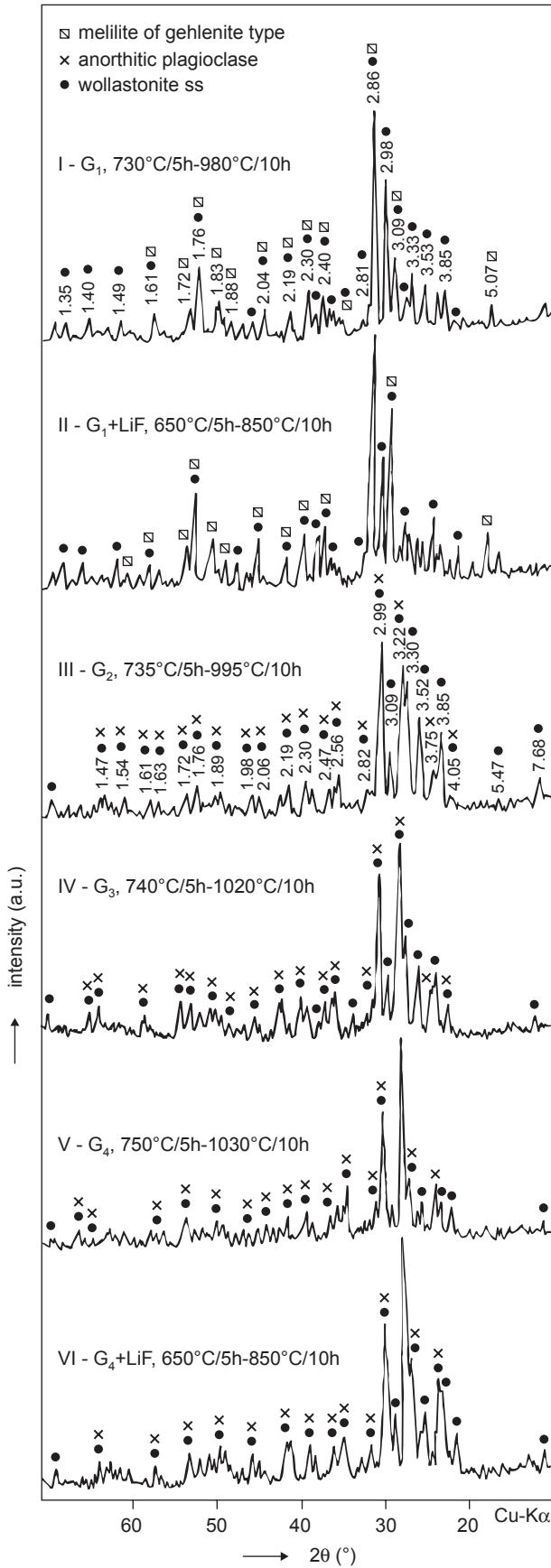


Figure 4. XRD analysis of crystallized glasses.

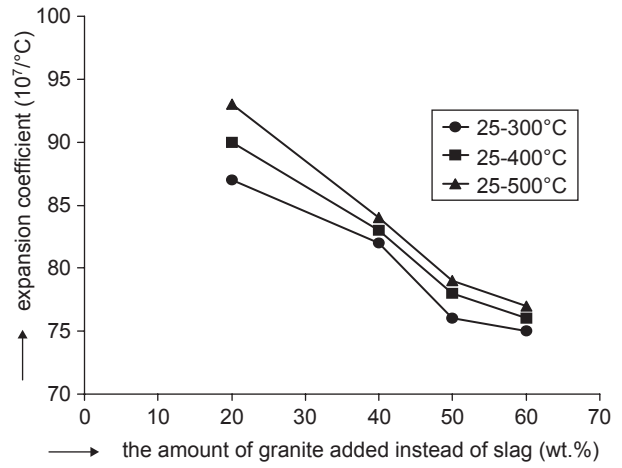


Figure 5. The thermal expansion coefficients of the glasses as a function of the amount of granite added.

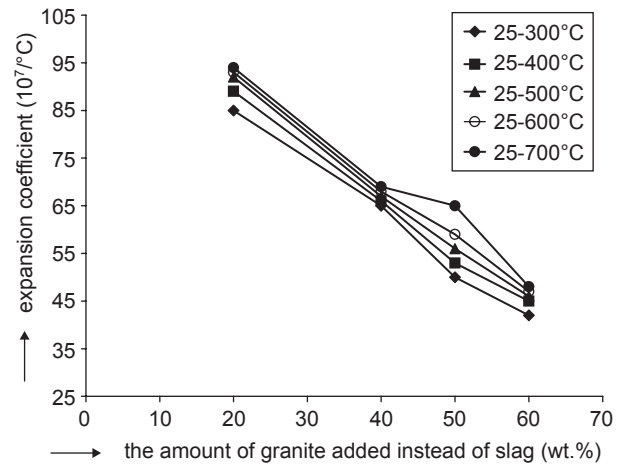


Figure 6. The thermal expansion coefficients of the glass-ceramics as a function of the amount of granite added.

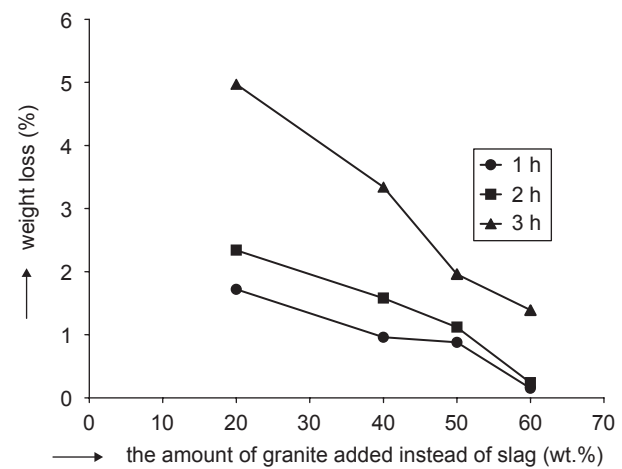


Figure 7. Measured percentage weight loss of glass-ceramic as a function of the amount of granite added.

## DISCUSSION

The blast furnace slag is highly susceptible to devitrification to the extent that no monolithic glassy phase could be obtained even through the granulation process. Any composition for a glass-ceramic requires only the ability to form a glass and control its crystallization into the favourable fine-grained microstructure [11]. Therefore, in order to obtain a stable glass from slag, it is necessary to decrease the diffusion rate throughout the slag-based glass by increasing its viscosity. This may reduce either the rate of nucleation or crystallization; or at least minimize the temperature zones of their overlapping. The addition of granite to slag is satisfying these requirements [5].

The DTA data revealed that the addition of granite in the present glasses at the expense of slag had significant effects on the temperatures at which the nucleation and crystallization start. It increases the temperature of both endothermic and exothermic peaks, i.e. more energy is needed to induce crystallization in glasses with higher content of granite. This can be attributed to the role played by  $\text{Al}^{3+}$  and  $\text{Si}^{4+}$  ions, which increased as the granite content in the glass was increased. Accordingly, in glasses with high alkaline earth silicate, the  $\text{Al}^{3+}$  ions being in four-fold coordination form ( $\text{AlO}_4$ ) tetrahedra, which enter the glass network and take part in the formation of a strong aluminium-silicon-oxygen framework [12]. The formation of such closely packed tetrahedral structural groups led to shift both the endo- and exothermic peaks towards high temperatures.

The DTA data revealed also that the sharp crystallization peaks observed at constant heating rate is indicative of the domination of bulk crystallization mechanism. These results are in consistent with the assumption developed by Ozawa [13] who reports that for a constant heating rate, a broad crystallization peak indicates surface crystallization while a sharp peak signifies a bulk crystallization.

The addition of LiF as nucleating agent led to increase the crystallization tendency of the glasses. This can be attributed to the fact that the fluorine ion, with a radius of 1.36 Å, is very close in size to the oxygen ion (radius 1.40 Å) so that a fluorine ion could replace an oxygen ion in the glass network [11]. Since the fluorine ion is monovalent, the overall replacement within the glass must be of two fluorine ions for each oxygen ion in order to ensure electrical neutrality. A general effect of the fluorine would be the replacement of the strong  $\equiv\text{Si}-\text{O}-\text{Si}\equiv$  linkages by pair of weaker  $\equiv\text{Si}-\text{F}$  linkages with the result that the glass network structure would be weakened. This led to decrease the viscosity of the glass melts and may result in the subsequent ease of migration and diffusion of different ions and ionic complexes present, therefore an increase in the rate of nucleation and crystallization could be expected.

In the light of microstructural observations, SEM revealed that the combination of crystallization at a high temperature and the progressive increase in the granite contents resulting into a finer grain size and more uniform bulk crystallization. It is clear that the microstructures were changed from numerous aggregates of crystals to fine growths of network microstructure. Strnad [14] revealed that the nucleating agents used for Slagsitall glass-ceramic include the sulphides of the heavy metals (FeS, MnS) in optimal concentrations of 0.2 to 0.4 wt.%. Agarwal et al., [15] studied the crystallization behaviour of cupola slag glass-ceramic and revealed that the heterogeneous nucleation sites for the obtained wollastonite solid solution crystals were Fe-Mn sulphides, which crystallize from dispersed immiscible droplets existing when the glass is quenched. It seemed therefore, that Fe-Mn sulphides present in glass 4 are effective as nucleating agents to induce fine grained bulk crystallization, figure 3.

## Effect of granite/slag replacements on the crystalline phases formed

The X-ray diffraction analysis revealed that the base glass  $G_1$  (with granite/slag ratio up to 0.25) crystallized into melilite phase of gehlenite type and wollastonite ss phase. The d-spacing reflections of the wollastonite solid solution formed are similar to those of wollastonite phase. No other phases could be detected. This will lead to an important conclusion that all other elements present in the melt can find place in the wollastonite or melilite of gehlenite type structure [15].

The displacement of the major characteristic d-spacing reflections of the formed wollastonite solid solution phase towards higher  $2\theta$  values may support the suggestion that wollastonite could acquire considerable amounts of  $\text{Fe}^{2+}$ ,  $\text{Mn}^{2+}$ ,  $\text{Mg}^{2+}$ ,  $\text{K}^+$ ... etc replacing  $\text{Ca}^{2+}$  and  $\text{Ti}^{4+}$  replacing  $\text{Si}^{4+}$  in its structure [15, 16].

Salama [17] found that wollastonite forms extensive series of solid solutions with  $\text{MnSiO}_3$  extending to about 75 wt. %  $\text{MnSiO}_3$  and concluded also that varieties of Ca, Mn-silicate solid solutions including Mn-wollastonite ( $\text{Ca}_{0.75}, \text{Mn}_{0.25}$ )  $\text{SiO}_3$ , bustamite [ $\text{CaMn}(\text{SiO}_3)_2$ ] and  $\beta$ -Mn-Silicate ( $\text{Mn}_{0.25}, \text{Ca}_{0.25}$ )  $\text{SiO}_3$  were mostly formed depending on the MnO/CaO ratios in the glasses. Mn-pyroxene ss forming varieties of the probable formula ( $\text{Ca}_{0.5}, \text{Mn}_{0.5}$ )  $\text{MgSi}_2\text{O}_6$  and  $\text{Ca}(\text{Mn}_{0.5}, \text{Mg}_{0.5})\text{Si}_2\text{O}_6$  in glass containing  $\text{Ca}^{2+}$ ,  $\text{Mg}^{2+}$  and  $\text{Mn}^{2+}$  ions.

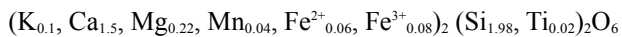
Salama and Salman [18] concluded also that in the presence of mixing of three divalent oxides (i.e.  $\text{Ca}^{2+}$ ,  $\text{Mg}^{2+}$  and  $\text{Mn}^{2+}$ ), metasilicates of these divalent cations were assumed to be formed i.e.  $\text{CaSiO}_3$ ,  $\text{MgSiO}_3$  and  $\text{MnSiO}_3$ , which go into solid solution to form a pyroxene solid solution series.

Schairer and Bown [19] showed that there is a solid solution between wollastonite and diopside in the CaO–MgO–SiO<sub>2</sub> system with a maximum 22 % of the later at eutectic.

Salman et al. [20] investigated the crystallization behaviour of Li<sub>2</sub>O–CaO–MgO–SiO<sub>2</sub> glasses. They pointed out that in Ca-containing glasses, four varieties of Ca, Mg-Silicate phases were identified depending on the CaO/MgO ratio, namely clinopyroxene ss, diopside, wollastonite ss and pure Ca-silicate-wollastonite. They showed that the Ca-Mg-silicate phase formed is a solid solution between diopside and wollastonite. The diopside component in this solid solution amounts to 49.6 %. However, Salman et al., [21] found that wollastonite - diopside solid solution phase containing up to 66 % of diopside could be formed. This Mg-rich wollastonite solid solution which disintegrates ultimately by increasing time or at high temperature of heat-treatment to wollastonite and diopside.

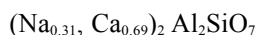
Bowen et al [22] showed that, wollastonite forms an extended series of solid solutions in the system CaSiO<sub>3</sub>–FeSiO<sub>3</sub>, wollastonite ss being obtained with up to 76 wt.% FeSiO<sub>3</sub> at high temperatures.

Therefore, the theoretical calculation of the glass compositions (G<sub>1</sub>–G<sub>4</sub>) into normative mineral molecules [23] indicated that the wollastonite solid solution developed in crystalline glass G<sub>1</sub> may had the following probable formula:



Agarwal et al., [15] revealed that the nature of shift in the X-ray peak of wollastonite phase indicates the substitution of a smaller ion for calcium causing the shrinking of lattice.

Gehlenite phase is related to a group of minerals known as melilite. The chemical formula of the melilite group is a solid solution of Al–end member gehlenite–Ca<sub>2</sub>Al<sub>2</sub>SiO<sub>7</sub> and Mg–end member akermanite–CaMgSi<sub>2</sub>O<sub>7</sub> [24]. There is no solid solution in gehlenite–wollastonite system [25]. Goldsmith [26] stated that 15 % Na<sub>2</sub>Si<sub>3</sub>O<sub>7</sub> enters into solid solution with gehlenite–Ca<sub>2</sub>Al<sub>2</sub>SiO<sub>7</sub> (with Na<sub>2</sub>O content of 3.85 %). Theoretically, [23] it is assumed therefore that the Melilite phase of gehlenite type formed in the glass-ceramic of G<sub>1</sub> has probably the following formula:

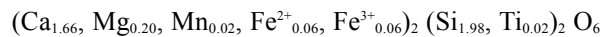


Attempts to synthesize K–melilite have been unsuccessful due to the lack of suitable accommodation in melilite structure for the large K<sup>+</sup> ion [27].

Increasing granite/slag replacements in the glasses G<sub>2</sub>–G<sub>4</sub>, anorthitic plagioclase (instead of melilite phase of gehlenite type) together with wollastonite ss phases were developed. The SiO<sub>2</sub> and Al<sub>2</sub>O<sub>3</sub> contents in these glasses increased while the amount of CaO decreased.

So the formation of plagioclase of anorthite–CaAl<sub>2</sub>Si<sub>2</sub>O<sub>8</sub> type is more favourable than the melilite phase of gehlenite–Ca<sub>2</sub>Al<sub>2</sub>SiO<sub>7</sub> type. Anorthite, a triclinic feldspar, has an anionic structure in which Ca<sup>2+</sup> ions balance the charge on the (Al<sub>2</sub>Si<sub>2</sub>O<sub>8</sub>)<sub>2</sub>-tetrahedral units. Anorthite-containing glass-ceramics has been regarded as a potential material in low temperature co-fired ceramic (LTCC). Anorthite crystals have a tendency to coalesce into a huge domain. [27].

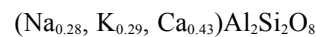
On increasing the granite/slag ratio up to 0.67 i.e., G<sub>2</sub> anorthitic plagioclase and wollastonite ss were formed. The resulting wollastonite solid solution phase may exhibit the following formula:



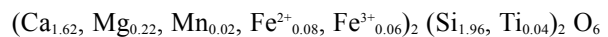
However, the presence of Na<sub>2</sub>O or K<sub>2</sub>O (in small amounts) may lead to the displacement of some Ca<sup>2+</sup> ions from the anorthite molecules–CaAl<sub>2</sub>Si<sub>2</sub>O<sub>8</sub> to form albite–NaAlSi<sub>3</sub>O<sub>8</sub> or KAlSi<sub>3</sub>O<sub>8</sub> molecules instead, which go into solid solution with the remaining CaAl<sub>2</sub>Si<sub>2</sub>O<sub>8</sub> molecules [16] during crystallization of the glass G<sub>2</sub>, giving rise to plagioclase crystals of varying compositions in the series CaAl<sub>2</sub>Si<sub>2</sub>O<sub>8</sub>–NaAlSi<sub>3</sub>O<sub>8</sub>–KAlSi<sub>3</sub>O<sub>8</sub>. Therefore, the anorthitic plagioclase formed may has the following formula:



On increasing the granite/slag ratio up to 1.0 i.e., G<sub>3</sub> resulting into increasing appreciable amount of Na<sub>2</sub>O and K<sub>2</sub>O in the original composition of G<sub>3</sub>. This increases the probability of formation of KAlSi<sub>3</sub>O<sub>8</sub>, NaAlSi<sub>3</sub>O<sub>8</sub> in solid solution with anorthite–CaAl<sub>2</sub>Si<sub>2</sub>O<sub>8</sub>, which has the probable formula:



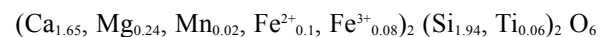
The structure of wollastonite solid solution formed in glass-ceramic G<sub>3</sub> may be had the following formula:



The increase of granite/slag ratio up to 1.5 i.e., G<sub>4</sub>, the resulting anorthitic plagioclase may exhibit the following formula:



However, structure of wollastonite ss formed in glass-ceramic G<sub>4</sub> may represent the probable formula:



#### Thermal expansion

The thermal expansion of the glass is due to anharmonicity of the atomic vibrations. The amplitudes of the thermal vibrations are small when there are many strong bonds present in the network. As a result, the thermal

expansion coefficient decreases as the rigidity of the glass network increases. The change in the thermal expansion coefficient of the glass, which is caused by different additives, is often directly proportional to the amounts of the additives [29].

The addition of granite at the expense of slag led to decrease of the expansion coefficients of the glasses. This can be explained on the basis that the addition of granite increases the rigidity of the glasses due to the increase in the amount of silica, their structure thus being more cross-linked [1]. It was found also that the amount of  $Al^{3+}$  ions (found in granite) was increased and forming  $(AlO_4)$  tetrahedra, which enter the glass network and take part in the formation of a strong aluminium-silicon-oxygen framework. Thus the amplitudes of the thermal vibrations are small and the expansion coefficients ( $\alpha$ ) of the glasses are decreased. Consequently, higher  $T_g$  and  $T_s$  temperatures could be expected on adding granite at the expense of slag.

However, the addition of lithium fluoride led to increase the expansion coefficient values of the glasses. Lithium fluoride may act as network breaker in the glassy anionic structure. This effect is reflected in decreasing the viscosity of the melt (or glass) and consequently led to increase the thermal expansion coefficient of the glass.

The thermal expansion property of the crystalline solids is quite different than that of the parent glasses. The thermal expansion coefficient ( $\alpha$ ) of the glass-ceramics is a function of the thermal expansion coefficients and elastic properties of all crystalline phases present including residual glass and the resulting microstructure. The contribution of the residual glassy phase, whose composition is altered from that of the parent glass, must be taken into account [11 and 14].

An extremely wide range of thermal expansion coefficients is covered by the different crystal types and the development of these phases in appropriate proportions forming the basis of the production of glass ceramics with controlled thermal expansion coefficients [11].

The crystallization of glasses ( $G_1$ - $G_4$ ) generally produces crystal phases such as melilite of gehlenite type, wollastonite ss and anorthitic plagioclase phases with varying expansion coefficients depending on the granite/slag ratios. The contribution of a particular crystal phase to the thermal expansion of a glass ceramic may be also modified if the crystal enters into solid solution with another phase. Gehlenite has high positive expansion of  $123 \times 10^{-7} \text{ }^\circ\text{C}^{-1}$  (20-1000 $^\circ\text{C}$ ) [30]. Wollastonite has  $\alpha$ -value of  $94 \times 10^{-7} \text{ }^\circ\text{C}^{-1}$  (100-200 $^\circ\text{C}$ ) [11, 14]. Anorthite has  $\alpha$ -values of  $51 \times 10^{-7} \text{ }^\circ\text{C}^{-1}$  (25-600 $^\circ\text{C}$ ) [31] and  $64 \times 10^{-7} \text{ }^\circ\text{C}^{-1}$  (20-1000 $^\circ\text{C}$ ) [32].

The glass-ceramics  $C_1$ - $C_4$  showed that as the amount of granite increased, the coefficients of thermal expansion of the resulting glass-ceramics decreased

(figure 6). Glass-ceramic  $C_1$  has the highest  $\alpha$ -values due to the presence of high expanding melilite of gehlenite type together with wollastonite ss phases. However increasing the granite/slag ratios ( $C_2$ - $C_4$ ) resulting into the formation of the relatively low expanding anorthitic plagioclase at the expense of the high expanding melilite phase of gehlenite type. Samples  $C_4$  and  $C_4 + LiF$  showed the lowest expansion coefficient values.

#### Chemical durability

The powdered test technique was used to assess the chemical durability of the glass and glass-ceramics. The powdered test is sought to yield a true representation of the leaching data of the materials [33]. It provides reliable information about the glasses and glass-ceramics as composite materials and not about the surface, as any effect due to differences in phase composition of the surface relative to the bulk is minimized. The relationship between temperature and time of test has been investigated [33], that one year at room temperature was approximately equivalent to 3 weeks at 50 $^\circ\text{C}$ , 2 days at 75 $^\circ\text{C}$ , or 7 hours at 95 $^\circ\text{C}$ .

Glass-ceramics are multiphase systems with each phase having individual corrosion characteristics and possible unique reactions at the phase boundaries. The multiphase microstructure can be subdivided into two categories: 1) the crystalline phase, and 2) the amorphous phases (or the residual glass phase) [34]. However, the overall durability performance of a glass-ceramic cannot be solely determined by separate phase investigations. It is essential to take the phase boundaries into consideration as well. In this study the indicator of the extent of corrosion is weight loss measurements after corrosion.

In the present work, the addition of granite at the expense of slag improved the chemical durability of the glass-ceramics  $C_1$ - $C_4$ .

The major factors influencing the overall durability of glass and glass-ceramics appear to be: 1) composition of the crystalline phases as compared with the residual glass, 2) structure and density of the crystalline phase, 3) volume fraction of crystalline phase, and 4) grain size of crystalline phase [34].

The chemical durability data revealed also that sample  $C_4$  exhibited the best durable sample. This can be explained on the basis that the sample  $C_4$  has a fine grain microstructure with small amount of residual glassy matrix as indicated from the SEM micrograph (figure 3). The dense non-porous microstructure of the glass-ceramics makes it possible to count on better chemical stability as compared with porous ceramics, which have a more extensive surface and greater penetrability to liquids and vapours [11].

Alkali metal ions are much more stable in the crystalline phase than in the residual glass phase. Consequently, alkali metal ions are more rapidly removed from the glass phase during the action of leaching solution on glass-ceramic materials [11, 14, 35]. In order that glass-ceramic materials have good chemical resistance, it is thus necessary that the residual glass phase does not contain high concentrations of the oxides of the alkali metals in particular.

However, the solubility of both the formed crystals and the residual glass phase in leaching solution has an almost equally important influence on the stability of glass-ceramics [35-36].

The leaching mechanism may involve the replacement of cations like Na<sup>+</sup> and K<sup>+</sup> with hydrogen-bearing ion from the solution leading to the formation of a leached layer, i.e. alkali depleted layer. Therefore, in acid media, the initial stage of the reactions is the diffusion of alkali ions through the glass-ceramic network and across the leached layer into the solution. The diffusion rate of alkali ions gradually slow down as the leached layer becomes thicker [35].

Kay and Doremus [37] stated that the volume of the crystals remains essentially constant with temperature as reflected in its low coefficient of thermal expansion. They suggested that the tendency of the lattice to maintain a constant volume reduces the rate of hydration reaction. This is in agreement with the results reported in the present work that the glass-ceramic C<sub>4</sub> showed a lower  $\alpha$ -values and lower leaching rate than that of the other investigated glass-ceramic materials (C<sub>1</sub>-C<sub>3</sub>). These also can explain why the anorthitic plagioclase-containing glass-ceramics C<sub>4</sub> + LiF is more durable than the melilite phase of gehlenite type-containing glass-ceramic C<sub>1</sub> + LiF.

## CONCLUSION

The glass-ceramic route can be successfully applied to the blast furnace slag provided from the Iron and Steel Company and Aswan granite with the goal of converting them into useful products.

The DTA data revealed that the sharp crystallization peaks observed is indicative of the domination of bulk crystallization mechanism. Lithium fluoride enhanced the crystallization of the glasses. Melilite phase of gehlenite type or anorthitic plagioclase together with wollastonite ss phases were mainly detected by XRD analysis depending on the granite/slag ratios. The morphology of the crystallized samples showed uniform volume crystallization of fine-grained network microstructures, which is achieved by increasing the granite/slag ratios in the glasses.

The increase of granite at the expense of slag in the glasses led to improve both the thermal expansion characteristics and the chemical durability of the materials investigated.

## References

- Holland W., Beall G. H.: *Glass-ceramic technology*, Am.Ceram.Soc.Inc., New York 2002.
- Francis A. A.: *J. Eur.Ceram.Soc.* 24, 2819 (2004).
- Karamanov A., Pelino, M.: *J.Non-Cryst.Solids* 28, 139 (2001).
- Karamanov A., Gutzow I, Chomakov I., Christov J., Kostov L.: *Glastech.Ber.Glass Sci.Technol.* 67, 227 (1994).
- Lucas A., Harris J. R.: *Ancient Egyptian materials and industries*, p. 523, Ed. Arnold E., London 1962.
- Ovecoglu M. L.: *J. Eur.Ceram.Soc.* 18, 161 (1998).
- Beall G. H. in: *Reviews of solid state science*, Vol.3, p.113, World Scientific, Singapore 1989.
- Glaze F. W.: *Chemical analysis of glass*, in: *Handbook of glass manufacture*, Vol.2, p. 57-87, Ed. Tooley F.V., Ogden Publishing Company, New York 1960.
- Bamford C. R.: *Color generation and control in glass*, Elsevier, Amsterdam 1978.
- Joint Committee on Powder Diffraction Standards (JCPDS): Files, Swarthmore, PA, USA 1999.
- McMillan P. W.: *Glass-ceramics*, Academic Press, London, New York 1979.
- MacDowell J. F.: *Alumina in glasses and glass-ceramics*, Reprinted from *Alumina Chemicals Science and Technology Handbook*, p. 365-374, Am.Ceram.Soc., Inc., New York 1990.
- Ozawa T.: *Polymer* 12, 150 (1971).
- Strnad Z.: *Glass-ceramics materials*, in *Glass science and technology*, Vol. 8, p. 185 - 252, Elsevier, Amsterdam 1986.
- Agarwal G., Hong K. S., Fletcher M. R., Speyer R. F.: *J.Non-Cryst.Solids* 130, 187 (1991).
- Deer W. A., Howie R. A., Zussman J.: *An introduction to the rock forming minerals*, Printing Press Ltd., Hong Kong 1992.
- Salama S. N.: *Mat.Chem.Phys.* 28, 237 (1991).
- Salama S. N., Salman S. M.: *J.Eur.Ceram.Soc.* 11, 179 (1993).
- Schairer J. F., Bown N. L.: *Am.J.Sci.* 240, 725 (1942).
- Salman S. M., Omar A. A., Salama S. N.: *Sprechsaal* 118, 9 (1985).
- Salman S. M., Salama S. N.: *Ceramogia* XVII, 3 (1987).
- Bowen N. L., Schairer J. F., Posnjak E.: *Am.J.Sci.Ser.* 5, 193 (1933).
- Barth T. F.: *Theoretical petrology*, Wiley, New York 1962.
- Morioka M., Kamata Y., Nagasawa H.: *Geochim.Cosmochim.Acta* 61, 1009 (1997).
- Schairer J. F., Osborn E. F.: *J.Am.Ceram.Soc.* 33, 160 (1950).

26. Goldsmith J. R.: *J.Geol.* 56, 437 (1948).
27. Nurse R. W., Midgley H. G.: *J. Iron and Steel Inst.* 147, 121 (1953).
28. Lo C. L., Duh J. G., Chiou B. S., Lee W. H.: *Mat.Res. Bull.* 37, 1949 (2002).
29. Gavrilu G.: *J.Eur.Ceram.Soc.* 22, 1375 (2002).
30. Hemingway B. S., Robie R. A.: *Am.Mineral.* 69, 307 (1984).
31. Peng F., Liang K., Hu A.: *Fuel* 84, 341 (2005).
32. Gigby G. R., Green A. T.: *Trans.Br.Ceram.Soc.* 41, 123 (1942).
33. Newton R. G.: *Glass Technology* 26, 21 (1985).
34. McCracken W. J. in: *Corrosion of glass, ceramics and ceramic superconductors*, Eds. Clark D. E., Zoitos B., Noyes Publ., Park Ridge, New Jersey 1992.
35. Lodding A., in: *Corrosion of glass, ceramics and ceramic superconductors*, Eds. Clark, D. E., Zoitos, B., Noyes Publ., Park Ridge, New Jersey, 1992.
36. Salman S. M., Salama S. N.: *J.Non-Cryst.Solids* 83, 114 (1986).
37. Kay J. F., Doremus R. H.: *J.Am.Ceram.Soc.* 57, 480 (1974).

## VÝVOJ LEVNÉHO SKLOKERAMICKÉHO MATERIÁLU NA BÁZI VYSOKOPECNÍ STRUSKY A ŽULY

SAAD MOGHAZY SALMAN, HUSSEIN DARWISH

*Glass Research Dept., National Research Centre,  
El-Behoos St., Dokki, Cairo, Egypt*

Byl zkoumán vývoj levného sklo-keramického materiálu s různým obsahem egyptské vysokopecní strusky a žuly. Vliv náhrady žula/struska na krystalizační charakteristiky skel výslednou mikrostrukturu byl sledován pomocí diferenční termické analýzy (DTA), rentgenové difrakční analýzy (XRD) a skenovací elektronové mikroskopie (SEM). Proměnlivost typů fází melilitu a gehlenitu, tuhého roztoku wollastonitu a anortických plagioklasových fází byla většinou způsobena závislostí na poměrech žula/struska u jednotlivých skel. Typy vzniklých krystalizovaných fází jsou diskutovány ve vztahu k proměnlivosti složení skel a použitému způsobu tepelného zpracování. Mikrosnímky SEM ukazují, že náhrada žula/struska podporuje krystalizaci jednotného objemu jemnozrnné propletené mikrostruktury, které se dosáhne zvyšováním obsahu žuly ve sklech. Přídavek LiF jako katalyzátoru nukleace zlepšuje charakteristiky krystalizace skel. Zvýšení obsahu žuly na úkor strusky ve sklech vedlo ke zlepšení jak tepelných expanzních charakteristik, tak chemické odolnosti zkoumaných materiálů.

# THE EFFECT OF FLY ASH ON CEMENT HYDRATION IN AQUEOUS SUSPENSIONS

DRAŽAN JOZIĆ, JELICA ZELIĆ

*Faculty of Chemical Technology, Teslina 10/V, 21000 Split, Croatia*

E-mail: jozicd@ktf-split.hr

Submitted October 31, 2005; accepted March 3, 2006

**Keywords:** Cement, Fly ash, Conductometry, TG/DTA, XRD

*Fly ash is waste material formed in coal-using thermal-power plants, and is frequently used as addition to cement and mortars/concrete. Its physical and chemical properties depend exclusively on the quality of coal used and on technological conditions of burning. This study has examined the effect of fly ash from the Plomin 2 Thermal Power Plant, Croatian Power Supply (HEP), Plomin, Croatia, on early stages of cement hydration in aqueous suspensions ( $w/s = 4$ ,  $t = 20^\circ\text{C}$ ). According to the ASTM C618 Standards, fly ash used, belongs to the F class fly ash, i.e. to low CaO content fly ash. Fly ash was added as a replacement for cement in amounts of 0, 5, 11, 15, 20, and 30 wt.%. Conductometrical measurements in suspensions have indicated that the replacement postpones the start of precipitation of  $\text{Ca}(\text{OH})_2$ , prolongs the duration of that precipitation, and reduces the overall cement hydration rate. XRD and DTA-TG/DTG measurements indicate that the share of  $\text{Ca}(\text{OH})_2$  in the solid part of the suspension decreases when the fly ash addition increases, while the results of the DTA-TG/DTG analysis corrected to the cement weight confirm the role of fly ash as nucleation site where hydration products settle, while its pozzolanic activity has not been observed in this period of hydration up to 72 hours.*

## INTRODUCTION

Various types of additions that improve cement properties have been used in the cement industry for a long time. The most frequently used materials are blast furnace slag, silica fume, fly ash or natural pozzolans such as burned clay, metakaolinite [1]. Fly ash is waste materials from the thermal power plant; it is separated from the flue gas of the power station burning pulverized coal [2]. Factors such as the origin of the coal and the burning condition, strongly affect their chemical and mineralogical composition. According to ASTM C618, two classes of the fly ash are specified Class F and C. Class F fly ash is produced by burning anthracite or bituminous coal and it is known like fly ash with low content CaO. Class C is produced by burning sub-bituminous or lignite coal and Class C is known like fly ash with high content CaO [3,4]. Fly ash is added to Portland cement or directly to mortars or concretes [5]. The use of fly ash as a replacement addition to cement in production is useful for a number of purposes: reduction of  $\text{CO}_2$  emission, reduction of power needed for cement production, reduction in the quantity of waste material and protection of natural raw materials. There are numerous studies on using the fly ash as addition to mortars/concrete and it is widely accepted that they affect fluidity, reduce the hydration heat, and block the alkali-silicate reactions [6]. The effect of fly ash on the hydration rate and on final properties of hardened cement composites depends on the chemical composi-

tion, specific surface and chemical reactivity (the content of the amorphous phase) of fly ash in cement systems [7,8].

This study has examined the physical and chemical properties of fly ash and its effect on hydration of cement containing a replacement part of fly ash in aqueous suspension systems.

## EXPERIMENTAL

The materials used in the experimental work were fly ash from the thermal power plant Plomin-2 (HEP-Plomin, Croatia) and the industrial Portland cement type CEM IIA-S 42.5N (Dalmacija cement, Croatia). Table 1 shows the chemical composition of fly ash and cement used, and the properties of class F fly ash according to the ASTM C618 Standards.

Aqueous suspensions have been prepared with the replacement part of fly ash in the amounts of 0, 5, 11, 15, 20, 30 wt.% (samples designated PF0, PF5, PF11, PF15, PF20, and PF30, respectively) with the water/solid ratio ( $w/s = 4$ ) at the hydration temperature of  $20^\circ\text{C}$ . The cement - fly ash mixture was homogenized in mills with ceramic spheres, the homogenization process lasting for 30 minutes. After adding the homogenized mixture to the thermostated water, the system was left to mix on the magnetic mixer for 5 minutes, after which a conductometrical cell was immersed to trace the changes in conductivity (Schott LF 413-3T).

The Schott CG-853 conductometer was connected to a computer via an RS232 output, and data on conductivity were collected every 5 seconds. The conductivity of the suspensions was monitored continuously up to approx 48 hours, i.e. as long as there were noticeable changes in conductivity.

In order to determine the concentration of Ca<sup>2+</sup> ions present in the aqueous phase of the suspension and the quantity of Ca(OH)<sub>2</sub> formed in the solid part of the suspension, hydration was interrupted at precisely defined time intervals, at 0.08, 0.25, 0.75, 1, 3, 7, 12, 13,16, 17, 24, 48, and 72 h. Separation solid and liquid phase was made by system vacuum filtration, solid part of the suspension is immediately mixed with acetone in order to stop the hydration and remove free water, after removing free water samples are dried in vacuum at room temperature and placed in desiccator. In liquid phase concentration Ca<sup>2+</sup> ions is determined by using complexometric methods with EDTA.

The content of the chemically bound water in the system was determined by reducing the overall loss from 105 to 1000°C by the loss of bound water and CO<sub>2</sub> due to decomposition of Ca(OH)<sub>2</sub> and CaCO<sub>3</sub>. The content of the chemically bound water and Ca(OH)<sub>2</sub> was corrected to 100% cement weight. The fineness of fly ash was expressed as the weight proportion in % of the fly ash retained when sieved on a 0.045 mm mesh sieve, according to Standards EN 450:1994. Differential thermal analysis (DTA) and thermogravimetric analysis (TG) were conducted on a Perkin Elmer simultaneous DTA/TG analyzer, the Pyris Diamond model, in the temperature range from the room temperature until 1000°C with a linear heating rate of 20°C/min in the nitrogen atmosphere. XRD powder pattern was recorded on a Philips X'Pert Pro, the PW 3040/60 model with an X-Ray tube PW 3373/00 Cu LFF DK119707 at a current of 40 mA and voltage of 40 kV, and goniometer

PW 3050/60. Recording was made in the range 4° < 2θ < 64°. The FTIR spectrum was made in KBr pastile on the Perkin Elmer spectrophotometer, the Spectrum One model, in the wave numbers range from 4000-400 cm<sup>-1</sup>.

## RESULTS AND DISCUSSION

### Properties of fly ash

Fly ash consists mainly of SiO<sub>2</sub>, Al<sub>2</sub>O<sub>3</sub>, Fe<sub>2</sub>O<sub>3</sub> and CaO components, with the (SiO<sub>2</sub> + Al<sub>2</sub>O<sub>3</sub> + Fe<sub>2</sub>O<sub>3</sub>) content of more than 70 wt.%, and with the CaO content of 2.81 wt.%. The data obtained by chemical analysis place the fly ash in the F class, i.e. the low CaO content fly ash. The weight loss (in air atmosphere and in range 30-1000°C) value of 1.60 wt.% reflects the weight of unburned carbon, sulfide, hydrate, carbonate and oxide that is present in the fly ash. Thermal analyses of the samples indicate the continuous weight loss in the range from 30-1000°C. According to the literature data in the temperature range between 500-750°C, in the inert atmosphere, degradation of carbonate can take place, just one process influence on the weight loss. In the same temperature range but in the oxidizing atmosphere unburned carbon can oxidize into carbon dioxide at the same time with the degradation carbonate, both process influences on the weight loss [9]. Figure 1 presents the DTA-TG/DTG measurements of fly ash in the two different atmospheres (air and nitrogen) with the heating rate 5°C/minutes. The quantity of unburned carbon in the fly ash has been determined. Combination heating in the limited temperature range from 438-714°C, both in oxidizing and inert atmospheres, makes it possible to resolve the unburned carbon and carbonate in the fly ash samples. From the difference of weight loss in the oxidizing and nitrogen atmosphere is calculated quantity of carbon which is presence in the fly ash (0.6 wt.%). Table 1 presents the results obtained.

Table 1. Major elements found in fly ash and the composition required by ASTM C618 for class F Fly ash, and composition of the CEM IIA-S 42.5N cement used.

Materials	Cement (wt.%)	Fly ash (wt.%)	Required by Standards ASTM C618
SiO <sub>2</sub>	21.55	59.46	(SiO <sub>2</sub> +Al <sub>2</sub> O <sub>3</sub> +Fe <sub>2</sub> O <sub>3</sub> )=Min.70%
Al <sub>2</sub> O <sub>3</sub>	5.96	19.91	
Fe <sub>2</sub> O <sub>3</sub>	2.61	9.93	
CaO	59.95	2.81	-
MgO	2.84	0.84	5.0 max.
SO <sub>3</sub>	2.83	0.18	5.0 max.
Na <sub>2</sub> O	0.22	0.40	-
K <sub>2</sub> O	0.77	1.27	-
C	-	0.60	-
Loss of ignition (1000°C)	2.8	1.6	6.0 max.
Moisture Content	0.2	0.1	3.0 max.
Specific gravity (kg/m <sup>3</sup> )	2.501	1.839	-
Specific surface (Blain) (m <sup>2</sup> /kg)	409.1	312.9	-
Normal Consistency (%)	28	-	-
Initial settings	2h 26min	-	-
Final settings	3h 15min	-	-

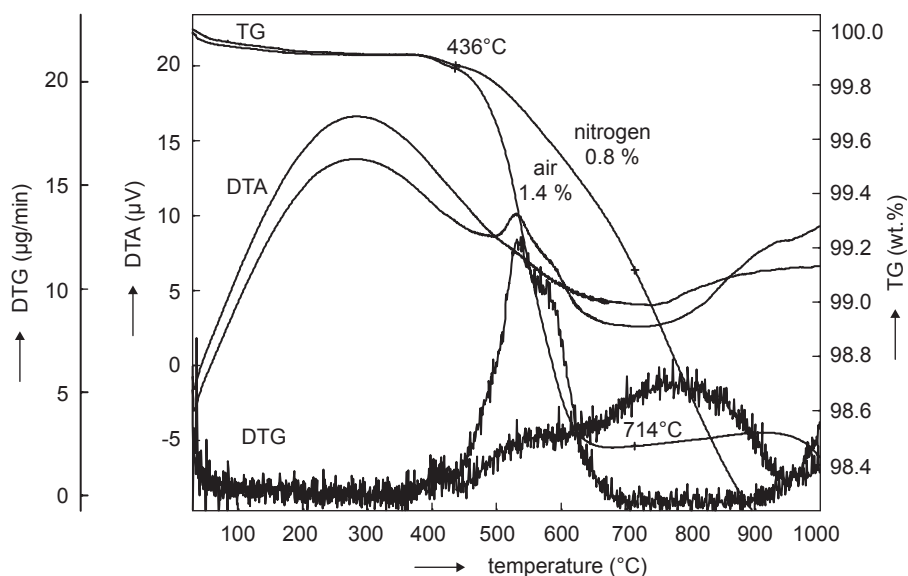


Figure 1. TG/DTA of fly ash sample with 5°C/min heating rate.

Fly ash is generally found in small spherical particles that differ significantly in size and shape (figure 2). The specific gravity of fly ash used is about 1.839 kg/m<sup>3</sup> and the specific surface area is about 312.9 m<sup>2</sup>/kg. The results of the grain size distribution analysis (obtained by sieving) show that the fraction retained on a 0.045 mm sieve is 28.2 % and the fraction passed through a 0.045 mm sieve is 71.8 %, which meets the criteria for application in production of cement/concrete required by the EN 450:1994 norm.

Figure 3 shows the XRD powder patterns of the fly ash un-fractionated (a), retained on a 0.045 mm sieve (b), and a fraction passed through a 0.045 mm sieve (c).

Qualitative analyses of the different fractions of fly ash samples were made by comparing experimental diffraction data with the diffraction data for known com-

pounds stored in the JCPDS database [10]. Diffraction powder patterns for all fractions are same, without any difference. Two diffraction maximums at  $2\theta = 44.9^\circ$  and  $38.3^\circ$  arise from the samples holder, not from sample fly ash. Other diffraction maximums which arise from the fly ash are analyses, results is the three main crystal phases were found: mullite (PDF # 15-0776), quartz (PDF # 12-0708) and hematite (PDF # 24-0072). The diffuse band are present in the region  $15^\circ < 2\theta < 30^\circ$  and it show on presence the amorphous (glass) phase. FT-IR spectrums of fly ash samples are shown in figure 4, detecting the presence of aluminosilicate with a little amount of adsorbed water.

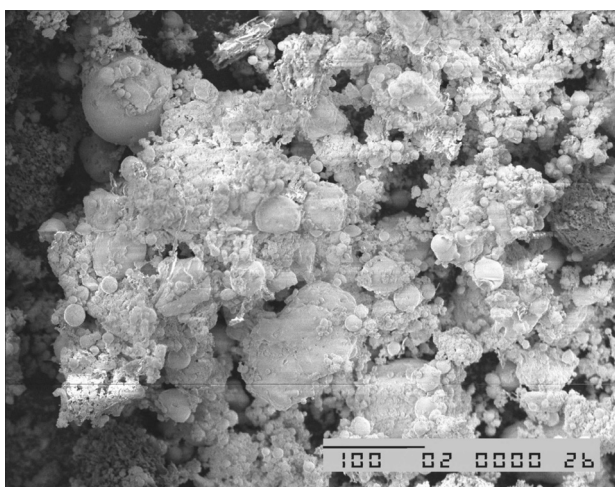


Figure 2. SEM micrograph used fly ash.

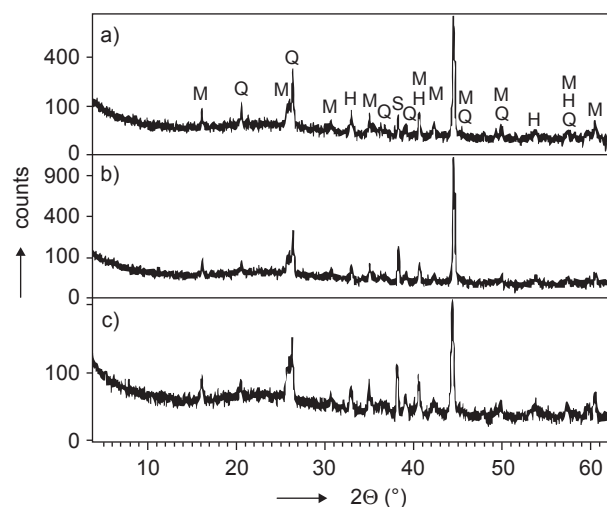


Figure 3. XRD diagram of different fractions of fly ash sample; a) un-fractionated sample, b) retained on a 0.045 mm sieve and c) fraction passed through a 0.045 mm-sieve; M - mullite, Q - quartz, H - hematite, S- sample holder.

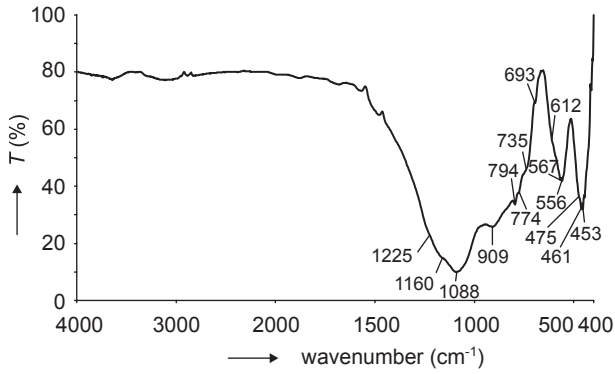


Figure 4. FT-IR spectrum of fly ash sample.

The main and very broad absorption zone appears centered at 1088  $\text{cm}^{-1}$  attributed to asymmetric stretching of O–Si–O and O–Al–O bonds, the bands at 567 and 556  $\text{cm}^{-1}$  are attributed to the bending Al–O–Si and Si–O–Si bonds, the bands at 461  $\text{cm}^{-1}$  attribute on bending O–Si–O bonds. Assigned strong and very strong absorption bands at 1160, 1088 and 794  $\text{cm}^{-1}$  attribute on the presence quartz, shoulder 612  $\text{cm}^{-1}$  and strong absorption bands at 567  $\text{cm}^{-1}$  attribute on the mullite phase but the one absorption bands characteristic for mullite phase at 1138  $\text{cm}^{-1}$  is hid with very broad band

centered at 1088  $\text{cm}^{-1}$ . Absorption bands at 1088, 612, 556, 475  $\text{cm}^{-1}$  attribute on the presence hematite phase in the sample. Broad absorption band in the area 500–650  $\text{cm}^{-1}$  indicate on the silicate and aluminosilicate glasses phase [11–14].

### Conductivity in suspensions

Measurements of conductivity in cement suspensions, pastes, and mortars are very suitable for monitoring the progress of hydration. A change in conductivity in cement suspensions relative to hydration duration has been divided into three hydration phases according to Maximilen: a) mixing, b) dormant and c) acceleration period [15].

When non-hydrated cement particles get in contact with water, various simultaneous hydration processes take place on clinker materials contained in cement, and various alkali oxides and sulfates contained in cement dissolve completely, which results in the increase of cations and anions present in the aqueous suspension, such as  $\text{Ca}^{2+}$ ,  $\text{K}^+$ ,  $\text{Na}^+$ ,  $\text{SO}_4^{2-}$ ,  $\text{OH}^-$ . The first conductometric maximum is determined by the number and mobility of ions present [16]. C–S–H and the ettringite phase, as hydration products on the surface of non-

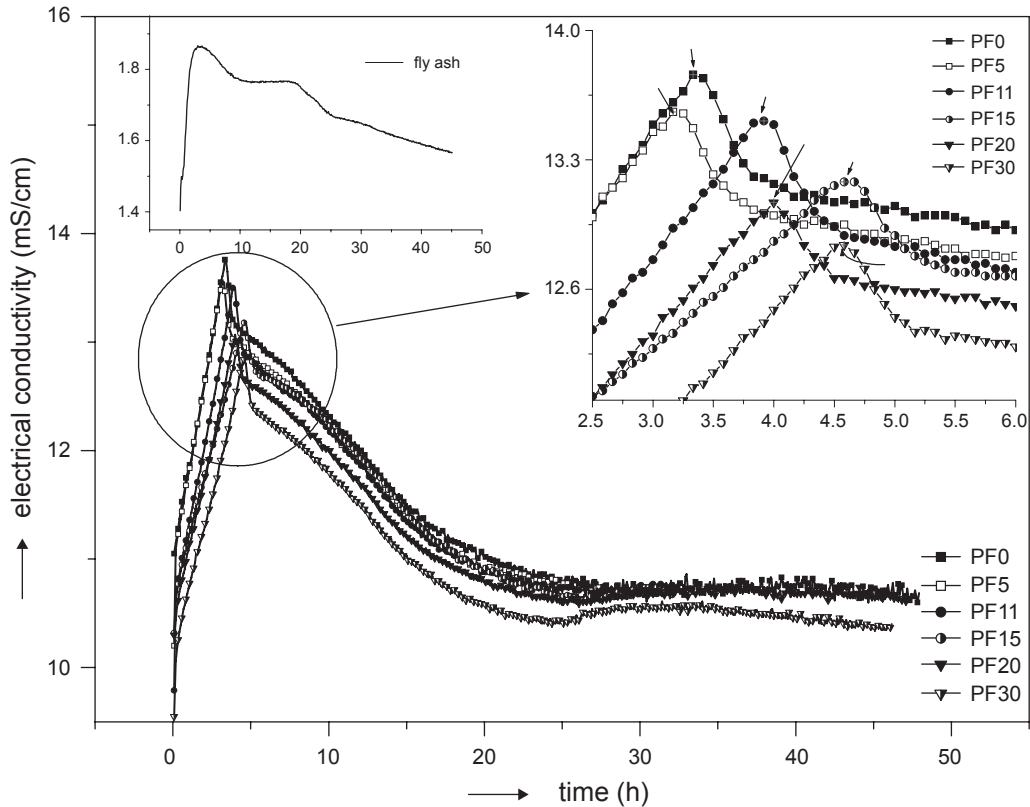


Figure 5. Change in electrical conductivity in aqueous suspension ( $w/s = 4$ ) for sample PFO, PF5, PF11, PF15, PF20 and PF30 relative to hydration duration.

hydrated cement grain, are known to be poorly conductive phases that upon formation lead to a drop in conductivity (phase b), but as the CH nucleation process is rather slow, the concentration of  $\text{Ca}^{2+}$  and  $\text{OH}^-$  ions increases in the solution which in turn increases conductivity until supersaturation which reaches its maximum there. The curves of changes in conductivity in the fly ash - cement aqueous suspension systems, shown in figure 5, indicate a conductivity maximum in the interval between 3.3 and 4.6 hours of hydration. Addition of fly ash to the system postpones the maximum of conductivity, which decreases with the increase of the addition (table 2). The change of the slope of the conductivity change line relative to hydration duration in phase b reflects the effect of the addition on the cement hydration rate: the lower the line slope, the lower the hydration rate [17]. The results indicate that the addition of fly ash slows down cement hydration. However, when the solubility product constants are reached,  $K_{\text{sp}}[\text{Ca}(\text{OH})_2]$ , portlandite suddenly precipitates which is manifested by a sudden drop in the conductivity of the system [15,16]. The precipitation of  $\text{Ca}(\text{OH})_2$  takes 26 to 54 minutes, followed by a slower drop in conductivity, which suggests further progress of hydration in the system. This is probably due to breaking of the membrane of hydration products formed around the non-

hydrated cement grain (due to the action of the osmotic pressure) and to transformation of ettringite into monosulfate with constant separation of portlandite and continuous drop in conductivity until approx. 24 hours of hydration, after which conductivity becomes balanced and hydration processes are strictly limited to diffusion processes of hydration [18,19]. In systems with addition of 20 or 30 wt.% of fly ash, a mild increase of conductivity in the system is encountered again after 24 hours of mixing.

Figure 6 shows that the change in concentration of  $\text{Ca}^{2+}$  ions in the aqueous suspension phase, expressed as the change in CaO concentration in the systems, follows the change in conductivity in the suspensions (figure 5).

The maximum concentration of  $\text{Ca}^{2+}$  ions present in the liquid phase is achieved after 3 hours of hydration, followed by a continuous drop in concentration which becomes slower after 24 hours of hydration, and concentration continues to decrease until 72 hours of hydration. In systems with increased addition of fly ash (15, 20, and 30 wt.%), there occurs an increase in the concentration of  $\text{Ca}^{2+}$  ions in the period of hydration after 24 hours, which confirms the results obtained by conductometric measurements, indicating that hydration continues and more active in the systems with addition fly ash.

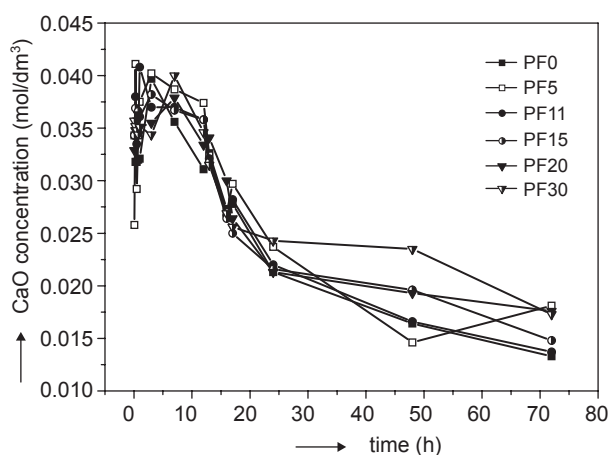


Figure 6. Change in  $\text{Ca}^{2+}$  ion concentration (expressed as CaO) in the cement suspension solution relative to hydration duration.

#### XRD analysis of the solid residue

The mineralogical composition of the solid hydration residue has been analyzed by means of the XRD method, as shown in figure 7. Diffraction patterns of a sample without fly ash (PF0) and of a sample containing fly ash (PF30) confirm the presence of the same phases after 24 hours of hydration. The major crystalline phases present in the system are: tri-calcium silicate ( $\text{C}_3\text{S}$ ) (PDF # 49-0442), di-calcium silicate ( $\text{C}_2\text{S}$ ) (PDF # 33-0302), tri-calcium aluminate ( $\text{C}_3\text{A}$ ) (PDF # 33-0251), calcium hydroxide ( $\text{Ca}(\text{OH})_2$ ) (PDF # 04-0733), calcium carbonate ( $\text{CaCO}_3$ ) (PDF # 05-0586), ettringite (PDF # 72-0646), and brownmillerite ( $\text{C}_4\text{AF}$ ) (PDF # 30-0226). If the share of fly ash is higher than 11 wt.%, the diffraction patterns show diffraction maximums that can be attributed to quartz (PDF # 70-2517) and mulite (PDF # 15-0776) and which are due to the fly ash addi-

Table 2. Results obtained with the conductometric measures.

Sample	Initial conductivity (mS/cm)	Maximum conductivity (mS/cm)	Duration of max. conductivity (h)	Duration of precipitation $\text{Ca}(\text{OH})_2$ (min)
PF0	11.15	13,76	3.33	29
PF5	11.09	13.56	3.17	26
PF11	11.66	13.51	3.92	40
PF15	10.62	13.18	4.00	33
PF20	10.44	13.07	4.58	54
PF30	10.06	12.84	4.58	54

tion: this is best shown in the PF30 sample as in figure 7. The presence of the amorphous C-S-H gel has been observed in all the system, indicated by the presence of a wide diffusion diffraction maximum in the angular range of 20-42° 2θ. The crystal form of gypsum has not been found in the system as it has probably been consumed in formation of ettringite in the early hydration phase.

The comparison of integrated intensities belonging to the Ca(OH)<sub>2</sub> phase in the angular range where there is no overlapping with other phases, i.e. in the angular ranges from 17-19° 2θ and 46-48° 2θ, (figure 8) indicates that the content of Ca(OH)<sub>2</sub> formed by hydration decreases with the increase of the fly ash addition in the mineral mixture.

Diffraction patterns of polycrystalline samples indicate that the largest share of the crystal Ca(OH)<sub>2</sub> phase is observed in samples without fly ash (PF0) for all hydration durations observed (until 72 hours).

DTA-TG/DTG analysis was used to quantify the Ca(OH)<sub>2</sub> formed in the solid part of the suspension blocked by hydration. Hydration in aqueous suspensions was interrupted at precisely defined hydration times (5 minutes - 72h).

The Ca(OH)<sub>2</sub> decomposition takes place in the temperature interval from 400-550°C (figure 9). The values obtained for the Ca(OH)<sub>2</sub> content in samples with the

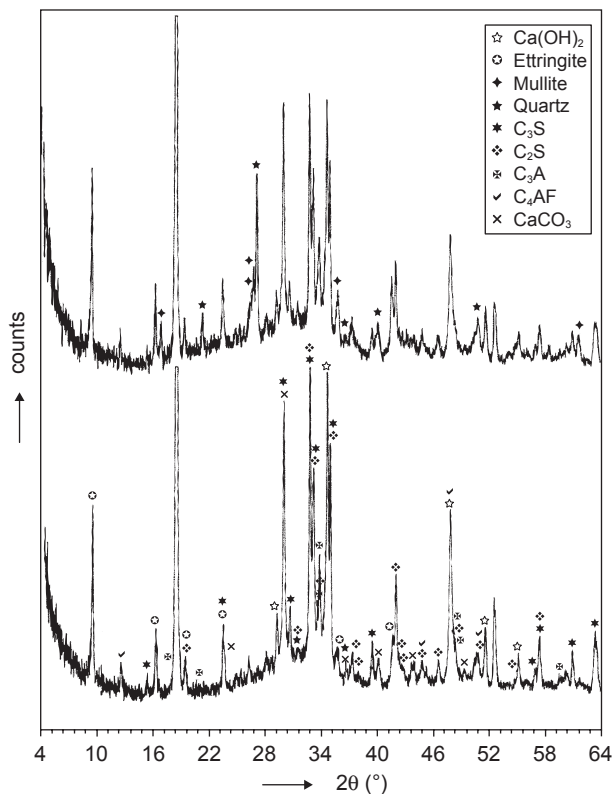


Figure 7. XRD patterns of PF0 and PF30 samples after 24 hours of hydration.

addition of fly ash have been corrected to 100 % cement weight. Figure 10 presents the results for the change in Ca(OH)<sub>2</sub> content in samples examined during hydration from 5 minutes to 72 hours, corrected to 100 % cement weight.

The results obtained indicate that in the cement suspension systems Ca(OH)<sub>2</sub> precipitates much sooner than assumed based on conductometric measurements. DTA-TG/DTG measurements have indicated the presence of Ca(OH)<sub>2</sub> even in systems 5 minutes old. The DTA signal and the weight loss in the temperature interval from 330-460°C indicate an endothermic change that may be attributed to the Ca(OH)<sub>2</sub> decomposition, but which cannot be confirmed by XRD because of a very high share of amorphous and crystal phase in the system and a very small share and low degree of order in the crystal Ca(OH)<sub>2</sub> phase in that hydration period. A sudden increase in the Ca(OH)<sub>2</sub> content occurs in the period between 3 and 7 hours of hydration. In the period between 7 and 13 hours of hydration, the Ca(OH)<sub>2</sub> content is observed to be almost constant [20], followed

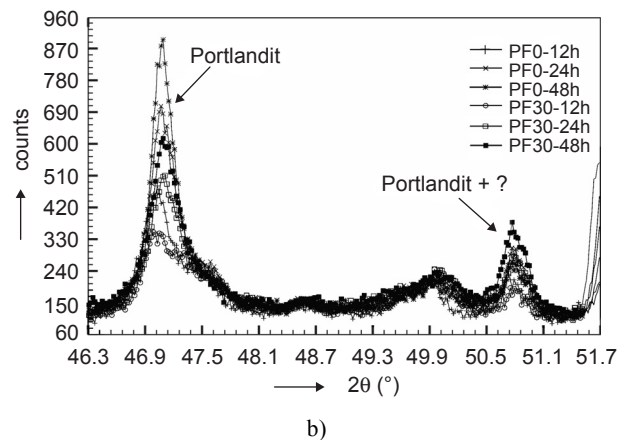
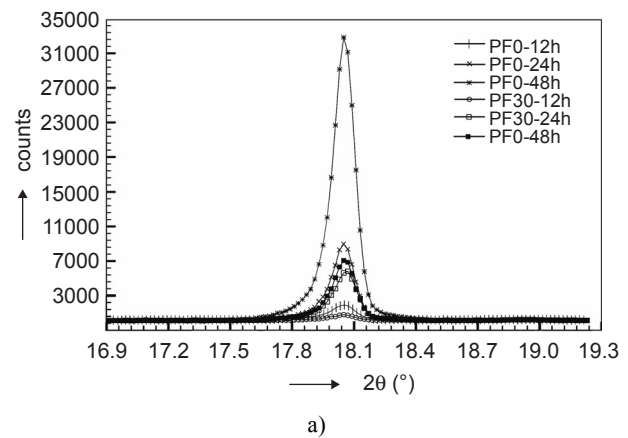


Figure 8. XRD of PF0 and PF30 samples after 12, 24, and 48 hours of hydration: a) 2θ from 17.4° to 18.8°; b) 2θ from 46.8° to 48.1°.

by a further increase in the  $\text{Ca}(\text{OH})_2$  content in the solid suspension residue. If the content of fly ash in the systems is compared to  $\text{Ca}(\text{OH})_2$  formed, it can be seen that after 48 hours of duration the  $\text{Ca}(\text{OH})_2$  content is lowest in systems without fly ash addition. The  $\text{Ca}(\text{OH})_2$  content in systems with addition of more than 5 wt.% of fly ash is higher than that in the cement without fly ash addition (the PF0 sample) already after 24 hours of hydration.

The values obtained for the content of chemically bounded water in the solid suspension residue have been calculated to 100 % cement weight and shown in figure 11. There is a continuous increase of chemically bounded water in all systems in the whole measuring range. The increase of bound water is observed in the

period after 24 hours in the systems containing the fly ash addition in comparison with the system without the fly ash addition. This indicates the increase in hydration products. As the share of chemically bound water increases and there is a simultaneous increase of the  $\text{Ca}(\text{OH})_2$  content in systems containing the fly ash addition, it may be assumed that fly ash increases the cement hydration degree. This indicates that the addition of fly ash plays a very important role as nucleation site where hydration products precipitate, which accelerates the hydration reaction. As no drop in the  $\text{Ca}(\text{OH})_2$  content has been observed in samples containing the fly ash addition, the pozzolanic reaction may be assumed to take place later in comparison with the cement hydration reaction.

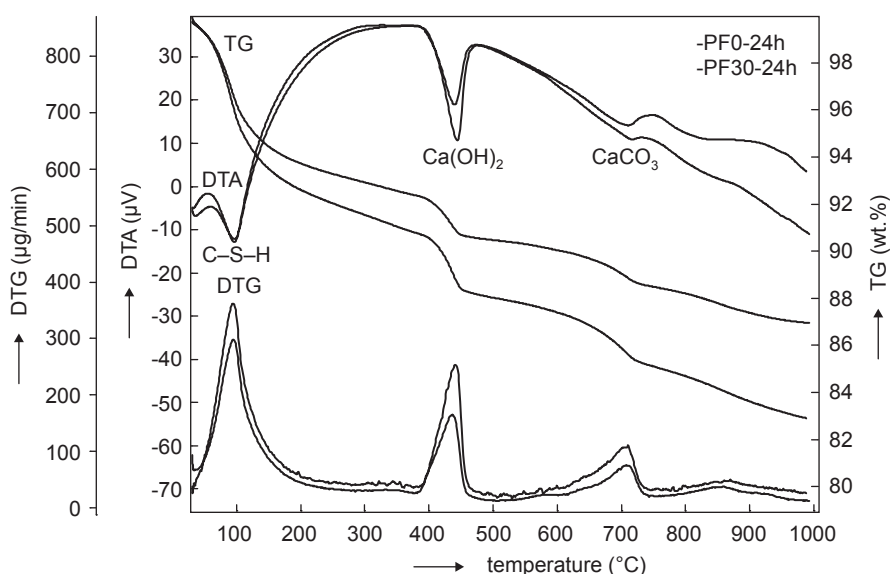


Figure 9. DTA-TG/DTG thermal decomposition of hydration products in the PF0-24h and PF30-24 h samples.

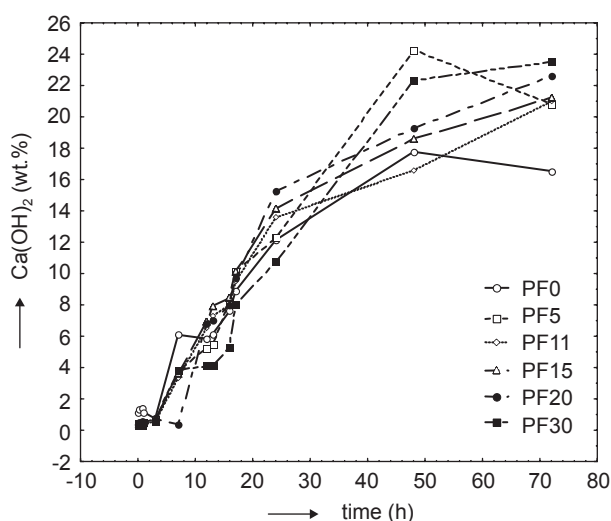


Figure 10. Change in the content during 72-hours' hydration (wt.%)  $\text{Ca}(\text{OH})_2$  in solid hydrated residue after filtering and stopping of further hydration.

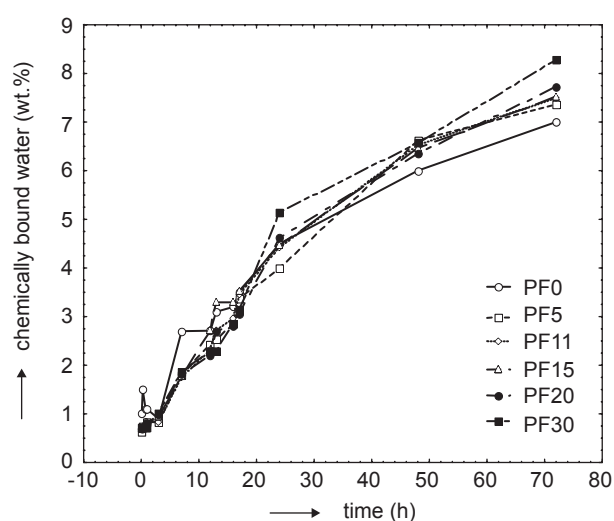


Figure 11. The content the chemically bounded water in the PF0, PF5, PF11, PF15, PF20 and PF30 samples.

## CONCLUSION

The fly ash from TE Plomin-2 belongs to the low CaO content fly ash group by its physical and chemical properties and according to the ASTM C618 Standards, which places it in the F class and makes it applicable as addition to cement/concrete according to the EN 450:1994 Standards. The results of examination of aqueous suspensions ( $w/s = 4$ ) of the cement-fly ash system indicate that the replacement part of fly ash from 5 to 30 wt.% slows down the hydration rate, increases the cement hydration degree, postpones the beginning of  $\text{Ca(OH)}_2$  precipitation by as much as 78 minutes, and increases the time of sudden precipitation by 28 minutes in comparison with the cement without the fly ash addition. For all hydration times, the  $\text{Ca(OH)}_2$  content (without correction to 100 % cement weight) is highest in samples without the addition of fly ash, which leads to the conclusion that the addition of fly ash reduces the content of free chemically reactive  $\text{Ca(OH)}_2$ . The results of the DTA-TG/DTG analysis confirm XRD measurements. However, after correction to 100 % cement weight, the results obtained indicate that the hydration degree is higher in the systems containing the fly ash addition than in the pure cement, which can be seen from the content of  $\text{Ca(OH)}_2$  and the chemically bound water. Continuous increase in the content of chemically bound water and  $\text{Ca(OH)}_2$  indicates that the pozzolanic reaction is postponed in the cement-fly ash aqueous suspension systems until 72 hours of hydration in comparison with cement hydration reactions.

## Acknowledgement

Support by the Ministry of Science and Technology of Croatia under the Project No. 0011012 is gratefully acknowledged. The authors would like to thank the Faculty of Science, Department of Geology University of Zagreb, Croatia for the use of the XRD equipment and Croatian Power Supply (HEP) Plomin d.d. for providing fly ash samples and giving permission to publish this paper.

## References

1. Targan Ş., Olgun A., Erdogan Y., Sevinc V.: *Cem.Conc. Res.* 33, 1175 (2003).
2. Taylor H.F.W.: *Cement Chemistry*, p.276-316, Academic Press Limited, London 1992.
3. Tsimas S., Moutsatsou-Tsima A.: *Cem.Conc.Res.* 27, 231 (2005)
4. Zelić J., Jozić D.: *Proc. 1<sup>st</sup> International Symposium on Environmental Management*, p.65. Ed. N. Koprivanac.
5. Rahhal V., Talero R.: *J.Therm.Anal.Calori.* 78, 191 (2004).

6. Sakai E., Miyahara S., Ohsawa S., Lee S.-H., Daimon M.: *Cem.Conc.Res.* 35, 1135 (2005).
7. Li G., Wu X.: *Cem.Conc.Res.* 35, 1128 (2005).
8. Roy D. M., Arjunan P., Silsbee M. R.: *Cem.Conc.Res.* 31, 1809 (2001).
9. Payá J., Monzó J., Borrachero M. V., Perris E., Amahjour F.: *Cem.Conc.Res.* 28, 675 (1998).
10. JCPDS (1996): Powder Diffraction file PDF-2 Database sets 1-46, International Center for Diffraction Data, Philadelphia
11. Lee W. K. W., van Deventer J. S. J.: *Colloids Surfaces A* 211, 49 (2002).
12. Mollah M. Y. A., Kesmez M., Cocke D. L.: *Sci. Total Environ.* 325, 255 (2004).
13. Biakiaris D., Daniilia S., Sotiropoulou S., Katsimbiri O., Pavlidou E., Moutsatsou A.P., Chrysosoulakis Y.: *Spectrochim.Acta A* 56, 3 (2000).
14. van Jaarsveld J.G.S., van Deventer J.S.J., Lukey G. C.: *Mater.Lett.* 57, 1272 (2003).
15. Maximilien S., Péra J., Chabannet M.: *Cem.Conc.Res.* 27, 63 (1997).
16. Heikal M., El-Diamony H., Morsy M. S.: *Cem.Conc. Res.* 30, 1827 (2000).
17. Peschard A., Govin A., Pourchez J., Fredon E.: *J.Eur. Ceram.Soc.* (in print).
18. Salem T. M.: *Cem.Conc.Res.* 32, 1473 (2002).
19. Saad Morsey M., Abo El-Enein S. A., Hanna G. B.: *Cem.Conc.Res.* 27, 1307 (1997).
20. Zelić J., Rušić D., Veža D., Krstulović R.: *Cem.Conc. Res.* 30, 1655 (2000).

## VLIV POPÍLKU NA HYDRATACI CEMENTU VE VODNÝCH SUSPENZIÍCH

DRAŽAN JOŽIĆ, JELICA ZELIĆ

Faculty of Chemical Technology,  
Teslina 10/V, 21000 Split, Croatia

Popílek je odpadní materiál vznikající při spalování uhlí v tepelných elektrárnách a je hojně používán jako přísada do cementu, malty či betonu. Jeho fyzikální a chemické vlastnosti závisejí výhradně na kvalitě použitého uhlí a na technologických podmínkách spalování. Tato studie zkoumala popílek z tepelné elektrárny Plomin 2, Chorvatské energetické závody (HEP), Plomin, Chorvatsko v počátečních fázích hydratace cementu ve vodných suspenzích ( $w/s = 4$ ,  $t = 20^\circ\text{C}$ ). Podle normy ASTM C618 odpovídá použitý popílek třídě F, tj. popílkům s nízkým obsahem CaO. Popílek byl přidáván jako náhrada cementu v množstvích 0, 5, 11, 15, 20 a 30 hmotn. %. Konduktometrická měření suspenzí ukázala, že náhrada odsunuje počátek srážení  $\text{Ca(OH)}_2$ , prodlužuje trvání tohoto srážení a snižuje celkovou rychlost hydratace cementu. XRD a DTA-TG/DTG měření ukazují, že podíl  $\text{Ca(OH)}_2$  v pevné části suspenze se zvyšujícím se přidavkem popílků klesá, zatímco výsledky DTA-TG/DTG analýz korigované na hmotnost cementu potvrzují funkci popílků jako nukleačních zárodků v místě usazování produktů hydratace, zatímco jeho pucolánová aktivita v této fázi hydratace (do 72 hodin) nebyla pozorována.

# HYDRATION AND MICROSTRUCTURE OF BINDER COMPOUNDS CONTAINING $C_2AS$ AND $C_2S$ SYNTHESIZED BY SOL-GEL METHOD

MARTIN DOVÁL, MARTIN PALOU, VLADIMÍR KOVÁR

*Faculty of Chemical and Food Technology, Slovak University of Technology,  
Radlinského 9, 812 37 Bratislava, Slovak Republic*

E-mail: martin.doval@stuba.sk

Submitted January 30, 2006; accepted February 17, 2006

**Keywords:** Sol-gel method, Hydration, Gehlenite hydrate, Ettringite

*Sol-gel method has been used to synthesize the nano particles of  $C_2AS$  and  $C_2S$ . These cement phases prepared by solid-state reaction at high temperatures are hydraulically latent or less active. After heating at  $600^\circ C$ , they were calcined at  $900^\circ C$  and  $1100^\circ C$  to obtain crystals of  $C_2S$  and  $C_2AS$  respectively. Binder compounds in the framework of  $C_2AS-C_2S-C_4A_3\bar{S}-C\bar{S}-C$  system were prepared using  $C_2AS$  and  $C_2S$  synthesized via sol-gel process. Samples showed better hydraulic activity when comparing it with the system, where pure minerals were used. The hydration of this system leads to coexistence of two crystalline hydrates of gehlenite hydrate and ettringite, which were originated by primary and secondary reactions. Gehlenite hydrate as well as ettringite were stable.*

## INTRODUCTION

Synthesis and preparation of cement phases are essentially realized by conventional methods that assure the formation of these binder materials by solid state reaction at high temperatures. The processing includes mixture and homogenization of finely ground natural raw materials or chemical reagents, following by thermal treatment at adequate temperature. This technical operation leads to the formation of crystal phases (minerals), that after grinding can react with water to form material with binding properties. Some of these minerals have not good hydraulic properties and some ones are hydraulically latent, even though their important presence in cement. Research in cement chemistry realized in the last years mapped over the possibility to synthesize highly pure cement phases using starting materials different from the usual ones and treatments at lower temperatures, using alternative synthesis methods [1-4]. These non traditional methods include: pyrolysis of solutions of some salts, precipitation from solutions, sol-gel processing and hydrothermal steam processing. From the non-conventional methods, namely those that realize the mixing and homogenizing of the raw materials at a molecular scale by wetting process, can produce very reactive samples of binding compounds able to react with water at low temperatures. These alternative methods for the synthesis of binding compounds present some advantages: low synthesis temperatures comparatively with those of the traditional methods; the advanced homogeneity of the starting material, often at molecular level; products with fine grained powders and

a strict control of the grain size distribution can be obtained; very pure and homogeneous compounds and very reactive compounds can be obtained [2-7].

Cements based on  $C_2S$  and  $C_2AS$  are generally classified as Low-Energy-Cements due to the temperatures at which they are producible [9-11]. Unfortunately,  $C_2S$  is hydraulically less active [9] and  $C_2AS$  latent phase [11]. Some progress has been realized to improve the hydraulicity of  $C_2S$  by stabilizing with minor oxides the high temperature  $\beta-C_2S$  polymorph [12,13]. Indeed, the transformation at lower temperature (about  $550^\circ C$ ) of  $\beta-C_2S$  to the  $\gamma-C_2S$  is accompanied by a volume increase responsible for the well-known phenomenon of dusting. Furthermore,  $\gamma-C_2S$  has not hydraulic properties [14]. Also, the effect of grain size upon the stabilization of  $\beta-C_2S$  has been investigated and it was found that micro-particles of  $\beta-C_2S$  having no overcome the critical size are stabilized without doping or rapid cooling [14]. Next to  $C_2S$ ,  $C_2AS$  is one of the clinker minerals of Low-Energy Cements (LEC). Its formation occurs as an intermediary product formed at  $800^\circ C$  during the burning of Portland cement [15], but gehlenite is hydraulically latent and could not contribute to the properties of binder materials. Nevertheless, gehlenitehydrate  $C_2ASH_8$  has been obtained by hydrating gehlenite glass prepared by melting a mixture of  $CaO$ ,  $Al_2O_3$  and  $SiO_2$  in molar ratio of 2:1:1 at  $1630^\circ C$ , following by rapid quenching in water [16]. Also, gehlenite hydrate is found as hydration product of cement containing blast furnace slag [17-19]. Currently gehlenite is as melted glass phase in slag. The obtention of gehlenitehydrate by this procedure is high energy consumption way.

Recently, authors [20] have explored the hydraulic properties of  $C_2AS-C_2S-C_4A_3\bar{S}-C\bar{S}-C$  system in hydrothermal conditions. The computational method has established quaternary and ternary phase associations, which hydration could give two crystallohydrates: gehlenite hydrate and ettringite (figure 1). Under hydrothermal steam conditions, ettringite formed at early hydration period is not stable and converts to monosulfate, while gehlenite hydrate formed by primary and secondary reactions remains stable.

With regard to the energy cost and technical conditions to prepare the gehlenite glass and the non-equilibrium condition of hydration in autoclave [16, 20], the present work was undertaken to find an alternative method (sol-gel process) allowing to synthesize gehlenite and  $\beta-C_2S$  without dopant, both with high hydraulic reactivity.

Sol-gel process, as an alternative to the conventional method [21] has been already used by Roy and Oye-fesobi, and that for the first time, to synthesize  $C_2S$  from aqueous silica sol and a  $Ca(NO_3)_2$  solution as precursors, the mole ratios  $Ca/Si$  were 2:1. The obtained gels were, after washing dried and then heated at  $700^\circ C$ .  $\beta-C_2S$  with fibrous shape and a very high specific surface area (of about  $12.9\text{ m}^2/\text{g}$  BET) was identified. The compressive strength developed by this compound was about 62 MPa, as compared to 40 MPa for commercial  $\beta-C_2S$  measured in the same conditions. Thereafter, sol-gel process has offered an alternative route to prepare highly active dicalcium silicate.

$C_2S$  and  $C_2AS$  are ones of the main phases of Low-Energy Cements based on belite and calcium-sulfoaluminate cements in the framework of  $C_2AS-C_2S-C_4A_3\bar{S}-C\bar{S}-C$  system [20]. Unfortunately, the rate of hydration of these cements are inhibited by the worse reactivity of minerals gehlenite and dicalcium silicate prepared by conventional method and the lack of calcium silicate hydrate in the matrix of cement paste at beginning of hydration enables the formation of ettringite that is not always stable.

In the present investigation, hydraulic properties of  $C_2AS-C_2S-C_4A_3\bar{S}-C\bar{S}-C$  system are explored, using nano particles of  $C_2AS$  and  $C_2S$  synthesized by sol-gel

method. Other phases  $C_4A_3\bar{S}$ ,  $C\bar{S}$  and  $C$  have been obtained by conventional procedure. The hydration reaction, as previously investigated has to lead to the formation of two crystallohydrates: gehlenitehydrate and ettringite [20].

## EXPERIMENTAL

Homogenized mixture of reagent grade  $CaCO_3$ ,  $Al(OH)_3$  and  $CaSO_4 \cdot 2H_2O$  was burnt twice for two hours at  $1250^\circ C$  in platinum crucible to synthesize  $C_4A_3\bar{S}$ . The obtained mineral was milled to specified fineness (to pass a 40 m sieve). Purity of this mineral was controlled by STOE Powder Diffraction System using  $CoK_\alpha$  radiation, operating at 40 kV and 30 mA. Data were collected over  $2\theta$  between 10 to  $60^\circ$ . Assignment of lines was made by comparison with JCPDS files.

$C_2AS$  gel was prepared using commercial boehmite powder (Condea Pural SB, ~ 5 nm, Condea, Germany), silica sol (Tosil, 30 wt.% of silica, particles ~ 20 nm, TONASO Neštence, Czech Republic) and solution of  $Ca(NO_3)_2 \cdot 4H_2O$  ( $c = 1.234\text{ mol/l}$ ). Water boehmite suspension was peptized by mixing with  $HNO_3$  ( $pH \approx 2.5$ ) at  $55^\circ C$ . Then the calculated amount of the silica sol and solution of  $Ca(NO_3)_2 \cdot 4H_2O$  were slowly added into the boehmite suspension. The same procedure was used to prepare nano-crystalline  $C_2S$  from stoichiometrically mixture of silica sol and solution of  $Ca(NO_3)_2 \cdot 4H_2O$ . The sol was poured onto a glass plate and was gelled. Afterwards, gels were dried at  $100^\circ C$  and then gradually heated at from  $500^\circ C$  to  $1250^\circ C$ . Calcium hydroxide (CH) was used instead calcium oxide (C) and anhydrite ( $C\bar{S}$ ) was substituted by gypsum ( $C\bar{S}H_2$ ).

Then, series of samples were prepared by mixing and homogenizing minerals and xerogels in the proportion as elucidated in Table 1. The hydration of samples at defined water/cement ratio was performed by using conduction calorimeter at  $25^\circ C$  [22]. Mineralogical composition of samples was derived from gehlenite hydrate/ettringite ratio as described in figure 1.

Table 1. Studied samples.

Samples	1	2	3	4	5	6
$C_2S$ (%)	0	10.15	20.31	28.06	12.56	0
$C_2AS$ (%)	100	63.83	27.67	0	0	0
$C_4A_3\bar{S}$ (%)	0	17.98	35.97	49.72	38.82	29.98
$C\bar{S}$ (%)	0	8.02	16.04	22.20	39.82	53.48
C (%)	0	0	0	0	9.13	16.53
Gehlenite hydrate: ettringite	100:0	80:20	60:40	44.7:55.3	20:80	0:100

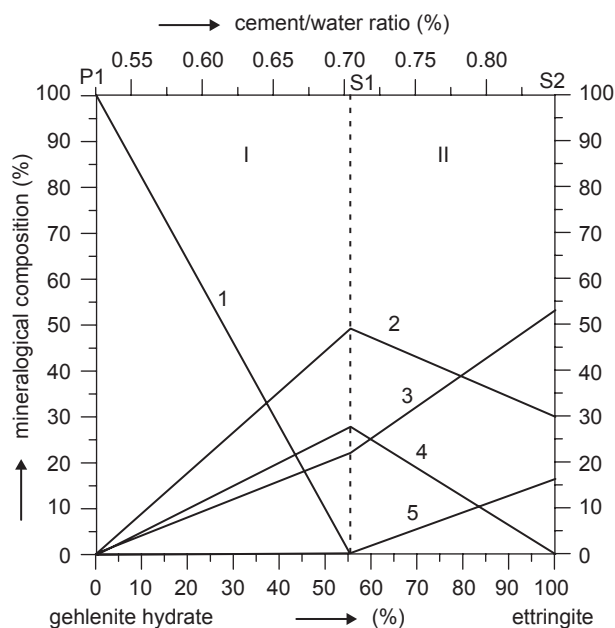


Figure 1.  $C_2AS(1)-C_4A_3S(2)-C_5S(3)-C_2S(4)-C(5)$  system and phase associations (I, II), singular points (S1, S2) and gehlenite point (P1) [20].

## RESULTS AND DISCUSSION

### Formation and hydraulic activity of $C_2S$

Figure 2 presents the degree of crystallization of xerogel of  $C_2S$  with temperature. As it can be seen, diffraction peaks of  $C_2S$  become narrower with increasing temperatures. In addition, main diffraction intensity for  $C_2S$  appears at  $600^\circ C$  between  $2\theta$   $37-38^\circ$ , confirming that the nucleation and crystallization of this phase starts at lower temperatures. With increasing heating temperature, the crystallization of this phase is well emphasized and the broad peak appeared in sample heated at  $600^\circ C$  is divided into 2 peaks measured at  $d = 2.28 \text{ \AA}$  and  $d = 2.74 \text{ \AA}$ . Assignment of lines of diffraction peaks compared with JCPDS files demonstrates the presence of  $\beta-C_2S$  as an unique and pure phase. As xerogel  $C_2S$  was not doped, it can be proposed that sol-gel technique will be a suitable method to synthesize  $C_2S$  without stabilizer. Also, the reaction processes and transformations that occur during the heating of  $C_2S$  were evidenced by the DTA curve.

The hydration activities of xerogels of  $C_2S$  calcined at  $600^\circ C$  and  $900^\circ C$  were investigated at  $25^\circ C$ ,  $40^\circ C$ ,  $50^\circ C$  and  $70^\circ C$ . The results are presented by figures 3 and 4. Gel  $C_2S$  annealed at  $600^\circ C$  is hydraulically active as demonstrated by calorimetric curves showing two peaks separated by induction period (figure 3). The intensity of hydration reaction increases with increasing

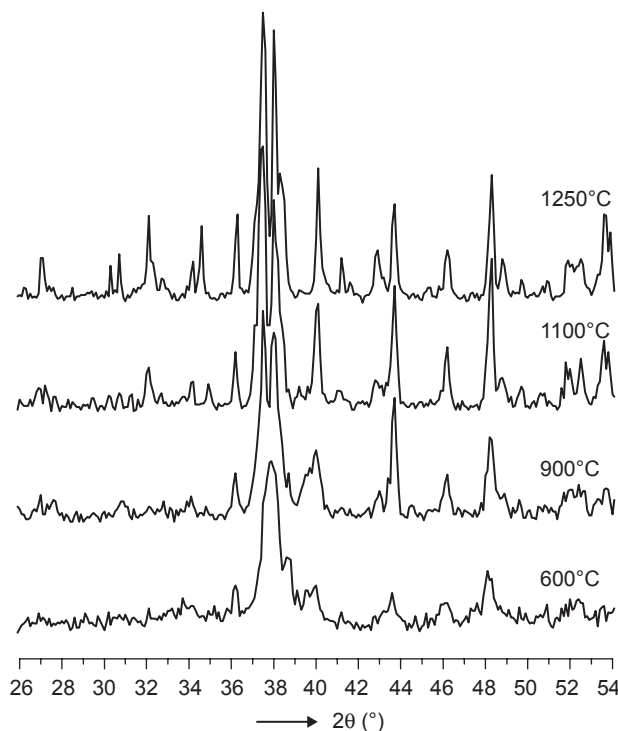


Figure 2. XRD diffraction patterns of  $C_2S$  xerogels calcined at different temperatures.

temperature at which measurements were performed. While  $C_2S$  prepared by conventional method has lower hydraulic activities [23], nano particle of  $C_2S$  as xerogel with high specific surface exhibits high hydration rate.

The rate of hydration heat with temperature of xerogel calcined at  $900^\circ C$  is reported in figure 4. The calorimetric curves present one peak. The absence of second peak demonstrates that hydration is considerably reduced. When the samples are crystallized, the specific surface decreases and  $C_2S$  becomes less and less active. In addition, hydration reaction rate of  $C_2S$  calcined at  $900^\circ C$  increases with increasing temperatures. The nano particles of  $C_2S$  hydrated show a microstructure with C-S-H after one day, and then the crystals are well developed after 7 days of curing (figures 5 and 6).

### Formation and hydraulic activity of $C_2AS$

Figure 7 shows the crystallization progress of  $C_2AS$  xerogel. Diffraction peaks characterizing the presence of  $\beta-C_2S$  appear in samples heated at  $600^\circ C$ . Gradually with heating temperatures, this peak disappears and the diffraction peak at  $2\theta = 36.56^\circ$  characterizing gehlenite appears according to JCPDS. These findings confirm that  $\beta-C_2S$  reacts with alumina (reaction (1)) to form  $C_2AS$  crystal as demonstrated by diffraction peaks for gehlenite.



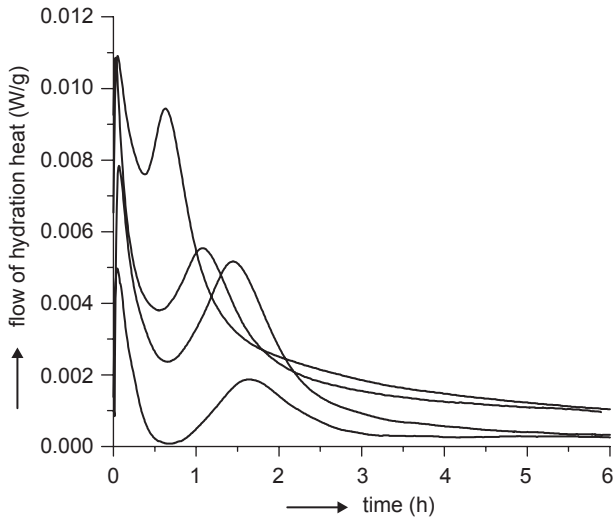


Figure 3. Calorimetric curves of nano-crystalline  $C_2S$  calcined at  $600^\circ C$ ;  $w/c = 0.5$ .

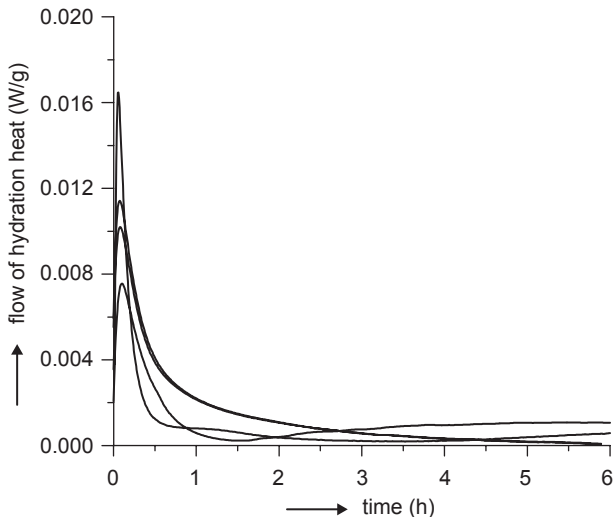


Figure 4. Calorimetric curves of nano-crystalline  $C_2S$  calcined at  $900^\circ C$ ;  $w/c = 0.5$ .

The positions of the peaks are the same but the peak intensities differ due to the crystallinity of the dicalcium silicate and gehlenite.

Calorimetric measurements on samples of  $C_2AS$  prepared at  $600^\circ C$  and  $1100^\circ C$  are depicted in figures 8 and 9. The profile of the hydration peak of samples  $C_2AS$  and  $C_2S$  calcined at  $600^\circ C$  is shaper than that of samples calcined at  $1100^\circ C$  and  $900^\circ C$ . The influence of temperatures is evidently demonstrated; the higher is the temperature, the higher is the magnitude of hydration reaction. The results indicate that the maximum time of heat evolution at hydration of  $C_2AS$  varies from 1 to 2 h and at  $C_2S$  from 2 to 6 h.

SEM micrographs of  $C_2AS$  (figures 10 and 11) calcined at  $600^\circ C$  show plate crystal of gehlenite hydrate.

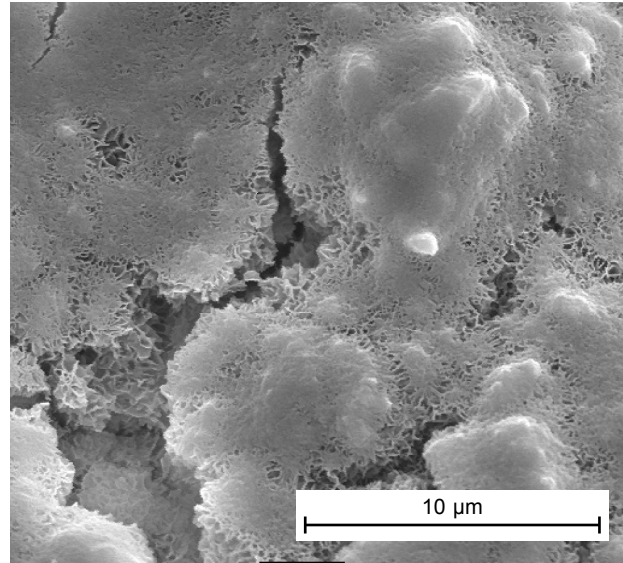


Figure 5. SEM micrograph of nano-crystalline phase of  $C_2S$  calcined at  $600^\circ C$  after 1-day hydration. Layer of C-S-H with honeycomb structure is observed.

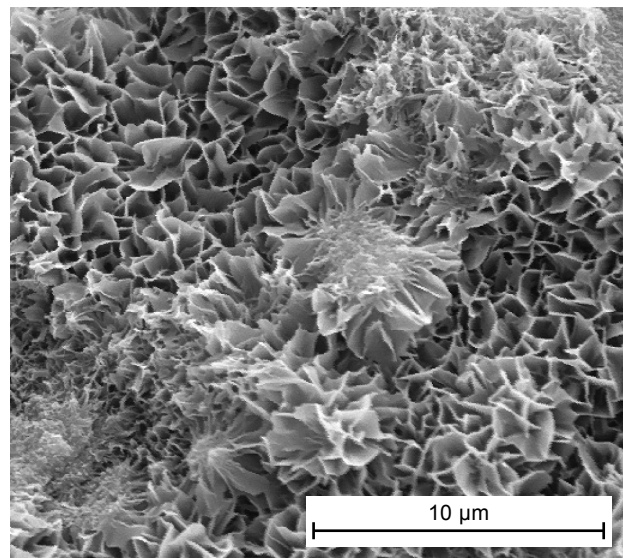


Figure 6. SEM micrograph of nano-crystalline phase of  $C_2S$  calcined at  $600^\circ C$  after 7-day hydration. Crystal structure is developed.

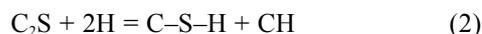
#### Formation of crystallohydrates in $C_2AS-C_2S-C_4A_3\bar{S}-C\bar{S}-C-H$ system

The course of heat evolution during hydration of samples obtaining by homogenizing minerals is described by means of calorimetric curves (figures 12a-f). The measurements were performed at room temperature. It is evident, that the mineralogical composition, as calculated from "gehlenite hydrate/ettringite" ratio, influences the course of hydration. The hydration reaction of samples with higher content of  $C_2S$  and  $C_2AS$  prepared via sol-gel process occurs in two phases sepa-

rated by induction period. With increasing expected ettringite, reaction occurs in one phase. The formation of ettringite in the presence of  $\text{Ca}(\text{OH})_2$  is achieved within two hours.

Figure 13 presents X-ray diffraction analyses of samples hydrated for 7 days. The XRD patterns show that the main hydration product in samples 1, 2 and 3 is gehlenite hydrate which is formed by primary and sec-

ondary reaction (reaction (4)). The primary hydration product of  $\text{C}_2\text{S}$  are C-S-H gel and  $\text{Ca}(\text{OH})_2$ . Later on the crystallization of gels leads to the formation of tobermorite or other calcium silicate hydrates.



The formation of gehlenite hydrate can be also represented by two reactions. Firstly, gehlenite hydrate can be formed by hydration reaction of  $\text{C}_2\text{AS}$  xerogel according to (reaction (3))



or as secondary reaction between calcium silicate hydrogel, calcium hydroxide and gibbsite.



Sample 4 is a specific sample without nano particles of gehlenite. Nevertheless, one can observe on XRD patterns that ettringite coexists with gehlenite hydrate. In this sample gehlenite hydrate was formed through secondary reactions between CSH, CH (calcium hydroxide) and  $\text{AH}_3$  (gibbsite) (reaction (4)). Consequential chemical equation in sample 4 which corresponding to singular point S1 (figure 1) can be written:



In samples 5 and 6 ettringite is the dominant phase. The identification of gehlenite hydrate by XRD was hindered due to very intense peaks of ettringite. Ettringite is there formed according to the following the reaction:

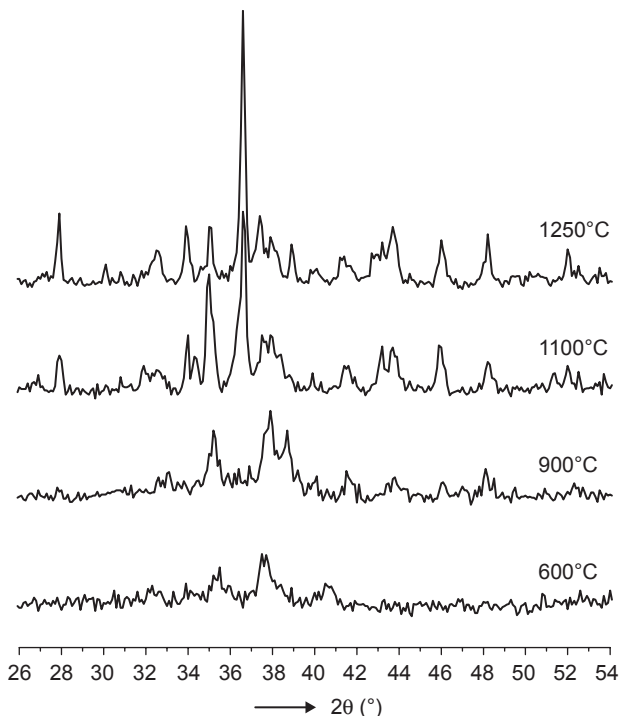


Figure 7. XRD diffraction patterns of  $\text{C}_2\text{AS}$  xerogels calcined at different temperatures.

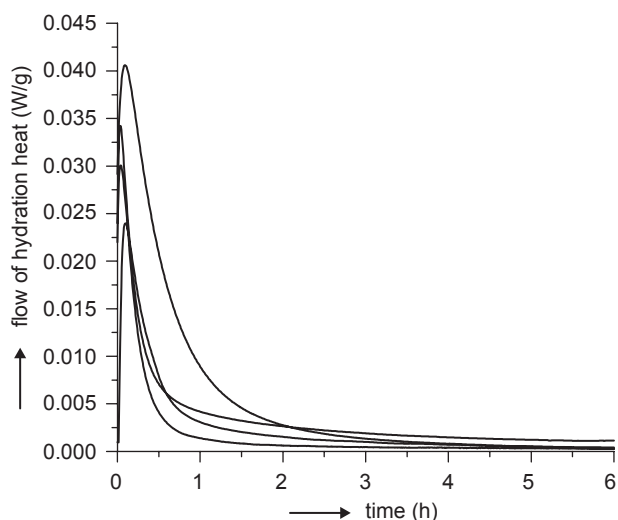


Figure 8. Calorimetric curves of nano-crystalline  $\text{C}_2\text{AS}$  calcined at  $600^\circ\text{C}$ ;  $w/c = 0.5$ .

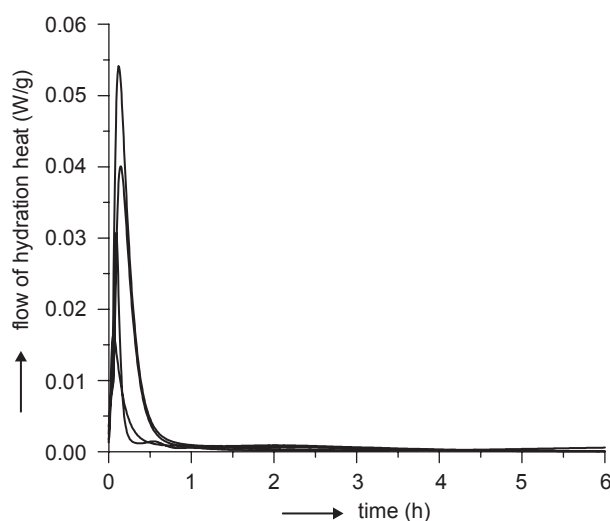


Figure 9. Calorimetric curves of nano-crystalline  $\text{C}_2\text{AS}$  calcined at  $1100^\circ\text{C}$ ;  $w/c = 0.5$

Figure 14 presents SEM micrographs of samples after 7 days of hydration. The hydration was kept in suspension, allowing thus to accelerate process of reaction. Large tabular crystals of gehlenite are observed in samples 1, 2, 3. Here, gehlenite hydrate is dominating phase (figure 7). At singular point, two distinct hydrated products can be observed: tabular shape supplemented by large and elongated crystal hydrates. These last ones are attributed to ettringite. The similar microstructure can be observed in micrographs of samples 5 and 6. In all these samples, ettringite is stable and gehlenite hydrate is formed at lower temperature. The formation of gehlenite hydrate by primary or secondary reaction is due to the high hydraulic activity of  $C_2S$  and  $C_2AS$  synthesized by sol-gel method.

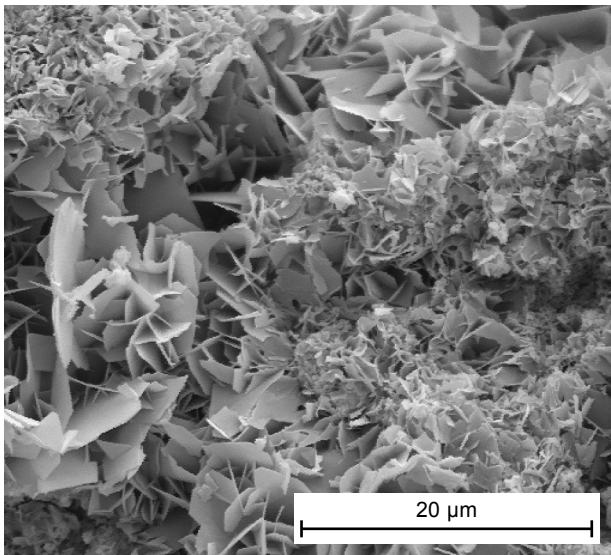


Figure 10. SEM micrograph of  $C_2AS$  calcined at  $600^\circ C$  after 1-day hydration.

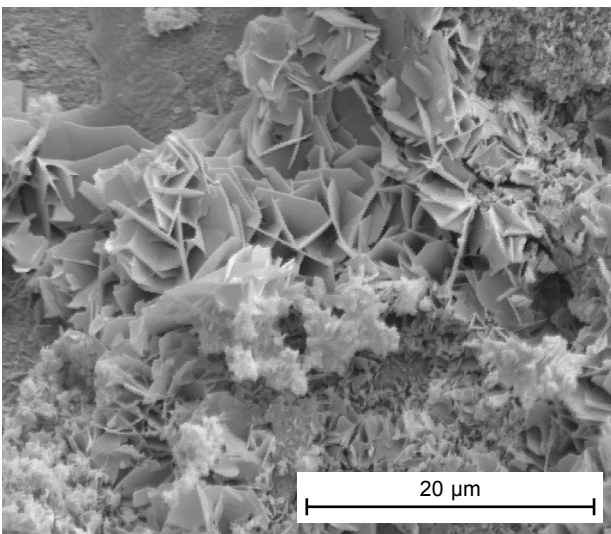
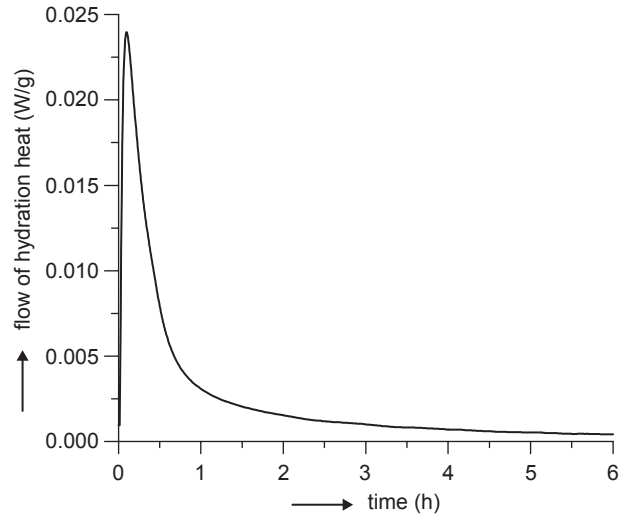
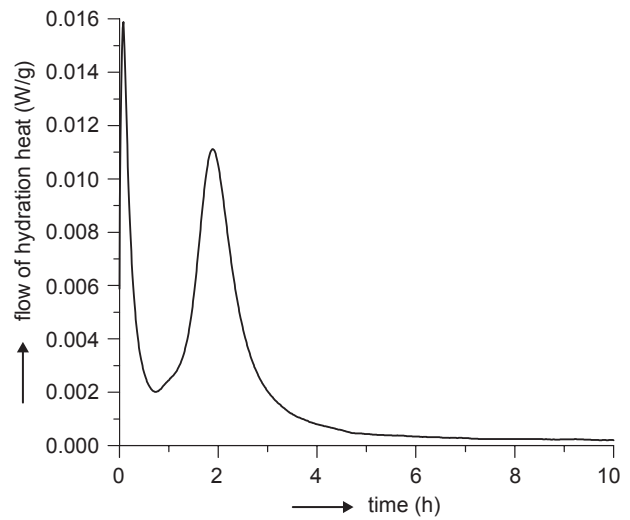


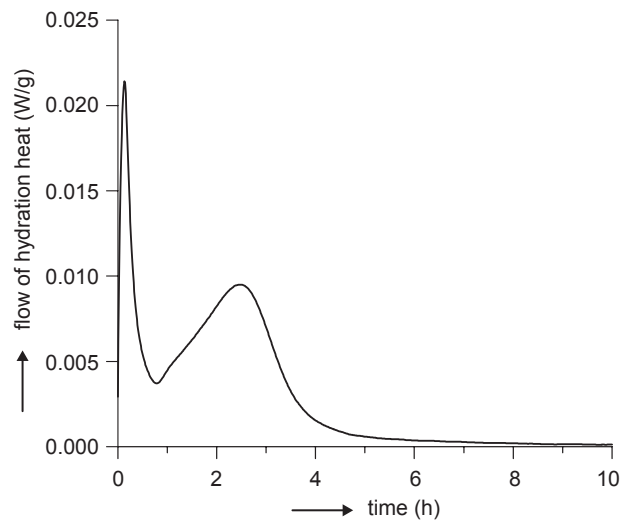
Figure 11. SEM micrograph of  $C_2AS$  calcined at  $600^\circ C$  after 7-day hydration.



Sample 1

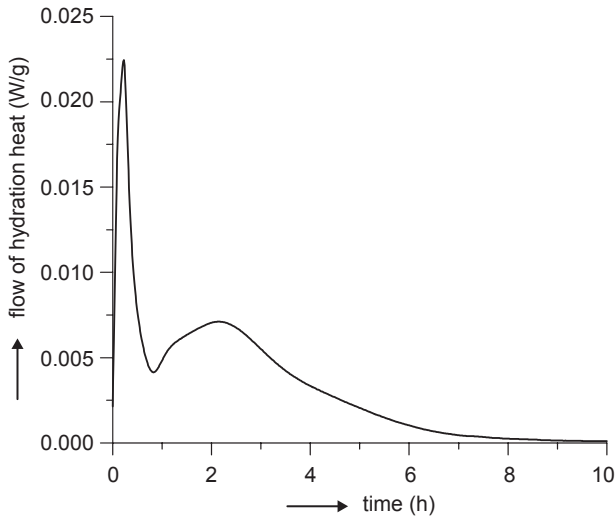


Sample 2

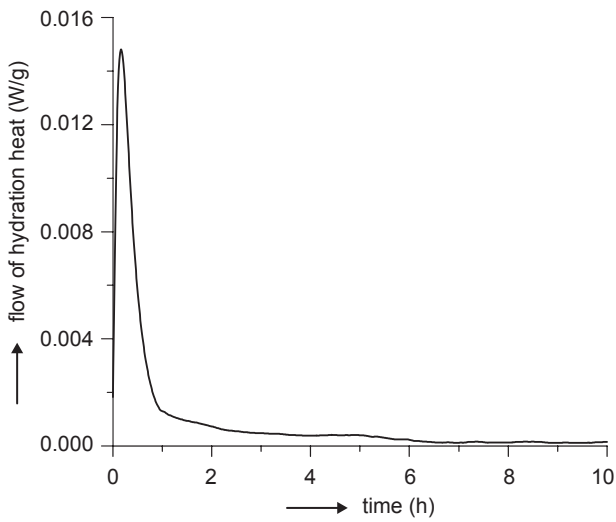


Sample 3

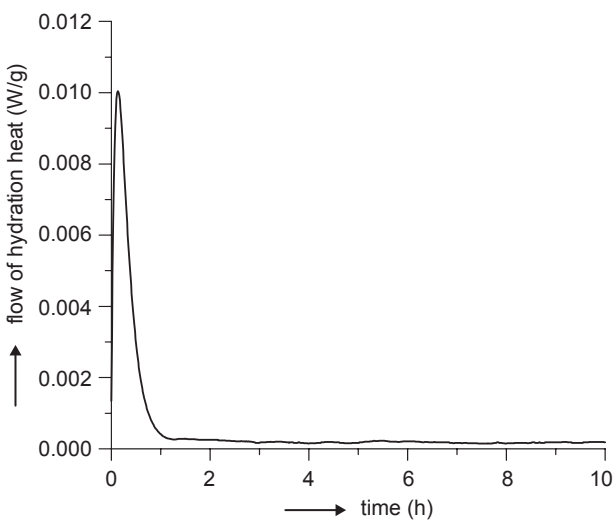
Figure 12. Calorimetric curves.



Sample 4



Sample 5



Sample 6

Figure 12. Calorimetric curves (continue)

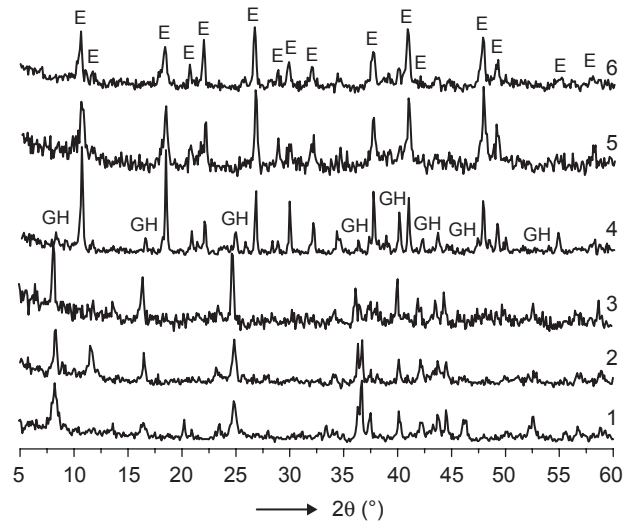
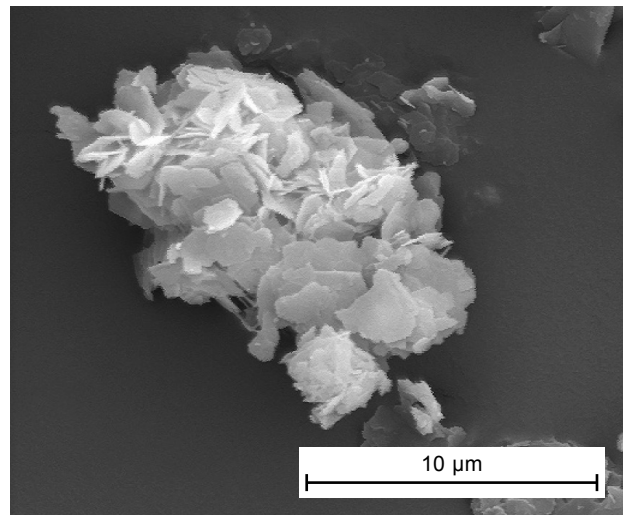
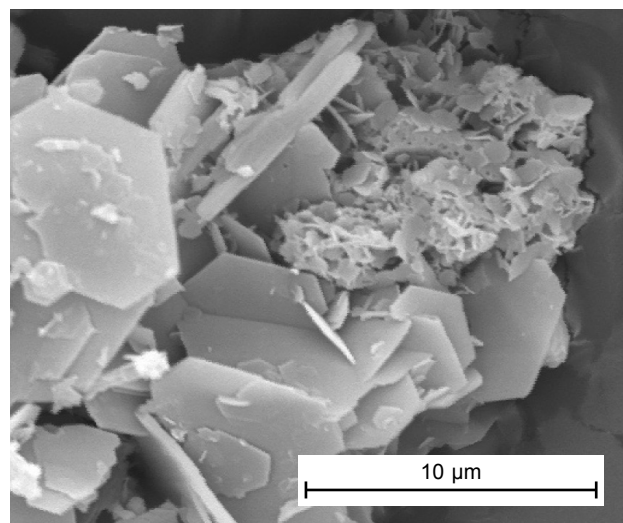


Figure 13. XRD diffraction patterns of samples after 7 days of hydration at 25°C. E- ettringite, GH - gehlenitehydrate

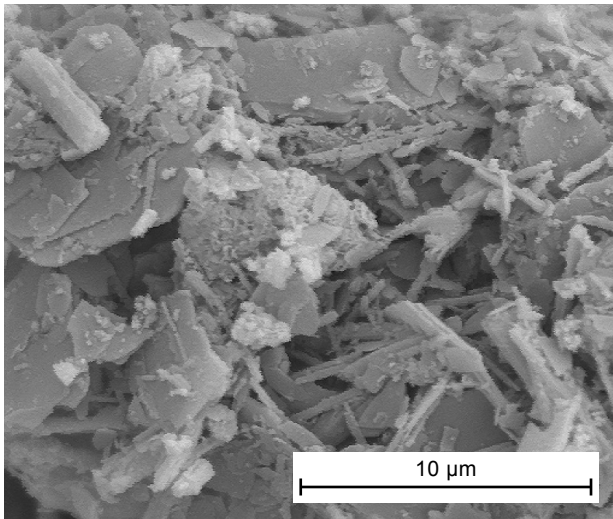


Sample 1

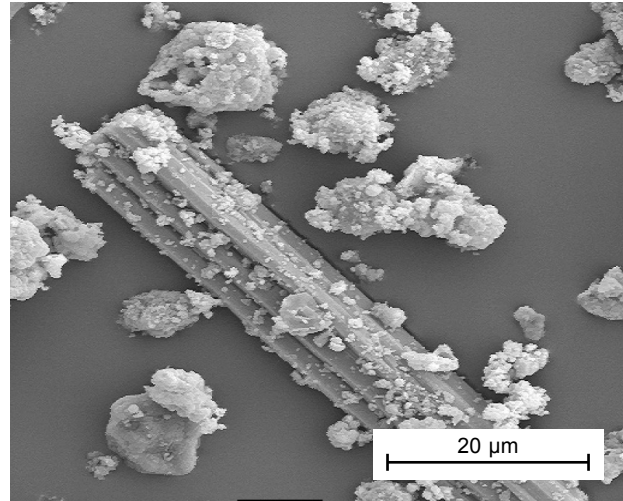


Sample 2

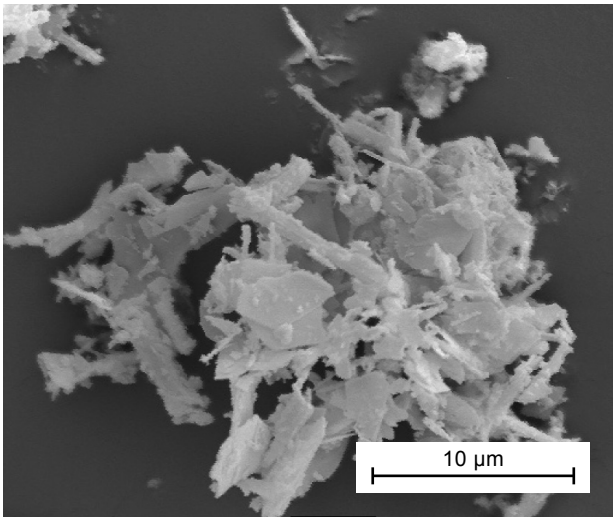
Figure 13. SEM micrographs.



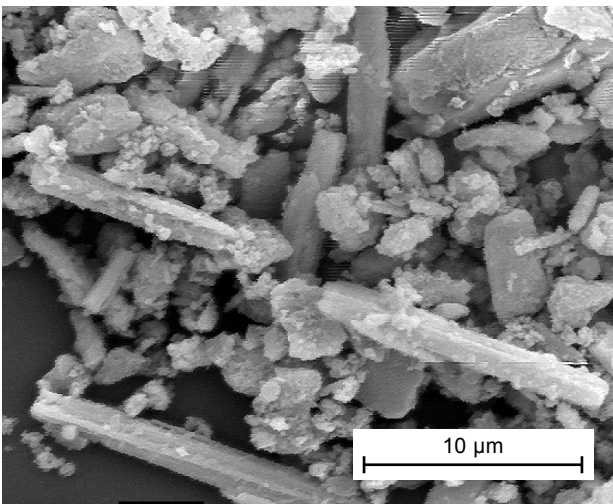
Sample 3



Sample 6



Sample 4



Sample 5

Figure 13. SEM micrographs.

## CONCLUSION

This work has explored an alternative method (sol-gel processing) to synthesize pure and highly active cement phases, which prepared by traditional route have low or latent hydraulicity. The xerogels of  $C_2S$  and  $C_2AS$  have shown good hydraulicity. For the first time, sol-gel process has been applied to obtain gehlenite hydrate from gehlenite hydration. Binding materials in the framework of  $C_2AS-C_2S-C_4A_3\bar{S}-C\bar{S}-C$  system, that can be considered as belonging to the class of Sulfoaluminate Belite Cements (SAB) with nano particles of  $C_2AS$  and  $C_2S$  prepared by sol-gel method, showed better hydraulic activity comparatively to the system which consist of pure minerals. The forecasted hydration products ettringite and gehlenite hydrate were identified. The hydration leading to coexistence of two crystalline hydrates of gehlenite hydrate and ettringite has been achieved by primary and secondary reactions.

## Acknowledgement

*The authors are grateful to Slovak grant VEGA 1/3574/06 for financial support of this work.*

## References

1. Georgescu M., Lepetich J.: *IBAUSIL 14*, Weimar 2000, vol.I, p.I-0395-0403
2. Komljenovic M. M., Zivanovic B. M., Rosic A.: 10<sup>th</sup> ICCG Goteborg 1977, vol.I, p.017
3. Brinker C. J., Scherer G. W.: *Sol-Gel Science*, Acad. Press, New York, 1989.
4. Schmidt H.: *Materials Science Forum* 34, 833 (1988).
5. Sugita K.: *Advanced Materials* 4, 582, (1992).

6. Chatterjie A. K.: *Cem.Concr.Res.* 26, 1227, (1996).
7. Jiang W., Roy D. M.: *Ceram.Bul.* 71, 642, (1992).
8. Palou M. T., Majling J.: *Ceramics-Silikáty* 39, 63 (1995).
9. Majling J., Sahu S., Vlna M., Roy M. D.: *Cem.Concr. Res.* 23, 1351 (1993).
10. Majling J., Jesenák V., Roy M. D., Roy R.: *J. Mater. Res.* 4, 447 (1989).
11. Palou M., Majling J.: *Proc., Book of Abstracts*, p.87, Brno 1999.
12. Gao-Chao Lai, Takuo Nojiri, Kin-ichi Nakano: *Cem. Cochr.* 22, 743 (1992).
13. Feng Xiuji, L. Shizong: *Cem.Concr.Res.* 16, 587 (1986).
14. Chromý S.: *Zement-Kal-Gips* 23, 382 (1970).
15. HEWLETT P.C.: *Lea's Chemistry of cement and concrete*, 4<sup>th</sup> ed., St. Edmunsbury Press, London 1998.
16. El-Didamony H., Khalil K. A., El-Attar M. S.: *Cem. Concr.Res.* 30, 7 (2000).
17. El-Diamond H., Khalil K. A. and El-Atter M. S.: *Cem. Concr.Res.* 30, 7 (2000).
18. Locher F. W., *Proc. 4<sup>th</sup> Int. Symp. on chemistry of cem.* 44, 267 (1960).
19. Quillin K. C., Majumdar A. J.: *Adv. in Cem.Res.* 6, 47 (1994).
20. Palou M. T., Majling J., Dováľ M., Kozánková J., Mojumdar S.: *Ceramics-Silikáty* 49, 275 (2005).
21. Roy D. M., Oyefesobi S. O.: *J.Am.Ceram.Soc.* 60, 178 (1977).
22. Dováľ M., Palou M. T., Kovár V.: *Ceramics-Silikáty* 49, 104 (2005).
23. Palou M., Dováľ M.: 2<sup>nd</sup> Inter. Symp. Non-traditional Cement and Concrete, p.261-268, Ed. Bílek and Keršner, Brno 2005.

---

HYDRATÁCIA A MIKROŠTRUKTÚRA SPOJÍV  
OBSAHUJÚCICH C<sub>2</sub>AS A C<sub>2</sub>S SYNTETIZOVANÝCH  
SÓL-GÉL METÓDOU

MARTIN DOVÁĽ, MARTIN PALOU, VLADIMÍR KOVÁR

*Fakulta chemickej a potravinárskej technológie,  
Slovenská technická univerzita,*

*Radlinského 9, 812 37 Bratislava, Slovenská Republika.*

Sól-gél metóda bola použitá na syntézu nanočastíc C<sub>2</sub>AS a C<sub>2</sub>S. Tieto cementové fázy pripravené reakciou v tuhej fáze pri vysokých teplotách sú hydraulicky latentné alebo menej aktívne. Po kalcinácii pri 600°C boli jednotlivé vzorky C<sub>2</sub>S a C<sub>2</sub>AS tepelne spracované pri 900°C resp. 1100°C. V modelovom systéme C<sub>2</sub>AS-C<sub>2</sub>S-C<sub>4</sub>A<sub>3</sub>S-CŠ-C boli použité fázy C<sub>2</sub>S a C<sub>2</sub>AS pripravené sól-gél metódou. Výsledky u týchto vzoriek ukázali lepšie hydraulické vlastnosti ako to bolo u systému kde boli použité čisté minerály. Hydratácia tohto systému vedie ku koexistencii dvoch rovnovážnych kryštallohydrátov gehlenit-hydrátu a ettringitu, ktoré vznikli primárnou aj sekundárnou reakciou. Obidva kryštallohydráty gehlenit-hydrát a ettringit boli stabilné.

# CEMENT HYDRATION IN THE PRESENCE OF WOOD EXTRACTIVES AND POZZOLAN MINERAL ADDITIVES

GIEDRIUS VAICKELIONIS, RITA VAICKELIONIENE

*Faculty of Chemical Technology, Kaunas University of Technology  
Radvilenu str. 19, 50254 Kaunas, Lithuania*

E-mail: gievaic@ktu.lt

Submitted February 4, 2005; accepted March 30, 2006

**Keywords:** Wood extract, Cement paste, Opoca, Pozzolanic activity, Specific surface area, Adsorption

*In this work, the ability to reduce the harmful influence of wood extractives using the pozzolanic mineral additive, carbonated opoca, was investigated. The influence of various wood species extracts on the setting time and the hardening of two types of Portland cement, CEM I 42.5 R and CEM II/A-L 32.5, was searched. It has been found that cement hydration, setting and hardening depend upon wood extract concentration and do not depend on wood species and preparation method. The influence of extractive additives on binding material (pure cement and cement with opoca additive) was estimated according to the setting time of binding material paste, active portion of the reaction products of cement hydration changes, cement stone strength and X-ray diffraction of hardened cement stone. The investigation data show that wood extractives decrease the hydration of cement and pozzolanic additives effectively minimize this influence. The expediency of employing mineral additives (opoca) with a large specific surface was confirmed and that opoca surface was found to influence the binding rate of CaO. The opoca specific surface influences its pozzolanic activity and adsorption ability. At the initial stages of cement hardening the strongest influence of the particle fineness of opoca additive was observed on its adsorption properties. At later stages of hardening the influence of opoca additive particle fineness on its pozzolanic properties (binding of separating Ca(OH)<sub>2</sub>) increased.*

## INTRODUCTION

Building products, such as cement-bonded particle-board (CBP), wood wool cement board (WWCB), cement bonded fibreboard, etc., made from mineral-binding materials and wood aggregates are widely applied in many developed countries. Chittenden [1] divides mineral-bonded wood composites into two distinct groups: (1) composites in which wood is incorporated as an aggregate in the mineral matrix (as fibres, sawdust, shavings or particles) and (2) composites in which the cement (or other mineral binder) acts purely as a binder, such as wood wool cement board or flake board. Mineral-bonded wood or other lignocellulosic composites are moulded or compressed blocks and panels containing approximately 30-70 % by weight of wood in various forms and 70-30 % of mineral binder [2]. Specially prepared wood aggregates with particular dimensions and varying in treatment are used for their production. Fibreboard is manufactured using wood strips 300-500 mm in length and 0.1-0.8 mm wide. Wood-Fibre Cement Blocks contain about 80 % of wood fibre, which has been specially treated to make them immune to rot or insect damage. The treatment also prevents sugars and tannins in the wood from reacting with the cement, which would interfere with proper

curing. The wood particles (thickness 0.3-5 mm, length 25-30 mm, width 1.6-4.8 mm) used in the manufacture of the block may be partially or fully comprised of post-industrial softwood, which is then mineralized with cement. In CBP, specially graded raw wood shavings and chips (length 3-30 mm) also are used; they are neutralized and mineralized, then bonded together with Portland cement.

Preparing concrete mixtures with fine sawdust requires big amounts of water. This water dissolves the extractive materials that retard the hardening of Portland cement. Besides, using sawdust, the input of cement increases in comparison with analogous materials in whose production specifically prepared wood filling material is used.

In comparison with specifically prepared wood aggregates, wood sawdust is practically not used.

Wood is chemically heterogeneous and its components can be divided into two groups: structural components of high molecular weight - natural polymer substances (cellulose, hemicelluloses and lignin), which are the major cell wall components; and non-structural components of low molecular weight (extractives and inorganic components). The content of polymer substances: cellulose 40-42 %, lignin 26-28 %, hemicelluloses 29-34 % and extractives 5-10 %.

Cellulose is insoluble in water, organic solvents and alkaline solution. It does not mediate under the influence of these materials.

Lignin is the most complex polymer among naturally occurring high molecular weight materials. It does not disintegrate under the influence of various organic solvents, alkaline solutions and water.

Hemicelluloses differ from cellulose by containing various sugar units with much shorter chains. It is a group of different polymers made up of 5 and 6 carbon sugars. They are soluble in alkali and some hardwood polyoses are even soluble in water. Disintegration of hemicelluloses to the constituents in the alkaline solution increases the amount of extractives. Hemicelluloses are more reactive than cellulose.

The extractives are non-polymeric (except pectins and condensed tannins) and may be separated from the insoluble cell wall materials by solving them in water or organic solvents.

The presence of extractives results in corrosion of metals in contact with wood, inhibition of setting of concrete, glue, and finishes, etc. [3].

Cement is an alkaline inorganic composite containing a surface hydroxyl group [4]. Wood, in general, inhibits the setting of cement with hardwood fibres, being the most inhibitory. It has been determined that heartwood is also highly inhibitory in the curing of cement [5]. Wood extractives were found to adversely affect the exothermic hydration characteristics of Portland cement, which in turn affects the wood cement compatibility [6].

The main inhibitor of cement hydration are wood fibre soluble sugars and part of hemicellulose, which under certain conditions can be resolved in these sugars [7, 8, 9]. It has also been found that along with sugars, starches and tannins can inhibit cement setting. Other extractives that cause problems in cement wood compatibility are resins and fatty acids, terpenes and terpenoids, simple sugars and salts [5]. Sugars in concentration as low as 0.03-0.15 wt. % in cement retard the setting time and affect the strength of the cement [10].

The main saccharides of different wood species are glucose and galactose, arabinose and xylose with mannose. The composition of alkali extracts is similar to that of water extracts [11]. The extraction temperature does not influence the extract qualitative composition. Other soluble materials have an insignificant influence on the hydration of cement.

The concentration of soluble wood materials in an extract depends on extraction time and temperature [10, 11]. A longer extraction time and a higher temperature (up to 100°C) afford a higher concentration of soluble materials.

The alkali medium of cement paste stimulates extract exudation [10, 11]. Pozzolanic material added to

the cement stimulates combination of free  $\text{Ca}(\text{OH})_2$  and active silica giving water-insoluble silicate hydrates, thus the amount of free  $\text{Ca}(\text{OH})_2$  and, herewith, the pH of the system decrease [12].

Set-retardation may be primarily due to retarding of the hydration of tricalcium silicate through the adsorption of organic admixtures onto calcium hydroxide. Adsorption onto the initial hydration products of tricalcium aluminate can also retard the further hydration [13]. The inhibition of cement hydration occurs when the calcium silicate hydrate nucleation sites on the originally positively charged surfaces are poisoned by sugar-acid anions [8, 14].

Our investigations [8, 15, 16] have resulted in the hypothesis that wood sugars are surface-activating hydrophilic material. Added to the cement mix together with hardening water, under the influence of adsorption ability and cohesion of molecules, sugars form a thin adsorption layer on the surface of cement grains. Small parts of cement cannot aggregate, and grains of cement become out of the reach of water. Thus, migration of hydration products becomes the impossible and hydration of cement slows down.

Mineral additives added to a mixture of concrete and wood fibre improve its quality [17, 18]. The influence of these materials isn't sufficiently investigated and their application is low.

The present work aimed to study the effect of the wood extractives on the setting properties of cement and the influence of the opoca on the process.

## EXPERIMENTAL

The materials used in this investigation were Portland Cement CEM I 42.5R, Portland Cement CEM II/A-L 32.5 and ground opoca. Pozzolana contains approximately 38 % of calcium carbonate, therefore it is called carbonated opoca. The calcite is evenly distributed in opal in the form of dispersal parties and rests of microorganisms. Quartz is in the form of very fine particles. The chemical and mineralogical composition and the specific surface area (Blaine) of the starting materials are shown in table 1.

Wood extracts were made from fresh sawdust of various wood species (fir, alder, asp, hornbeam and birch). The sawdust was poured over with water (water extracts) and with cement suspension (alkali extracts). For the estimation of the amount of soluble products of cement hydration, in parallel with the above-mentioned mixes in the same conditions cement suspension without sawdust was prepared. Tightly closed flasks with the mixture were kept for 24 hours at a temperature of 80°C and mixed up from time to time. Later the extracts were separated by vacuum filtration.

Table 1. Chemical and mineralogical composition and specific surface area (Blaine) of starting materials.

Specifications	CEM I 42.5 R	CEM II/A-L 32.5	Carbonate opoca
1. Chemical composition (wt.%)			
SiO <sub>2</sub>	20.37	18.63	55.83
Al <sub>2</sub> O <sub>3</sub>	5.04	5.41	2.31
Fe <sub>2</sub> O <sub>3</sub>	2.82	2.90	1.07
CaO	63.90	62.42	21.06
MgO	1.99	3.20	0.49
R <sub>2</sub> O	1.44	0.89	0.52
SO <sub>3</sub>	2.73	2.86	0.58
LOI	1.71	3.68	18.18
2. Mineralogical composition (wt.%)			
C <sub>3</sub> S	58.87	52.75	Opal ~ 46
C <sub>2</sub> S	14.62	13.73	Calcite ~ 38
C <sub>3</sub> A	8.60	9.41	Quartz ~ 7
C <sub>4</sub> AF	8.56	8.68	Chalcedony ~ 3
Cc	-	6.00	Glauconite ~ 0.7
C $\bar{S}$ H <sub>2</sub>	4.50	4.50	Muscovite ~ 0.6
3. Specific surface (m <sup>2</sup> /kg)			
	420	350	1100

To evaluating the amount of extracted materials in extracts, they were evaporated in a water bath and the residues were dried at a temperature of  $80 \pm 5^\circ\text{C}$ . The amount of soluble products of cement hydration formed in alkali extracts was subtracted. The calculated difference between the obtained data on the sawdust cement water system and cement water system extraction showed the amount of wood extractive. 25 wt.% of cement were used to maintain the alkali medium in the system.

The cement pastes and cement-opoca pastes were prepared using the standard water and wood extracts. The monitoring of consistency and setting time were directly carried out using a Vicat apparatus.

The fresh pastes were moulded in 2 cm steel cubes. One part of them were kept in a 90 % relative humidity (R.H.) at  $20^\circ\text{C}$  for 24 h, and the others were steamed in a 100 % R.H. at  $80^\circ\text{C}$  for 8 h. Then all specimens were remoulded and kept under tap water up to 28 days at  $20^\circ\text{C}$ , then broken.

After the determination of the compressive strength, the hydration of pastes was stopped using a 1:1 mixture of methanol acetone and then the pastes were dried at a temperature of  $100^\circ\text{C}$ . Three samples of cement cubes were measured for each test, and the mean value was considered. The mechanism of hydration was also studied by the classical techniques, namely, chemically combined water measurements, XRD (X-ray diffraction) and DTA (differential thermal analysis).

The kinetics of hydration was followed by determining the active portion of reaction products of cement hydration by the ignition loss at  $1000^\circ\text{C}$  of the dried paste on an ignited weight basis minus the amount of ignition loss of the anhydrous binding material (in the first case pure cement and in the second case cement with opoca additive).

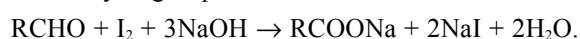
XRD analysis was performed using a DRON-3 diffractometer. The investigation was carried out in the  $2\theta$  range  $10\text{-}60^\circ$  with Ni-filtered, Cu K $\alpha$  radiation.

The DTA analysis was performed using a Du Pont 990 thermal analyzer at a heating rate  $10^\circ\text{C}/\text{min}$  up to  $1000^\circ\text{C}$  with finely powdered alumina as a reference material.

The specific surface area of different fractions of opoca was determined by Blain's method.

The opoca activity was determined according to its capacity to bind Ca(OH)<sub>2</sub> from lime solution. It was expressed as the amount of CaO mg in 1 g of the material.

The concentration of glucose was determined by the method of iodometric adsorption. This method is based on the ability of iodine in an alkali medium to oxidize the aldehydic group of the glucose molecule to the carboxylic group.



## RESULTS AND DISCUSSION

At the first stage of the experiment, fresh sawdust extracts of various wood species were investigated. The sawdust was treated in two different conditions: (1) neutral (water), (2) base (cement suspension). The test results are given in table 2. It was estimated, that alkali solution dissolved 5-10 times as much of wood extractive material as did water. The results of the investigation correspond to the reference data [10,11] and corroborate the great influence of hemicellulose. Under the influence of Ca(OH)<sub>2</sub> hemicellulose disintegrates into soluble sugars. The findings confirmed that the lowest content of soluble materials in fir. Deciduous trees contained much more soluble materials.

Table 2. Data on extracts of various wood species when extraction was carried out for 24 hours at a temperature of 80°C.

Wood's species	Amount of extracted materials from wood (wt.%)	
	10 g of sawdust and 10 ml of water	10 g of sawdust, 2.5 g of cement and 10 ml of water
The fir	1.202	5.087
The alder	0.904	6.576
The asp	1.326	7.433
The hornbeam	1.215	8.407
The birch	1.313	10.586

The investigation has confirmed that water-soluble wood sugars slow down the hardening and hydration of cement, and this harmful influence can be decreased using pozzolanic mineral additives (e.g., opoca). The mechanism of retardation of cement hydration with sugars has been only partly clarified.

The effects of wood extracts on the setting time of binding material were elucidated by investigating mixes of water extracts of wood species with cement CEM I 42.5R and binding material, which were prepared from equal parts of this cement and ground opoca (table 3). Different amounts of water-soluble materials in various species of wood had a different influence on the *setting time of cement paste* (table 3). Increasing the amount of the additive increased the extent of retardation. Using a

rapid-hardening cement, a low small concentration of water-soluble materials of various wood species resulted in the same hydration as in the control samples. Low concentrations resulted in similar amounts of new formations in various mixtures, thus, it was impossible to observe them in X-ray phase analysis.

To reveal the influence of soluble wood materials on the hardening of cement, more coarse-grained cement CEM II/A-L 32.5 with a lower hardening rate and a binding material made from equal portions of this cement and ground opoca were mixed with wood alkali extracts whose concentrations were respectively 1.604 % and 1.943 %. Then they were kept in the isothermal conditions for 4 h, steamed at a temperature of 80°C, hardened in natural conditions up to 28 days and immediately treated. The data were compared with the data on control samples prepared with water. The results are presented in table 4. The influence of soluble wood materials was the same on both kinds of cement, CEM I 42.5R and CEM II/A-L 32.5, when they harden as a pure binding material and with an opoca additive.

The active portion of the reaction products of cement hydration determines the degree of cement hydration. Extract additives in both classes of cement (without opoca) decrease the active portion of the reaction products of cement hydration in cement stone with respect to control samples. Hardening of cement in natural conditions only slightly decreased the active por-

Table 3. Influence of wood extractive additives on the setting time of cement CEM I 42.5R and binding material (50 wt.% of cement CEM I 42.5R + 50 wt.% of opoca) pastes.

Extract	Concentration of extract (%)	Amount of additive by weight of cement (%)	Setting time, hour-minute		Amount of additive by weight of binding material (%)	Setting time, hour-minute	
			Initial set	Final set		Initial set	Final set
The water	-	-	5-50	7-35	-	2-20	3-15
The birch	0.155	0.047	5-50	6-45	0.059	2-10	2-50
The alder	0.255	0.077	6-30	10-20	0.097	2-50	3-20
The fir	0.338	0.1025	8-05	9-25	0.129	2-20	3-40
The hornbeam	0.341	0.103	7-35	9-30	0.130	2-35	3-55
The asp	0.392	0.119	8-05	11-10	0.149	2-30	3-40
Concentrate	0.738	0.223	9-20	12-40	0.281	3-05	4-15

Table 4. Influence of wood extractive additives on the setting time, compressive strength and active portion of reaction products of cement hydration of steamed and later for 28 days cured cement CEM II/A-L 32.5 and binding material (50 wt.% of cement CEM II/A-L 32.5 + 50 wt.% of opoca) pastes.

Extract	Concentration of extract (%)	Amount of additive by weight of binding material (%)	Setting time, hour-minute		Compressive strength, (MPa) /Amount of active portion of the reaction products (%)	
			Initial set	Final set	After steaming	After 28 days
Binding material - cement CEM II/A-L 32.5. The water/cement ratio of all samples - 0.235						
Water	-	-	3-45	4-45	60.08/10.15	78.58/11.68
Extract 1	1.604	0.377	5-30	6-20	49.75/9.92	52.92/11.27
Extract 2	1.943	0.457	13-20	16-40	17.42/6.69	43.17/9.78
Binding material - 50 wt.% of cement CEM II/A-L 32.5 + 50 wt.% of opoca. The water/cement ratio of all samples - 0.37						
Water	-	-	1-55	2-35	30.88/6.67	34.60/10.21
Extract 1	1.604	0.593	2-35	3-05	29.46/6.61	33.67/9.95
Extract 2	1.943	0.719	3-10	3-50	31.34/6.76	35.10/10.50

tion of reaction products. The general, in the initial period of hardening (up to 3 days) it was more distinct. Steaming of reduced activity cement CEM II/A-L 32.5 with the addition of more concentrated wood extract afforded a more significant decrease of the active portion of reaction products in cement stone in comparison with control stone. After 28 days of hardening in natural conditions this difference decreased.

When the binding material of cement with opoca additive was steamed, there was a similar amount of the active portion of reaction products of cement hydration in the composition of cement stone with soluble wood materials in all cases with respect to control samples (table 4).

When cement without opoca additive was steamed, water-soluble wood materials retarded the hydration of cement. Increasing the concentration of these materials considerably decreased the compressive strength of steamed cement stone. Wood extractive additives (0.457 wt.% of cement) decreased the compressive strength 3.45 times with respect to control samples. The subsequent 28-day hardening of samples in natural conditions reduced this difference to 1.82 times.

Even high concentrations of extracts added to the paste of binding material formed from 50 % of cement CEM II/A-L 32.5 and 50 % of opoca made the compressive strength of steamed samples the same or bigger than the strength of control samples. In this case, the addition of opoca absolutely abolished the harmful effects of water-soluble wood materials on cement hydration.

Referring to our study, we assumed that inserted to the cement systems with hardening water, sugar molecules keep around the cement grain and form an adsorption layer. Therefore, under the action of molecular forces cement grains lose the possibility to cohere and coagulate. The water cannot reach the grains of cement because of this layer. The formation of such layer is described in the references [8,13]. The negative influence of water-soluble wood materials on cement hydration is explained by adsorption.

The addition of pozzolanic mineral materials (e.g., opoca) to cement mixtures decreases the influence of wood extractives. Because the specific surface of these additives is much bigger than of cement and the sorption ability of these materials is higher, the adsorption of water-soluble wood materials first of all takes place on the surface of pozzolanic materials and the concentration of extracts decreases. By the way, more water is required for the preparation of mixtures of cement and pozzolanic additives. Therefore, water easily gets to cement grains and facilitates the hydration.

The distinct peaks of minerals of hydrated clinker on the X-ray diffraction patterns of steamed samples of cement stone, which was made with more concentrated extracts (0.457 wt.% of cement) showed a low degree of cement hydration (figure 1).

The X-ray diffraction patterns of non-hydrated cement samples (figure 1, curve 3) and the same steamed cement prepared with wood extract (figure 1, curve 2), were carried out. Intensive  $\beta$ - $C_2S$  and  $C_3S$  peaks showed that there were many non-hydrated minerals in clinker in the cement stone.

On the X-ray diffraction patterns of steamed cement mixed with distilled water (figure 1, curve 1) distinct peaks characteristic of the main cement hydration product  $Ca(OH)_2$  were seen. The characteristic peaks of  $CaCO_3$  were identified too. The above-mentioned peaks of hydrated clinker minerals were not intensive, implying that cement hydration without wood extract additive was considerably more intensive.

X-ray diffraction patterns of samples of steamed binding material with opoca additive mixed with distilled water (figure 2, curve 1) and of samples with wood extracts (figure 2, curve 2) were similar. The most characteristic peaks of non-hydrated cement (figure 2, curve 3) minerals ( $\beta$ - $C_2S$  and  $C_3S$ ) were not intensive, showing a large degree of cement hydration. The distinct peaks of  $CaCO_3$  and quartz predominated in all X-ray phase analysis.

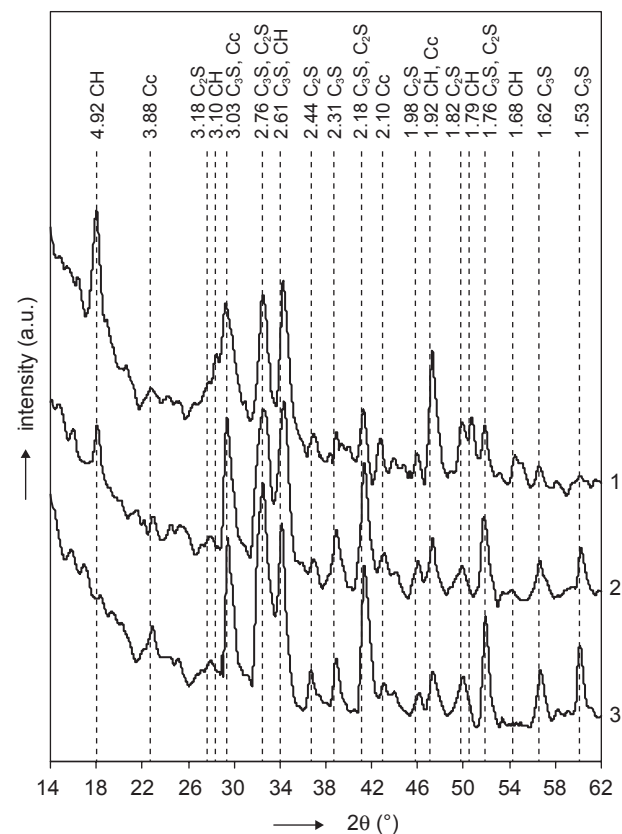


Figure 1. X-ray diffraction patterns of cement CEM II/A-L 32.5.; 1 - mixed with water and steamed; 2 - mixed with extract 2 and steamed; 3 - non-hydrated cement ( $C_3S$  - alite,  $\beta$ - $C_2S$  - bellite,  $C_3A$  - tricalcium aluminate, CH - calcium hydroxide, Cc - calcium carbonate).

Ca(OH)<sub>2</sub> was not identified in the steamed cement with opoca additive, because Ca(OH)<sub>2</sub> reacts with opoca SiO<sub>2</sub> and forms CSH.

Figures 3 and 4 illustrate the DTA thermograms of the same samples. All DTA thermograms of CEM II/A-L 32.5 Portland cement (figure 3) show three main endothermic effects. The first and largest effect at a temperature of 150-200°C is the elimination of hygroscopic water and the dehydration of the obtained hydrosilicates. The second effect at a temperature of 470-490°C shows dehydration of Ca(OH)<sub>2</sub>, and the third endothermic effect at a temperature of 725-740°C is essentially due to decarbonisation of CaCO<sub>3</sub>.

The intensity of the endothermic effect at a temperature of 480°C of steamed Portland cement mixed with alkali wood extractive (0.457 % from Portland cement mass) (figure 3, curve 2) is lower than the intensity of Portland cement mixed with water (figure 3, curve 1). It shows that the addition of wood extractive slows down the hydration of cement. The low endothermic effect at a temperature of 465°C of not hydrated cement (figure 3, curve 3) can be coherent with the dehydration of α-C<sub>2</sub>SH which through the hygroscopicity of Port-

land cement and the humidity of clinker additives (gypsum and limestone) was able to form during the partial hydration of clinker mineral C<sub>3</sub>S.

The degree of Portland cement hydration depends on the concentration of wood extractive. The higher content of extractives decreases the hydration of cement.

The DTA thermograms of binding material prepared of equal amounts of Portland cement CEM II/A-L 32.5 and opoca (figure 4) show two endothermic effects at temperatures of 110-200°C and 785-800°C and one exothermic effect at 855-890°C. The first endothermic effect, exactly as in the case of Portland cement without opoca additive, shows elimination of hygroscopic water and dehydration of hydrosilicates; the second endothermic effect is essentially due to decarbonisation of CaCO<sub>3</sub> of opoca. The endothermic effect of dehydration of Ca(OH)<sub>2</sub> is not displayed, because Ca(OH)<sub>2</sub>, which separates during the hydration when specimens are steaming, reacts with SiO<sub>2</sub> of opoca and forms CSH (I) type hydrosilicates. The exothermic effects at a temperature of 855-875°C confirm the formation of this type of hydrosilicates. This effect is principally related to the conversion of CSH (I) to volastonite. Unhydrated binding material has no CSH (I). The exothermic effect at a temperature of 890°C (figure 4, curve 3) is connected with the formation of volastonite from the CaO (decarbonisation of CaCO<sub>3</sub>) and SiO<sub>2</sub> of opoca.

The DTA thermogram (figure 4, curve 2) of Portland cement with opoca additive and mixed with alkali wood extractive is almost identical to the thermogram (figure 4, curve 1) of binding material mixed with water and steamed. Thus, in both cases Portland cement hydration is almost the same.

The DTA analyses are in good agreement with XRD data. It shows that opoca is an effective additive which decreases the harmful influence of wood extractives on the hydration of Portland cement.

Our study confirmed the expediency of employment of mineral additives (opoca) with a large specific surface. The influence of additive particle fineness on these processes is not yet clear.

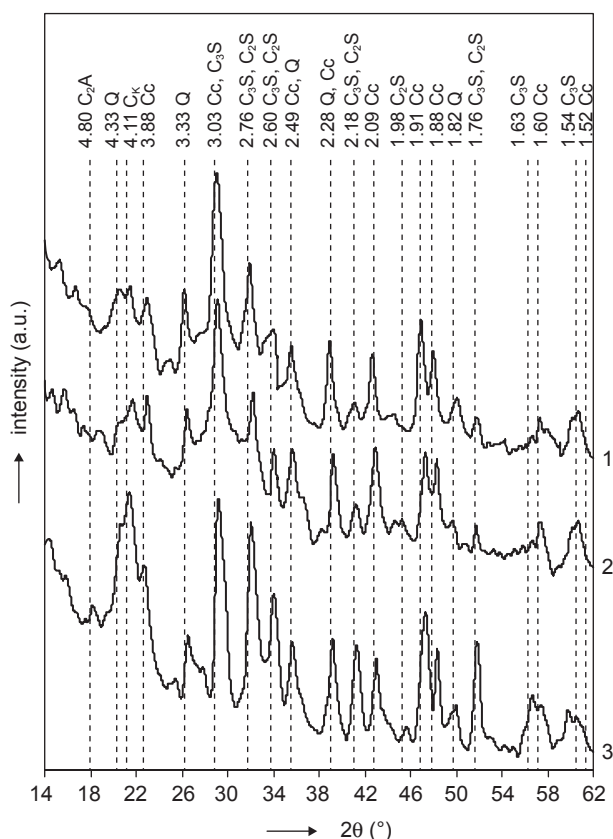


Figure 2. X-ray diffraction patterns of binding material (50 wt. % of cement CEM II/A-L 32.5 + 50 wt. % of opoca). 1 - mixed with water and steamed; 2 - mixed with extract 2 and steamed; 3 - non-hydrated binding material (C<sub>3</sub>S - alite, β-C<sub>2</sub>S - bellite, C<sub>3</sub>A - tricalcium aluminate, Q - quartz, Cc - calcium carbonate, C<sub>R</sub> - cristobalite).

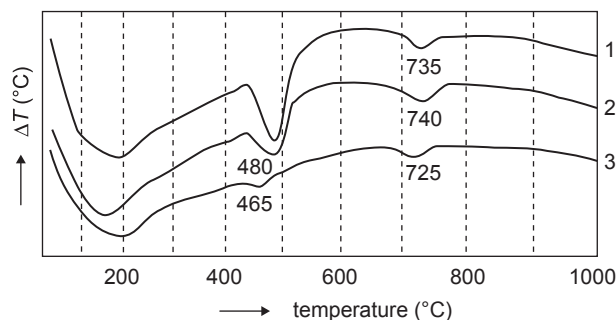


Figure 3. DTA thermograms of cement CEM II/A-L 32.5: 1 - mixed with water and steamed; 2 - mixed with extract 2 and steamed; 3 - non-hydrated cement.

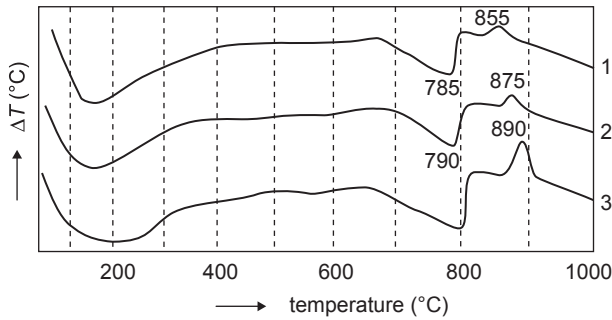


Figure 4. DTA thermograms of binding material (50 wt. % of cement CEM II/A-L 32.5 + 50 wt. % of opoca): 1 - mixed with water and steamed; 2 - mixed with extract 2 and steamed; 3 - non-hydrated binding material.

The aim of the third stage of our work was to determine the influence of the specific surface (the grinding degree) of opoca on CaO binding rate and pozzolanic activity and to investigate the dependence of adsorption ability upon the specific surface.

Five fractions (in mm) of opoca were employed for investigation: I - 0.9–0.63; II - 0.63–0.315; III - 0.315–0.14; IV - 0.14–0.05; V - < 0.05.

Data on the determined conditional specific surface of different fractions of opoca are presented in table 5.

Table 5. Specific surface area of different fractions of opoca.

Fraction (mm)	Specific surface area (m <sup>2</sup> /kg)
0.9-0.63	230
0.63-0.315	340
0.315-0.14	600
0.14-0.05	785
< 0.05	1125

Table 6. Kinetics of CaO binding with opoca of different specific surface area.

Time (days)	Specific surface area (m <sup>2</sup> /kg)				
	1125	785	600	340	230
	Amount of bound CaO (mg/g)				
2	16	15	15	13	12
4	32	30	29	26	24
6	53	49	46	43	40
8	76	69	64	56	53
10	100	93	83	76	67
12	122	112	99	90	74
14	145	128	114	102	84
16	165	147	128	117	95
18	181	164	141	127	103
20	198	175	152	134	110
22	219	190	164	145	121
24	233	200	174	149	125
26	248	212	184	156	130
28	266	229	196	164	138
30	281	241	210	172	144

The influence of opoca specific surface area on the binding rate of CaO was not constant (table 6).

At the initial stage of the experiment (till 8 days) the largest opoca fraction (230 m<sup>2</sup>/kg) bound CaO by 20-25 % less than the smallest (1125 m<sup>2</sup>/kg). Later this difference grew up and after 30 days reached almost 50 %.

At the same time the pozzolanic activity (binding of CaO during a month (15 titration)) of opoca of different specific surface area was investigated (figure 5), because the references refer only to data of samples obtained through a 80 μm sieve. Pozzolanic activity greatly depends on the specific surface area of opoca.

Equation  $y = 15.2 x^{0.41}$  most optimally describes the dependence of pozzolanic activity  $y$  of opoca upon its specific surface area  $x$ .

Different fractions of opoca were poured with a glucose (the main carbohydrate in extracts of different wood species) solution at a concentration of 0.3 % and the dependence of its adsorption ability upon particle fineness was investigated. The mixture in some intervals of time was stirred. After 2 and 24 hours the remaining concentration of glucose was determined by the method of iodometric adsorption. The initial level of

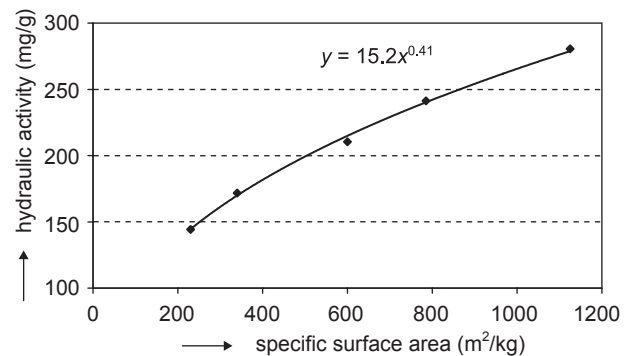


Figure 5. Influence of opoca specific surface on its pozzolanic activity.

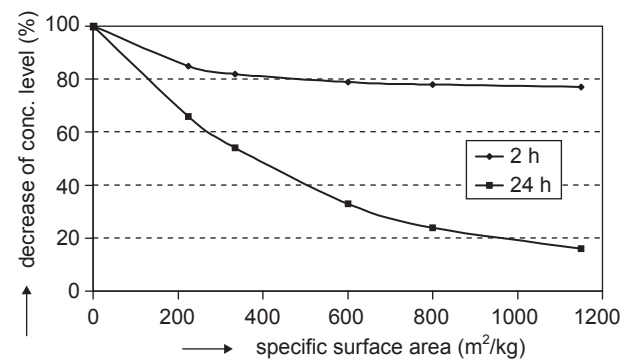


Figure 6. Change of 0.3 % glucose solution concentration after 2 and 24 hours of adsorption with an opoca of different specific surface area.

glucose solution concentration was equated to 100 %. The data on glucose concentration level after 2 and 24 hours of adsorption with an opoca of different specific surface area are presented in figure 6.

The data showed that at the initial stages of hardening of cement sawdust concrete, the biggest influence of particle fineness of the pozzolanic additive was exerted on the additive adsorption properties. Immediately after mixing of sawdust concrete with water, adsorption of separating wood extracts by the opoca began. From time to time a new proportion of extracts was separated, but at the same time its adsorption by the opoca intensified.

At the later stages of hardening, the influence of additive's particle fineness on the binding of separating  $\text{Ca}(\text{OH})_2$  increased. It can be maintained that the higher fineness of the pozzolanic additive was the reason for the higher definitive compressive strength of concrete.

### CONCLUSION

1. An alkali medium dissolves much more wood extractives than water. Under the influence of  $\text{Ca}(\text{OH})_2$  hemicellulose disintegrates into soluble sugars.
2. Sugars retard the hydration of Portland cement.
3. Cement hydration, setting and hardening depend on wood extract concentration and don't depend on wood species and preparation method.
4. Addition of pozzolanic mineral materials, e.g., opoca, to cement mixtures decreases the harmful retarding effect of wood extractives. Because the specific surface of pozzolanic additives is much bigger than of cement and the sorption ability of these materials is higher, adsorption of water-soluble wood materials first of all takes place on the surface of pozzolanic materials and the concentration of extracts decreases.
5. The amount of free lime bound by pozzolanic material is an indication of its pozzolanic activity. This property depends greatly on the specific surface area of pozzolana. The influence of opoca specific surface area on the binding rate of  $\text{CaO}$  varies with time.
6. The most optimal equation to describe the dependence of opoca pozzolanic activity ( $y$ ) on its specific surface area ( $x$ ) is  $y = 15.2x^{0.41}$ .
7. At the initial stages of cement hardening the biggest influence of particle fineness of opoca additive is exerted on its adsorption properties.
8. At later stages of hardening, the influence of opoca additive particle fineness on its pozzolanic properties (binding of separating  $\text{Ca}(\text{OH})_2$ ) increases.

### References

1. Chittenden A. E.: Proceedings 7<sup>th</sup> World Forestry Congress, p. 6128 6134, Buenos Aires, 1972.
2. Simatupang M. H., Schwarz G. H., Broker F. W. : Proceedings 8<sup>th</sup> World Forestry Congress, p. 717 728, Jakarta, 1977.

3. Hon David N.-S., Shiraishi Nobuo: *Wood and cellulosic chemistry*, 2<sup>nd</sup> ed., p. 914, Marcel Dekker, Inc., New York, 2001.
4. Coutts R.S.P., Kightly P.: *J.Mater.Sci.* 19, 3355 (1984).
5. Pehanich J. L., Blankenhorn P. R., Silsbee M. R.: *Cement and Concrete Research* 34, 59 (2004).
6. Hachmi M. H., Moslemi M. A.: *Forest Products Journal* 39, 55 (1989).
7. Zhengtian L., Moslemi A. A.: *Forest Products Journal* 36, 53 (1986).
8. Thomas N. L., Birchall J. D.: *Cement and Concrete Research* 13, 830 (1983).
9. Bilba K., Arsene M-A., Ouensanga A.: *Cement and Concrete Composites* 25, 91 (2003).
10. Janusa M. A., Champagne C. A., Fanguy J. C. et al.: *Microchemical Journal* 65, 255 (2000).
11. Shcherbakov A. S.: PhD. Thesis, Moscow, 1984 (in Russian).
12. Biricik H., Akoz F., Berkday I. I., Tulgar A. N.: *Cement and Concrete Research* 29, 637 (1999).
13. Young J. F.: *Cement and Concrete Research* 2, 415 (1972).
14. Milestone N.B.: *J.Am.Ceram.Soc.* 62, 321 (1979).
15. Nanazashvili I.Ch.: Building materials of wood cement composition, p. 415, Strojizdat, Leningrad 1990 (in Russian).
16. Juenger M. C. G., Jennings H. M.: *Cement and Concrete Research* 32, 393 (2002).
17. Murthy C.: *Inter. J. for Housing Science and its Applications* 9, 313 (1985).
18. Vaickelionis G., Martusevicius M., Vektaris B.: *Chemical Technology* 2, 54 (1997) (in Lithuanian).

### HYDRATAČE CEMENTU ZA PŘÍTOMNOSTI DŘEVNÍCH EXTRAKTŮ A PUCOLÁNOVÝCH MINERÁLNÍCH PŘÍRAD

GIEDRIUS VAICKELIONIS, RITA VAICKELIONIENE

*Faculty of Chemical Technology,  
Kaunas University of Technology  
Radvilenu str. 19, 50254 Kaunas, Litva*

V této práci byla zkoumána schopnost snižování škodlivého vlivu dřevních extraktů za přítomnosti pucolánových minerálních přísad a karbonátové opoky. Byl zkoumán vliv různých druhů dřevních extraktů na dobu a průběh tuhnutí dvou typů portlandského cementu - CEM I 42.5 R a CEM II/A-L 32.5. Bylo zjištěno, že hydratace cementu a jeho tuhnutí závisí na koncentraci dřevního extraktu a nezávisí na druhu dřeva a způsobu jejich přípravy. Vliv extrahovatelných přísad na pojivový materiál (čistý cement a cement s přísadou opoky) byl posuzován podle doby tuhnutí pasty pojivového materiálu, aktivního podílu reakčních produktů při hydratačních změnách cementu, pevnosti cementového kamene a rentgenové difrakce ztuhlého cementového kamene. Výsledky výzkumu ukazují, že dřevní extrakty snižují hydrataci cementu a pucolánové přísady tento vliv účinně zmenšují. Byla potvrzena vhodnost použitých minerálních přísad (opoka) s velkým specifickým povrchem a dále bylo zjištěno, že povrch opoky má vliv na vázání  $\text{CaO}$ . Specifický povrch opoky ovlivňuje jeho pucolánovou aktivitu a adsorpční schopnost. V počátečních fázích tuhnutí cementu byl pozorován nejsilnější vliv zrnitosti částic přísad opoky na její adsorpční vlastnosti. V pozdějších fázích tuhnutí se zvyšoval vliv zrnitosti částic přísad opoky na její pucolánové vlastnosti (vázání vylučovaného  $\text{Ca}(\text{OH})_2$ ).



#### DIMITRIJ LEŽAL - IN MEMORIAM

A few weeks ago, he was enthusiastically solving problems related to three scientific grants and supporting postgraduate students in their work, and now he is no longer with us...

Ing. Dimitrij Ležal D.Sc. was born June 28, 1933, in Prague and stayed loyal to this city his entire life. Since childhood he was an active athlete, playing basketball on a competitive level, and later working as a referee. In 1958, he graduated from the Institute of Chemical Technology in Prague. He started his professional career in ČKD Polovodiče, where he worked as a researcher for ten years, and devoted himself to the preparation of pure substances and the research of materials. In 1965, he defended his postgraduate thesis at the Institute of Chemical Technology in Prague, on the topic "Preparation and characterization of ultra-pure indium arsenide". For the next twelve years, he worked as a researcher in the Institute of Radio Engineering and Electronics of the Academy of Sciences, Czech Republic (ASCR). In 1979 he completed a six-month UNESCO fellowship at the University of California under the leadership of Professor Mackenzie. In 1980 he began working at the then Joint Laboratory of Chemistry and Technology of Silicates, where he initially worked on the preparation of ultra-pure raw materials for light-conducting fibers. He remained at the facility after its transformation to the independent Institute of the Chemistry and Ceramic Materials of Glass. In 1989 he defended his thesis on the purification

and characterization of substances for optics and electronics to obtain a Doctor of Science degree. In 1990 he was elected by the Scientific Board as director of the Institute. He devoted tremendous time and energy to the management of the Institute. Through no fault of his own, the Institute was dissolved as part of the reorganization of the ASCR - a move we now realize was a questionable wise one. Although he was dismayed by the dissolution of the Institute, he did not allow anyone to dampen his enthusiasm for further scientific work and continued to work in the Laboratory of Inorganic Materials on the preparation and characterization of chalcogenide and chalcohalogenide glasses and heavy metal oxide glasses. In recent years, he focused on the preparation of active optic fibers from rare earth-doped glasses, which are used in laser optics and optic fibers. He was a world-renowned expert in this field, as we can see for example from the long-term cooperation with the University of Rennes and other leading experts from Brazil, Germany and Slovakia. Dr. Ležal also dedicated his time to coordinating large-scale cooperation within international projects. For his successful cooperation and coordination of projects, he was granted a medal of honor by the Slovak University of Technology in Trnava. In addition to international projects, Dr. Ležal acted as a researcher in many grant projects supported by national science foundations. He was a prolific publisher, as expected from an expert at such a level. In addition to three monographs, he is the author of more than one hundred publications in important international scientific journals. He gave many lectures at international conferences, some of which were invited lectures. Some of his results can be designated as pioneering, as seen in their practical application. This includes the application of optic fibers in the health industry, especially in laser surgery, procedures for the preparation and purification of substances and glasses used in optoelectronics, as used for example in ČKD Polovodiče and in Tesla Rožnov. His pedagogical activities are also worthy of praise. In addition to training many postgraduate students, he gave lectures for postgraduate courses at the Institute of Chemical Technology in Prague and at the Faculty of Technical and Nuclear Physics, Czech Technical University in Prague. He was a member of the Committee for Lasers and Optic Fibers of the Purkyne Society. Last but not least, he worked as a member of the editorial board and was an important contributor to our journal.

In the last few years, he bravely endured health problems and worked up to the last moment. He passed away unexpectedly following a short hospital admission on February 21, 2006. With the passing of Dr. Ležal, the scientific community has lost an enthusiastic expert, teacher, colleague and good individual loyal to his country.

## NOTES FOR CONTRIBUTORS

### SCOPE OF THE JOURNAL

Ceramics-Silikáty accepts manuscripts dealing with chemistry and physics of ceramics, glass, and other modern inorganic and hybrid materials. Manuscripts must bring original results of scientific value regarding the materials synthesis, analysis, characterization, study of physical and chemical properties, application, or practically motivated modeling of these aspects. Reports with purely technological impact and/or with a lack of more general value or experimental substantiation will not be accepted.

### MANUSCRIPT FORM

*Abstract* must contain most important and new discoveries, observations or ideas. It is a condensation of the essential results of the paper and not a mere list of the subjects covered in the text. Abstract must clearly relate the topic, methods used, and especially original results and conclusions. Do not repeat information given in the title or refer to the literature in the abstract. Write your abstract in such a manner that it can be directly used by world abstract journals and other information-retrieval systems, where you would not expect to find a poorly written, superficial contribution. Abstract should not exceed 250 words and it is not sectioned into paragraphs.

*Keywords:* Authors should propose 3 to 5 key words suitable for literature databases.

*Figures* should be attached in duplicate at the end of the manuscript, each on a separate sheet. Additionally, electronic versions are required. Preferable formats for graphs are: \*.wmf (windows metafiles), files in Excel, Origin, Grapher and Adobe Illustrator, version 7 or 8.

*Photographs* have to be perfectly sharp and with adequate contrast on white glossy paper. Please also include the electronic version in TIFF format (possibly with LZW compression) scanned at least at 300 DPI. If necessary, compress data as \*.zip or \*.rar archives.

*References* should be marked in the text with the numbers in square brackets, e.g. [1] or McAdams [2]. Please use the following examples to format references.

*Articles:* Greene C.H., Platts D.R.: J.Am.Ceram.Soc. 52, 106 (1969).

*Books:* McAdams W.F.: *Heat Transmission*, 2nd ed., p.196-294, McGraw-Hill, New York 1942.

*Proceedings:* Porod G. in: *Small-angle X-ray Scattering*, p.17-51, Ed. Glatter O., Kratky O., Academic Press, London 1982.

### MANUSCRIPT SUBMISSION

Please send two hardcopies of the manuscript, if possible together with its electronic version, preferentially as e-mail attached files. Suitable are native \*.doc files of MSWord, or \*.rtf. The hardcopy of the final (revised) version of manuscript should be accompanied by its electronic version including figures either attached to e-mail or on a 3.5" DOS-formatted diskette. In addition, the e-mail address of the corresponding author is to be included.

#### Editor:

**Miloslav Bartuška**  
Department of Glass and Ceramics  
Institute of Chemical Technology  
Technická 5, 166 28 Prague  
Czech Republic  
tel.: +420 220 444 002  
fax: +420 220 441 082

#### Executive Editor:

**Jaroslav Kloužek**  
Laboratory of Inorganic Materials  
Institute of Chemical Technology  
Technická 5, 166 28 Prague  
Czech Republic  
tel.: +420 266 009 423  
fax: +420 266 009 421  
E-mail: klouzekj@vscht.cz